

UNDERSTANDING EXTRACTANT AGGREGATION
THROUGH MOLECULAR SIMULATION

by
Michael J. Servis

© Copyright by Michael J. Servis, 2017

All Rights Reserved

A thesis submitted to the Faculty and the Board of Trustees of the Colorado School of Mines in partial fulfillment of the requirements for the degree of Doctor of Philosophy (Nuclear Engineering).

Golden, Colorado

Date _____

Signed: _____

Michael J. Servis

Signed: _____

Dr. Jenifer C. Shafer
Thesis Advisor

Signed: _____

Dr. David T. Wu
Thesis Advisor

Golden, Colorado

Date _____

Signed: _____

Dr. Mark P. Jensen
Professor and Program Chair
Department of Chemistry

ABSTRACT

Solvent extraction is implemented in the nuclear fuel cycle to reprocess used nuclear fuel. One processing challenge in solvent extraction is avoiding third phase formation, which limits metal loading into the organic phase and therefore extraction efficiency. Third phase formation is known to depend strongly on extractant and solvent molecular structure for solvating organophosphorus extractants. Molecular dynamics simulations were employed to study the organic phase association of extractant molecules. Force field optimization and validation were conducted for the extractant molecules for properties relevant to organic phase association, including average molecular dipole, dimerization constant and mixing enthalpy with aliphatic solvents. Network analysis was used to quantify speciation of hydrogen bonded clusters of water and nitric acid extracted by tributyl phosphate into *n*-dodecane. Large cluster formation under high extracted nitric acid and water concentrations near the third phase formation phase boundary was found to be consistent with percolation theory. Simulations with uranyl nitrate/extractant clusters showed orientational dependence on the inter-cluster interactions. Structural differences between extractants resulted in changes to the uranyl-centered cluster interaction energetics. Future research may link these differences in metal-centered cluster interactions to organic phase solubility and third phase formation under high metal loading.

TABLE OF CONTENTS

ABSTRACT	iii
LIST OF FIGURES	viii
LIST OF TABLES	xiv
ACKNOWLEDGMENTS	xvii
DEDICATION	xviii
CHAPTER 1 BACKGROUND AND MOTIVATION	1
1.1 Solvent Extraction and the Nuclear Fuel Cycle	1
1.2 Third Phase Formation	3
1.3 Scattering Interpretations of Third Phase Formation	5
1.4 Molecular Structure and Third Phase Formation	7
1.5 Molecular Dynamics	9
1.6 Solvent Extraction and TBP in Molecular Dynamics	10
1.7 Evaluation of TBP Potentials	11
1.8 MD Simulation with Metal Ions	12
1.9 Thesis Outline	13
CHAPTER 2 A MOLECULAR DYNAMICS STUDY OF TRIBUTYL PHOSPHATE AND DIAMYL AMYL PHOSPHONATE SELF-AGGREGATION IN DODECANE AND OCTANE	16
2.1 Abstract	16
2.2 Introduction	17
2.3 Methodology	19

2.3.1	TBP model details	19
2.3.2	Simulation systems and conditions	23
2.3.3	Analysis methods and definitions	27
2.4	Results	28
2.4.1	Neat TBP and DAAP simulations	28
2.4.2	Extractant/Diluent Organic Phase Simulations	32
2.5	Conclusions	43
2.6	Acknowledgements	44
CHAPTER 3 THE ROLE OF SOLVENTS IN ORGANIZATION AND ASSOCIATION OF NEUTRAL ORGANOPHOSPHORUS EXTRACTANTS		46
3.1	Abstract	46
3.2	Introduction	46
3.3	Methodology	49
3.3.1	Force Fields	49
3.3.2	Simulation Systems and Conditions	53
3.4	Results	54
3.4.1	Volume Change on Mixing	54
3.4.2	Enthalpy of Mixing	57
3.4.3	Extractant Self-Association	58
3.5	Discussion	64
3.5.1	Isopropanol	64
3.5.2	Alkyl Wetting	66
3.5.3	Solvent Dilution of Extractant Dipole Interactions	68

3.5.4	Diethyl Ether and Extractant-Solvent Polar Interaction	69
3.5.5	Comparing <i>n</i> -Hexane, Diethyl Ether and Toluene	71
3.6	Conclusions	74
CHAPTER 4 NETWORK ANALYSIS AND PERCOLATION TRANSITION IN HYDROGEN BONDED CLUSTERS: NITRIC ACID AND WATER EXTRACTED BY TRIBUTYL PHOSPHATE		
4.1	Abstract	76
4.2	Introduction	77
4.3	Methodology	81
4.3.1	Force Fields	81
4.3.2	Simulation Systems and Conditions	83
4.3.3	Hydrogen Bonding Definitions	85
4.3.4	Network Analysis	85
4.3.5	QM Calculations of 1:2 TBP:HNO ₃	89
4.3.6	IR Spectroscopy	89
4.3.7	Monte Carlo Lattice Calculations	90
4.4	Results	90
4.4.1	Overview	90
4.4.2	Overall Hydrogen Bonding Behavior	91
4.4.3	Equilibrium Binding Model	93
4.4.4	TBP, HNO ₃ and H ₂ O Structures and Substructures	94
4.4.5	QM Vibrational and IR Spectroscopic Determination of 1:2 TBP:HNO ₃ Topology	97
4.4.6	Large Cluster Analysis	100

4.4.7	Percolation and Lattice Monte Carlo Comparison	104
4.5	Conclusions	105
4.6	Acknowledgements	108
CHAPTER 5 THE ROLE OF EXTRACTANT STRUCTURE IN THE ASSOCIATION OF EXTRACTED URANYL NITRATE CLUSTERS		109
5.1	Introduction	109
5.2	Methodology	112
5.2.1	Quantum Mechanical Calculations	112
5.2.2	Force Fields	112
5.2.3	Simulations Details and Compositions	113
5.3	Results	114
5.3.1	Organic Phase Uranyl Parameterization	114
5.3.2	Orientation and Spatial Dependence of Uranyl Cluster Association . .	118
5.4	Conclusions	121
CHAPTER 6 CONCLUSIONS AND FUTURE DIRECTIONS		129
6.1	Summary and Conclusions	129
6.2	Third Phase Formation with Water and Inorganic Acids	130
6.3	Third Phase Formation in Metal Ion Extraction	133
REFERENCES CITED		137
APPENDIX SUPPORTING INFORMATION FROM CHAPTER 4		150

LIST OF FIGURES

Figure 1.1	Molecular structures of the amphiphilic extractant molecules tributyl phosphate (TBP), triamyl phosphate (TAP), dibutyl butyl phosphonate (DBBP) and diamyl amyl phosphonate (DAAP).	3
Figure 1.2	An organic phase TBP/uranyl/nitrate cluster. The nitrate anions and TBP extractants coordinate the uranyl ion in a plane perpendicular to the uranyl oxygens oriented into and out of the page. The nitrate anions are bidentate, resulting in sixfold total coordination. Any hydrogen bonded water or nitric acid molecules in the cluster are not shown.	4
Figure 1.3	The limiting organic concentration (LOC) for thorium over a range of aqueous phase nitric acid concentrations for TBP, TAP, DBBP and DAAP.	8
Figure 2.1	AMBER atom type designations for TBP (left) and DAAP (right).	20
Figure 2.2	a) Snapshot of 0.12 M GAFF/p TBP in <i>n</i> -dodecane, with the two dimers in the simulation, circled in frame a, shown enlarged in b and c. d-f) A linear trimer, a cyclic trimer and a tetramer from the 0.97 M TBP simulation. Diluent is omitted for clarity. Oxygen atoms are depicted in red, phosphorus in green, and carbon tails in blue and white for carbon and hydrogens, respectively.	32
Figure 2.3	Angle versus distance frequency plot for GAFF/p 0.97 M TBP, 0.97 M DAAP and 0.04 M TBP in <i>n</i> -dodecane, shown in a, b and c respectively. The orientation convention is also illustrated. The color bar indicates the normalized count density in units of $\text{\AA}^{-1} \text{deg}^{-1}$	35
Figure 2.4	The dimer concentration versus total organic phase extractant concentration is plotted for each TBP and DAAP model and the extrapolated experimental value. Results for <i>n</i> -dodecane are given in a and <i>n</i> -octane in b. The dimerization constant for TBP and DAAP in both diluents at each simulated concentration is given in c.	39
Figure 2.5	The speciation, in number per extractant molecule, of 2^{nd} to 5^{th} order TBP and DAAP aggregates are plotted for each extractant and diluent combination for a) TBP in <i>n</i> -dodecane, b) TBP in <i>n</i> -octane, c) DAAP in <i>n</i> -dodecane and d) DAAP in <i>n</i> -octane.	41

Figure 2.6	a) Average number of extractant aggregates per extractant molecule, for varying aggregate size. b) The average coordination number for each aggregate size. TBP and DAAP at 0.97 M in both <i>n</i> -dodecane and <i>n</i> -octane are plotted together in each panel.	43
Figure 3.1	The molecular structure of: tributyl phosphate (TBP), triamyl phosphate (TAP), dibutyl butyl phosphonate (DBBP) and diamyl amyl phosphonate (DAAP).	48
Figure 3.2	Atomic charges for the extractant molecules are given in fundamental charge units. Charges are only given once for symmetric atoms.	51
Figure 3.3	Atomic charges for the solvent molecules are given in fundamental charge units. Charges are only given once for symmetric atoms.	52
Figure 3.4	The percent volume change on mixing for the TBP/dodecane mixture is shown for the TBP model used here, along with the two AMBER models and experimental values.	56
Figure 3.5	The percent volume change on mixing for each binary system is plotted across the range of extractant volume fractions for each extractant.	57
Figure 3.6	The enthalpy of mixing for the TBP/dodecane (left panel) and TBP/hexane (right panel) binary mixtures are plotted versus extractant volume fraction. Experimental data is plotted in red diamonds, the modified GAFF TBP developed here with optimized GAFF <i>n</i> -dodecane is plotted with black squares. The OPLS and refined OPLS simulation data are plotted with dark and light green triangles, respectively, for the <i>n</i> -dodecane systems only.	59
Figure 3.7	The enthalpy of mixing for each binary system is plotted versus volume fraction for each extractant.	60
Figure 3.8	The distribution of aggregate sizes for the 30% extractant systems are plotted on a semilog scale for each solvent and extractant combination.	62
Figure 3.9	Volume change on mixing and enthalpy of mixing data for the four extractants in isopropanol are replotted here for comparison between those solvent and extractant types.	64
Figure 3.10	The radial distribution for the isopropanol alcohol hydrogen and the extractant phosphoryl oxygen, which form the extractant-solvent hydrogen bond, is plotted for the four extractants for the 50% and 70% extractant volume fraction systems.	66

Figure 3.11	Percent volume change on mixing and enthalpy of mixing for the four extractants in <i>n</i> -dodecane and <i>n</i> -hexane are replotted here for comparison between solvent and extractant types.	67
Figure 3.12	Volume change on mixing and enthalpy of mixing data for the four extractants in diethyl ether are replotted here for comparison between solvent and extractant types.	69
Figure 3.13	The radial distribution for the ether oxygen in diethyl ether and the extractant phosphoryl oxygen is plotted for the four extractants for the 50% extractant volume fraction systems.	71
Figure 3.14	Percent volume change on mixing and enthalpy of mixing data for the four extractants in toluene are replotted here for comparison between solvent and extractant types.	72
Figure 3.15	The aromatic and aliphatic carbon-carbon radial distribution functions for the pure TBP, toluene and benzene systems as well as the 50% TBP with toluene and benzene systems are plotted.	73
Figure 4.1	The AM1-BCC atomic charges used in the GAFF nitric acid model. Charges are given in fundamental units.	83
Figure 4.2	The six possible hydrogen bond types in the TBP-HNO ₃ -H ₂ O extraction systems are depicted here with participating atoms highlighted for the given hydrogen bond type. The subscript in the atom name gives the molecule type to which the O or H atom belongs with <i>T</i> being TBP, <i>N</i> nitric acid and <i>W</i> water.	86
Figure 4.3	A graph with seven vertices and five edges resulting in three clusters.	87
Figure 4.4	The average number of each type of hydrogen bond across all systems, normalized by the total number of oxygen atoms of that hydrogen bond type, is plotted as data points. The top panels give hydrogen bonds with the oxygen bond acceptor belong to TBP, the middle panel for nitric acid and the lower panel for water. Calculated numbers of each hydrogen bond type from the equilibrium binding model are plotted as dashed lines.	92

Figure 4.5	Snapshots of several hydrogen-bonded structures. Part I shows a 1:1 TBP-HNO ₃ structure, part II a TBP-HNO ₃ -HNO ₃ Chain structure and part III a (TBP) ₂ (HNO ₃) ₃ (H ₂ O) cluster. The oxygen atoms in the nitric acid are shown in red, the nitrogen in blue and the hydrogen in white. For water, the hydrogen atoms are white and the oxygen atoms pink. The TBP atoms are depicted as solid bonds with the green phosphoryl oxygen atom expanded for visualization.	95
Figure 4.6	The average number observed in simulation, per TBP molecule, of the TBP-HNO ₃ , TBP-H ₂ O, TBP-HNO ₃ -HNO ₃ Chain and TBP-(HNO ₃) ₂ Shared structures is plotted for each system. Systems with one water concentration are in black while the red, green and blue data points correspond to the systems with three water concentrations.	96
Figure 4.7	The average number observed in simulation, per TBP molecule, of the TBP-HNO ₃ -HNO ₃ Chain, TBP-HNO ₃ -H ₂ O, TBP-H ₂ O-TBP and TBP-H ₂ O-H ₂ O substructures is plotted for each system. Systems with one water concentration are in black while the red, green and blue data points correspond to the systems with three water concentrations.	98
Figure 4.8	The vibrational modes for the coupled hydrogen wag and O-N-O asymmetric stretch of the nitric acid determined for the Shared and Chain configurations with QM calculations are plotted with the experimentally observed spectrum. Of the two configurations, the calculated frequencies of the vibrations for the two nitric acid molecules in the Chain structure match the peak separation observed experimentally.	100
Figure 4.9	A snapshot from the 1.25 M [HNO ₃] _{org} , 0.31 M [H ₂ O] _{org} C system. TBP is represented with the phosphoryl oxygen atom colored green and enlarged. Nitric acid and water molecules are represented with oxygen atoms shown in red for nitric acid and pink for water. Nitrogen atoms are blue and hydrogen atoms in both molecules are white. Dodecane is omitted for clarity. Two examples of isolated clusters are highlighted.	101
Figure 4.10	The semilog histograms of the average number observed versus cluster size are plotted for the 1.10 and 1.25 M [HNO ₃] _{org} A (0.15 M [H ₂ O] _{org}), B (0.23 M [H ₂ O] _{org}) and C (0.31 M [H ₂ O] _{org}) systems.	102
Figure 4.11	The average number of hydrogen bonds per molecule for water and nitric acid are given for the A-C systems for 1.25 M [HNO ₃] _{org} . While the numbers for nitric acid are generally unchanged with increasing water, the probabilities for water shift towards larger values as water is added to the system.	104

Figure 4.12	The cluster size distribution for the 1.25 M $[\text{HNO}_3]_{org}$ systems, with additional higher water concentration simulations, is compared to the cluster size distribution plots for a 15 by 15 square lattice for a range of bond probabilities. The similarity in distribution statistics implies that the simulation data is showing a percolation phase transition with finite size effects creating spanning clusters between 100 and 120 polar solutes in size.	106
Figure 4.13	Pictured is a snapshot of a large cluster, of size 117, from the 1.25 M $[\text{HNO}_3]_{org}$ C system. TBP molecules are depicted as green for clarity.	107
Figure 5.1	Molecular structures of the amphiphilic extractant molecules tributyl phosphate (TBP), dibutyl butyl phosphonate (DBBP) and triamyl phosphate (TAP).	111
Figure 5.2	An organic phase TBP/uranyl/nitrate cluster. The nitrate anions and TBP extractants coordinate the uranyl ion in a plane perpendicular to the uranyl ion oriented into and out of the page. The nitrate anions are bidentate, resulting in sixfold total coordination.	115
Figure 5.3	The dissociation energy profile, zeroed at 5 Å, for the TMP-uranyl nitrate complex is plotted for the QM (black) and fitted MD (red) data.	117
Figure 5.4	Uranyl nitrate cluster structures illustrating parameterization challenges. A) shows the 5-fold coordinate uranyl with monodentate nitrates and three binding TBPs and B) shows the 5-fold coordinate uranyl with nitrates forming a “bridge” between metal centers. C) shows the nitrate out-of-plane bending. D) shows the experimentally determined bidentate coordination.	123
Figure 5.5	Uranium-uranium RDFs for the 6 (0.03 M) $\text{UO}_2\text{-(NO}_3)_2\text{-(Extractant)}_2$ in <i>n</i> -dodecane simulations for TBP and TAP.	124
Figure 5.6	Uranium-uranium RDFs for TBP are plotted in panel A, TAP in panel B and DBBP in panel C.	125
Figure 5.7	The schematic shows the angle between uranyls measured for the angle distributions. All four possible $O = U - U$ angles are counted separately for each uranyl pair within the distance cutoff, resulting in a roughly symmetric distribution around 90 degrees.	126

Figure 5.8	A distribution of the uranyl-uranyl orientations as a function of uranium-uranium distance. The left panels correspond to 20 uranium systems and the right panels 40 uranium systems. The top panels are for TBP systems, the middle panels for TAP and the bottom panels for DBBP.	127
Figure 5.9	Snapshots of associating $\text{UO}_2\text{-(NO}_3)_2\text{-(TBP)}_2$ clusters, with snapshot A showing corresponding to the peak at 5-6Å, and snapshot B to the region at 10-12Å.	128
Figure 6.1	The cluster size distributions calculated from MD simulation of nitric acid and water extracted by TBP near the percolation threshold, compared with MC calculated lattice bond percolation cluster size distributions from 2 and 3 dimensional square and cubic lattices over a range of bond formation probabilities p_B around the percolation threshold probability. The theoretical percolation threshold cluster size distribution for 2D and 3D square lattices are overlaid with a red line. The MD data is compared to the 3D theoretical lattice percolation threshold distribution.	136
Figure A.1	The RDFs used to determine the distance cut-off given in the text for the hydrogen bond definitions of each hydrogen bond type.	152
Figure A.2	The average observed number of the TBP, TBP-HNO ₃ -H ₂ O, HNO ₃ , TBP-H ₂ O-HNO ₃ , H ₂ O and TBP(HNO ₃)(H ₂ O) structures.	154
Figure A.3	The average observed number of the TBP-H ₂ O-HNO ₃ , TBP(H ₂ O) ₂ , TBP(H ₂ O)(HNO ₃) and TBP(HNO ₃) ₂ substructures.	155

LIST OF TABLES

Table 2.1	GAFF equilibrium bond length and bond energy parameters.	21
Table 2.2	GAFF equilibrium angle and angle energy parameters.	21
Table 2.3	GAFF equilibrium dihedral angle and dihedral energy parameters. Asterisk indicates modified parameters.	22
Table 2.4	BCC values for the bonded atom combinations that exist in TBP and DAAP.	23
Table 2.5	TBP and DAAP AM1-BCC charge sets. For DAAP, charges for the two carbon tails with a bridging oxygen are listed together first with the third tail without an oxygen listed after.	24
Table 2.6	Extractant concentrations for organic phase simulations. Neat TBP, DAAP and mixed composition details.	26
Table 2.7	Simulation density and dipole for neat TBP and DAAP liquids. Default GAFF, GAFF/p, GAFF/vdw, AMBER99 and scaled AMBER99 literature TBP models are compared with experimental values. Percent error with respect to the corresponding value is given for each simulation result. The asterisk denotes literature models with atomic charge scaling factors.	31
Table 2.8	Dimerization constants calculated from simulation for GAFF/p and scaled AMBER99 TBP models are given with the experimental and GAFF/vdw values. Computed GAFF/p DAAP dimerization constants are also given. Percent error is given relative to the corresponding experimental value, if applicable.	38
Table 3.1	Physicochemical properties for the four extractants, with available experimental data used in the optimization fitting, are given for the pure extractant systems with optimized force field potentials.	53
Table 3.2	Physicochemical properties of the simulated pure solvent systems are given with available experimental data.	54
Table 3.3	The number of molecules of each type for simulations of a given extractant volume fraction.	55

Table 3.4	The association free energies for extractant dimer formation and higher order associations are given below for each extractant and diluent combination for the 30% extracting volume simulations.	63
Table 4.1	Numbers of molecules and their approximate concentrations for each simulation in this study. The systems correspond to a range of $[\text{HNO}_3]_{aq,i}$, with A-C in the 1.10 and 1.25 M systems indicating simulations run with a range of water concentrations.	84
Table 4.2	The distance cutoffs applied for the different hydrogen bond types in all simulations are given here. An angle cutoff of 30 degrees was also used for each hydrogen bond type.	85
Table 4.3	The binding constants, defined in Equation 4.3, for the six hydrogen bonds obtained through least squares fitting of the simulation data.	94
Table 5.1	The uranyl and nitrate charges are given. The pairwise nonbonded uranium-phosphoryl oxygen parameters developed in this study are also given.	112
Table 5.2	The uranium concentrations and MD box compositions for the simulations with TBP.	113
Table 5.3	The uranium concentrations and MD box compositions for the simulations with DBBP.	113
Table 5.4	The uranium concentrations and MD box compositions for the simulations with TAP.	114
Table 5.5	The experimental, QM calculated and fitting MD simulation binding distances for the $\text{UO}_2\text{-(NO}_3)_2\text{-(TBP)}_2$ cluster (with nitrate distance restraints to enforce the $\text{U-O}_{\text{nitrate}}$ and $\text{U-N}_{\text{nitrate}}$ distances). The simulation and experimental distances are for an <i>n</i> -dodecane solvent liquid phase, while the QM calculations in the gas phase.	118
Table A.1	GAFF Lennard Jones parameters for the TBP and dodecane atom types.	150
Table A.2	GAFF equilibrium bond length and bond energy parameters.	150
Table A.3	GAFF equilibrium angle and angle energy parameters.	151
Table A.4	GAFF equilibrium dihedral angle and dihedral energy parameters. Asterisk indicates modified parameters.	152

Table A.5	TBP and dodecane AM1-BCC charges. For dodecane, the carbon and hydrogen atoms are denoted by position in the chain.	153
-----------	---	-----

ACKNOWLEDGMENTS

I thank my advisors, Dr. Jenifer Shafer and Dr. David Wu, for their invaluable input and support during my time as their student. Dr. Mark Jensen and Dr. Aurora Clark have provided valuable feedback on experimental and quantum mechanical aspects of my research, respectively.

For my parents.

CHAPTER 1

BACKGROUND AND MOTIVATION

1.1 Solvent Extraction and the Nuclear Fuel Cycle

Nuclear energy technology has been identified as an important source of commercial energy. At present, developing nations are interested in nuclear energy as a reliable and dense source of energy for growing populations. Developed regions are interested in a power source to supplement renewable energy that does not significantly contribute to anthropogenic climate change. Nuclear energy fits both of these criteria. However, the failure to utilize Yucca Mountain has raised the concern of where to deposit used nuclear fuel[1].

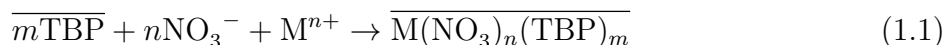
One technology that could reduce the burden for nuclear waste storage is used fuel reprocessing. Reprocessing consists of extracting the fissile isotopes from dissolved fuel rods to reconstitute into new fuel. The remaining isotopes can be separated such that the particularly dangerous or long lived isotopes are removed from the bulk of the waste, greatly reducing the volume of problematic material. Reprocessing technology was initially developed as a part of the Manhattan Project, but has not been implemented on a commercial scale in the United States for almost forty years for fear it could lead to nuclear proliferation. However, France and other countries have successfully implemented reprocessing schemes in their nuclear fuel life cycles. As no current plan exists for long term nuclear fuel storage, reprocessing in the United States remains worth consideration.

Light water nuclear fuel used in the United States' commercial reactor fleet consists of enriched uranium embedded in an oxide matrix. After its lifetime of use in a reactor, the fuel still contains the vast majority of U-238 and about 1/3 of the original U-235 atoms as well as fissile activation products like Pu-239. As a result, discarding the fuel after one use results in the loss of large amounts of fissile material and therefore lost energy production. Reprocessing would give access to this additional fuel while also reducing the volume of

waste. Furthermore, additional reprocessing steps can be implemented to further partition the fuel into groups of elements by radioactivity and longevity. This means that the highly radioactive or particularly long lived isotopes can be separated from the bulk of the waste, further reducing the volume of nuclear waste that is difficult to handle or needs to be isolated for time scales longer than can be accounted for by human engineering.

In a closed nuclear fuel cycle, used fuel is reprocessed to extract the remaining fissile isotopes to reconstitute into new fuel. The industry standard method for this separation is the Plutonium Uranium Reduction EXtraction (PUREX) process. PUREX is a solvent extraction technique wherein used nuclear fuel is dissolved in a concentrated nitric acid aqueous solution. That aqueous solution is then contacted with an organic phase containing ~30% tri-*n*-butyl phosphate (TBP) by volume in a long chain carbon diluent such as *n*-dodecane[2]. The TBP molecule, depicted in Figure 1.1, is amphiphilic, such that its carbon tails enable solubility in the *n*-dodecane organic phase while the polar oxygen head on the phosphoryl group, the negative end of the molecule’s electric dipole moment, interacts with the uranium and plutonium cations in the aqueous phase during mixing. TBP has been selected for this application as it extracts uranium and plutonium over other fission product elements with different oxidation chemistry. Other solvating organophosphorus extractants have been studied for PUREX-type extraction schemes, including triamyl phosphate (TAP), dibutyl butyl phosphonate (DBBP) and diamyl amyl phosphonate (DAAP). The molecular structures of these extractants are shown in Figure 1.1.

After contacting the two phases, TBP then extracts a metal cation as shown in the generic form



where the bar indicates an organic phase species where the nitrate anions serve to charge neutralize the extracted complex. A depiction of this cluster is given in Figure 1.2. “Cluster” is used here to refer to a group of extracted polar solutes in the organic phase connected through coordination (to a metal ion) or hydrogen bonding. With the uranyl nitrate/TBP

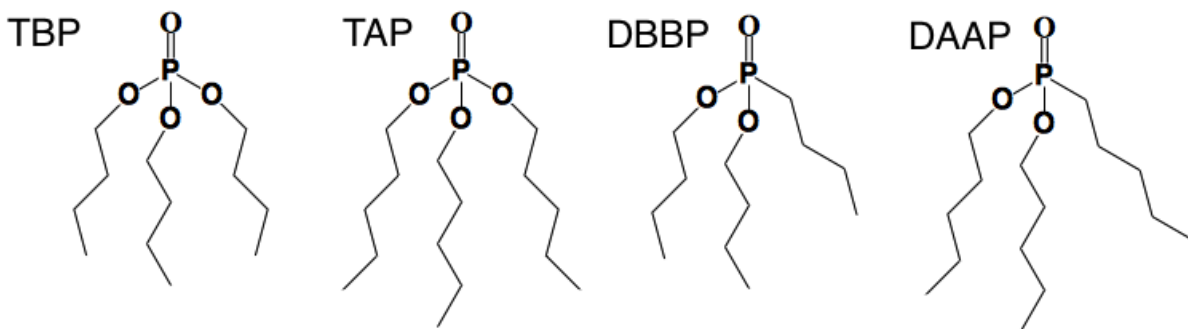


Figure 1.1: Molecular structures of the amphiphilic extractant molecules tributyl phosphate (TBP), triamyl phosphate (TAP), dibutyl butyl phosphonate (DBBP) and diamyl amyl phosphonate (DAAP).

cluster, the alkyl tails of the extractant molecules are oriented outward into the aliphatic solvent while the phosphoryl oxygen and nitrate anions coordinate the metal center. In addition to the metal ion, a number of nitrate anions are extracted that charge neutralize the organic phase complex. Furthermore, not shown in the extraction equation, a number of water molecules coordinated to the metal ion can be extracted. The components of the extracted complex may change upon transport into the organic phase according to the extraction conditions. While successfully implemented in large scale facilities and thoroughly studied empirically, there is still a lack of understanding of the basic chemistry involved in solvent extraction, including third phase formation.

1.2 Third Phase Formation

Third phase formation is an undesirable phenomenon that occurs in solvent extraction systems like PUREX when organic phase metal ion concentrations exceed a maximum threshold, called the “limiting organic concentration” (LOC)[3–6]. In third phase formation, the post-contact organic phase partitions into two separate phases: a light phase, containing mostly diluent, and a heavy phase, containing most of the extractant and extracted solutes. Third phase formation is problematic for two primary reasons. First, the heavy organic phase concentrates the extracted fissile atoms in an uncontrolled manner which could lead

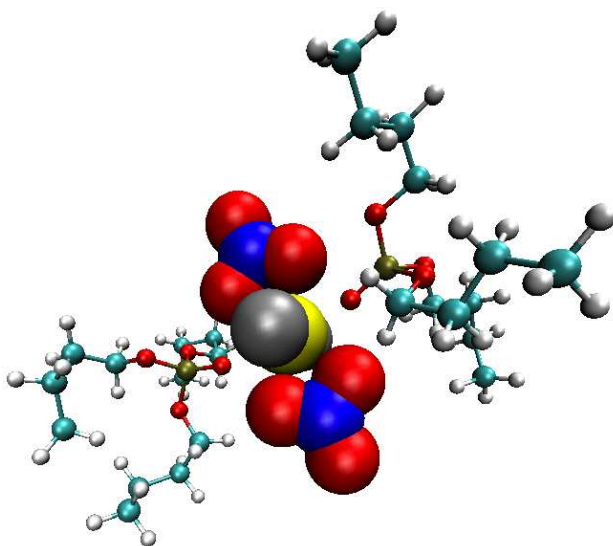


Figure 1.2: An organic phase TBP/uranyl/nitrate cluster. The nitrate anions and TBP extractants coordinate the uranyl ion in a plane perpendicular to the uranyl oxygens oriented into and out of the page. The nitrate anions are bidentate, resulting in sixfold total coordination. Any hydrogen bonded water or nitric acid molecules in the cluster are not shown.

to a criticality. The second issue is that by no longer having homogeneously solubilized metal ions in the organic phase, syphoning off the organic phase to back extract the metal ions is now a more difficult task. By having to avoid third third phase conditions, the efficiency of each extraction step is limited as the total concentration of extracted metal ions cannot exceed the LOC, a value specific to a given extraction system. Understanding the nature of the phase transition would allow for design of extraction systems that improve extraction efficiency.

Several experimental techniques have been employed to investigate the speciation and metal coordination of extracted clusters approaching and after third phase formation for uranium extraction systems. UV-Vis spectroscopy has been used to measure the coordination of nitrate and TBP oxygen atoms to the uranyl metal center, and concluded that the coordination remains unchanged until third phase formation[7–10]. In the heavy phase, nitrate oxygen coordination decreased, implying either a transition from 6-fold to 5-fold coordination of the uranyl group or increased coordination by other polar solutes. IR spec-

troscopy corroborated these conclusions from the UV-Vis data, indicating generally bidentate nitrate coordination to the uranyl[11]. Beyond UV-Vis and IR spectroscopy, the inter-cluster association leading to third phase formation has been probed far more extensively with x-ray and neutron scattering. This will be discussed in detail in the following section.

1.3 Scattering Interpretations of Third Phase Formation

While the third phase is a macroscopically visible phase, the constituent metal-centered clusters are on the nanometer length scale. To investigate the nanoscale molecular associations in the organic phase, neutron and x-ray scattering techniques have been used in the literature for both PUREX-type nuclear fuel cycle separations and rare earth separations[7, 10, 12–25]. While the metal-centered clusters are well characterized for dilute metal concentrations, the change in cluster compositions and inter-cluster interactions are suspected to govern the organic phase separation. Given the large neutron scattering cross sections of hydrogen present in the TBP butyl tails, by deuterating the *n*-dodecane solvent, the neutron scattering primarily results from the TBP molecules. Scattering therefore has been used to investigate the structure and association of these complexes under high metal loading.

Chiarizia and coworkers studied third phase formation with neutron scattering experiments using ellipsoidal and spherical form factors for the metal-centered clusters. Using an ellipsoidal form factor, they found extracted metal ions form reverse micelles with up to 40 TBP molecules at the LOC for zirconium extraction[19]. They concluded that these TBP numbers were unreasonably large compared to the spectroscopically identified discrete uranium-centered clusters. The TBP numbers for the ellipsoidal models for uranium extraction were found to be smaller at around 5 TBPs[10, 15, 17]. While these cluster TBP numbers were more in line with their expectations, the TBP numbers were, surprisingly, significantly smaller for the heavy organic phase than either the LOC samples or the light organic phase.

As the ellipsoidal form factor fitting did not capture the expected aggregation behavior, Chiarizia and coworkers also used the Baxter sticky hard sphere[18]. With the Baxter model,

the clusters are treated as hard spheres with an attractive surface potential. An attractive feature of the Baxter model beyond analytic simplicity is the implied mechanism for phase separation. As the organic phase becomes saturated with spherical “reverse micelle” metal-centered clusters, the surface adhesion leads to increased clustering. At sufficiently high surface attraction and solute volume fraction, the clustering may lead to long-range ordering and phase partitioning.

Using the Baxter model approach, a variety of systems and conditions have been explored, including extractants[20, 26], temperatures[21], metal ions[18, 19, 27] and acid types[21]. The TBP cluster numbers for zirconium[19], thorium[18] and uranium[27] extraction by TBP were found to be between 2 and 3. However, the Baxter model gives decreasing cluster sizes with increasing metal loading into the organic phase. Therefore, one might expect that with more metal ions resulting in larger contributions from the metal-containing clusters, the scattering particles would, on average, increase in size.

The Baxter model has been applied to acid and water extraction by TBP despite the lack of metal ions enforcing the metal-centered geometry of the extracted clusters[21]. While polyprotic acids that coextract significant quantities of water might form reverse micelles in solution that could be roughly spherical, nitric acid coextracts significantly less water but still forms a third phase. Ferraro *et al.* showed that approaching the nitric acid LOC, the most prominent species is a 2:1 nitric acid:TBP complex[28]. Therefore, describing third phase formation with a Baxter potential for this and possibly other TBP/acid/water systems may be insufficient to describe the geometry and interaction of extracted clusters.

There are numerous challenges to fitting the solvent extraction data with simple particle scattering models. Modeling the extracted clusters with the Baxter potential requires the assumption of a monodisperse cluster size distribution. While scattering data have been fit with an attempt to account for polydisperse cluster sizes[29], that approach requires an assumed particle distribution and is therefore is not computed from the scattering data itself. Incorporating polydispersity improved fitting of the Baxter particle model to the

experimental data in the high q range, but required a predetermined particle size distribution. Nave *et al.*[23] modeled extracted clusters using an alternative hard sphere model to the Baxter potential wherein an attractive square well potential of finite width was applied to the hard sphere surface. While fitting parameters can be added to the particle scattering models, a priori choices about the nature of the scattering particles and interparticle potentials remain necessary for scattering analysis which could pose a challenge for solutions where TBP clusters do not form some combination simple to model shapes.

1.4 Molecular Structure and Third Phase Formation

Third phase formation is impacted by every component of a solvent extraction system, including metal and acid types and concentrations, extractant structure and diluent structure. Tetravalent actinides such as Pu(IV) and Th(IV) are more prone to third phase formation than the hexavalent U(VI) dioxocation[4]. By contrast, TBP generally does not extract sufficient quantities of trivalent metals to form a third phase. With a metal-containing aqueous phase, increasing the acid concentration promotes third phase formation, i.e., lowers the LOC[4]. Without metal ions, extraction of acid and water from the aqueous phase still can result in third phase formation[21, 23]. Chirizia *et al.* found significant differences in the acid LOC for sulfuric, perchloric, hydrochloric, phosphoric and nitric acids.

Extractant and diluent molecular structures for similar molecules (e.g. between organophosphorus solvating extractants or between alkane diluents) have also been shown to significantly impact third phase formation[4, 30]. Rao *et al.*[31] showed that differences between TBP and DAAP result in a factor of three difference in thorium LOC. The thorium LOC values for TBP, TAP, DBBP and DAAP reported by Rao *et al.* are plotted in Figure 1.3. Both alkyl tail length and phosphate versus phosphonate head groups have significant impacts on third phase formation, with increasing the alkyl tails and removing a bridging oxygen on the phosphate group (i.e., going from phosphate to phosphonate) increasing the LOC. Rao *et al.* have also shown that decreasing alkane diluent chain length increases the LOC for TBP with a roughly 1.8 times higher LOC for n -hexane than n -dodecane. Alkane branching

decreases the effective length of the solvent, resulting in an increase in the LOC. This could be generalized that increasing similarity between extractant and solvent molecules improves extracted cluster solubility and therefore the LOC. Other diluents that are either partially polar or polarizable also increase the LOC, as well as increasing temperature.

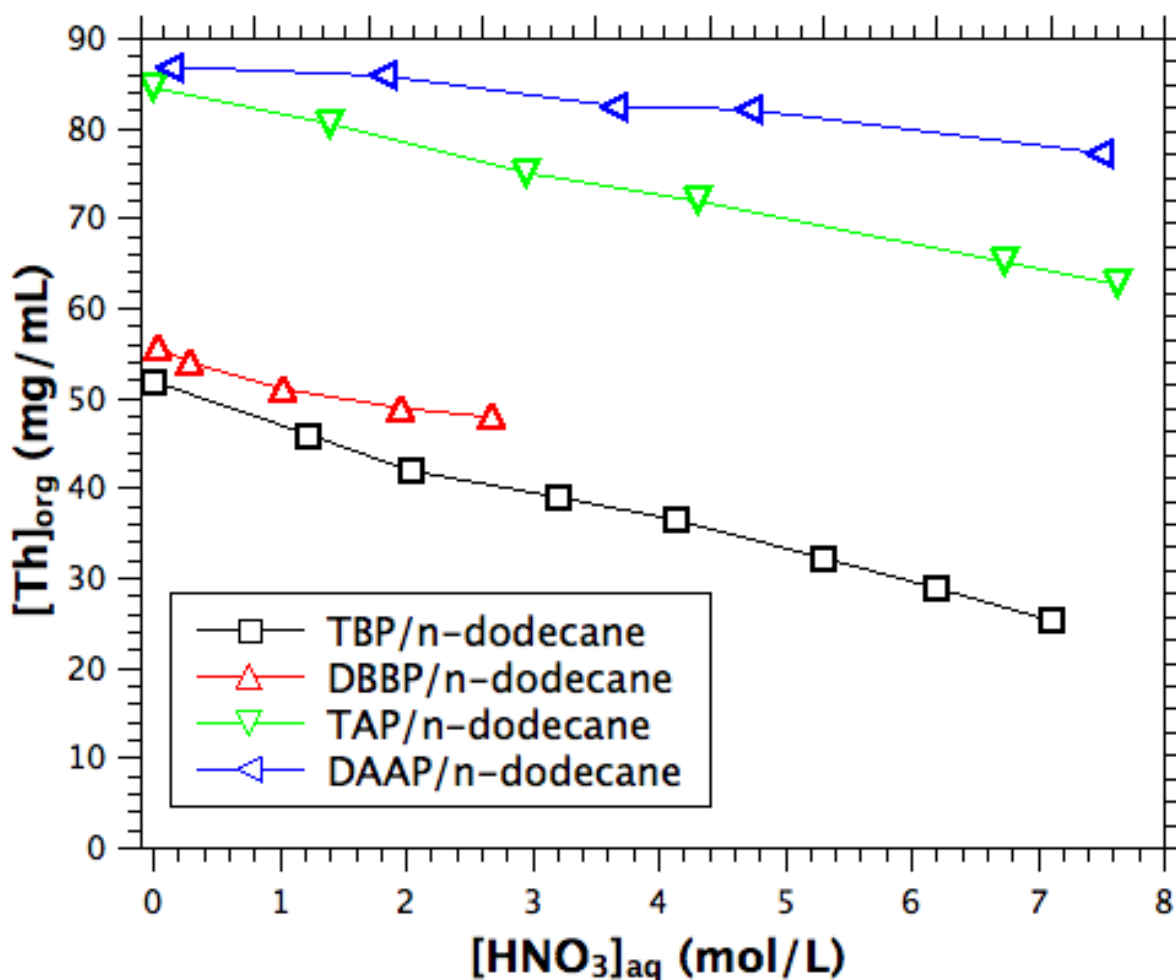


Figure 1.3: The limiting organic concentration (LOC) for thorium over a range of aqueous phase nitric acid concentrations for TBP, TAP, DBBP and DAAP.[31]

While third phase formation results from aggregation of metal-centered clusters, either with or without significant changes to the composition and number of metal ions in the polar core of those clusters, then the differences in LOC resulting from extractant and diluent molecular structure have a significant impact on the aggregation chemistry of the clusters.

Understanding how each of the changes to molecular structure impact aggregation and therefore third phase formation would allow for choice or design of extractants and diluents that avoid third phase formation and therefore improve solvent extraction efficiency. Scattering interpretation with the Baxter model limits the ability to account for the subtle structural changes in more detail than attributing them to either the hard sphere radius or “stickiness” parameter. To achieve the molecular scale resolution required to fully capture the aggregation chemistry of solvent extraction systems, molecular dynamics (MD) simulation can be used to model the post-contact organic phase clusters.

1.5 Molecular Dynamics

In molecular dynamics, atoms are treated as point particles interacting through a classical potential. The total potential energy of the system is defined as the sum of the applicable intermolecular and intramolecular interactions for a given configuration of atoms. For the non-polarizable force fields used predominantly for TBP in the literature and implemented in this thesis, the potential energy has the form of the Assisted Model Building with Energy Refinement (AMBER) force field[32], given in Equation 1.2. Atoms within a molecule interact with harmonic potentials for bonds and angles and a sum of cosine terms for dihedrals angles. Non-bonded interatomic interactions are computed as the sum of a Coulombic interaction and a Lennard-Jones potential to approximate van der Waals forces, given in the last term of Equation 1.2. In MD, periodic boundary conditions are commonly used to approximate a macroscopic phase. Those atoms are given initial coordinates and velocities and the system is propagated forward in time with an integrator solving Newton’s equation of motion to determine the forces on each particle given by the force field’s potential energy equation. Once the forces are determined for a given time step, the position and velocities of the particle are updated for the next time step[33].

$$\begin{aligned}
V = & \sum_{bonds} k_l(l - l_0)^2 + \sum_{angles} k_\theta(\theta - \theta_0)^2 + \\
& \sum_{dihedrals} \sum_n \frac{1}{2} V_n [1 + \cos(n\phi - \gamma_n)] + \\
& \sum_{j=1}^{N-1} \sum_{i=j+1}^N f_{ij} \left\{ \epsilon_{ij} \left[\left(\frac{r_{0ij}}{r_{ij}} \right)^{12} - 2 \left(\frac{r_{0ij}}{r_{ij}} \right)^6 \right] + \frac{q_i q_j}{4\pi\epsilon_0 r_{ij}} \right\}
\end{aligned} \tag{1.2}$$

1.6 Solvent Extraction and TBP in Molecular Dynamics

Relative to its application in the nuclear fuel cycle, computational chemistry approaches to study solvent extraction are recent. The first simulation studies of TBP-based extraction systems began in 1998 when Wipff and coworkers studied TBP behavior at a biphasic water/chloroform interface. They found TBP tail conformations depend strongly on solvation environment, where the $[g, g, g]$ conformation is more favorable in a vacuum (i.e., the environment employed in quantum mechanical calculations) but the $[t, g, g]$ conformation is more favorable in water and chloroform[34]. Later, they investigated the role of associated versus dissociated (with hydronium counterion) nitric acid models. As nitric acid is a strong acid and would therefore be dissociated in the aqueous phase, but is generally extracted by TBP in the associated form, it is not clear how to model nitric acid at the aqueous organic interface with classical MD potentials that typically do not allow for dynamic protonation. They found that the associated nitric acid exists at the interface with much higher than bulk average concentrations while the dissociated model is less concentrated at the interface. Only the associated nitric acid molecule was found to be extracted by TBP into the organic phase[35].

In another study on the same system, Baaden *et al.* showed that TBP molecules oriented with the polar head pointing towards the aqueous phase at the interface and engaged in hydrogen bonding with water, hydronium and associated nitric acid to form microemulsions near the surface, leading to a disordered interfacial region[35]. Later, they expanded these studies to include uranyl nitrate and found that surfactant (TBP) concentration impacted

the phase behavior, where increasing the TBP concentration and mixing the chloroform and water phases led to, in addition to complexation with the uranyl, formation of “microemulsions”. Using chloroform and supercritical CO₂ as organic phase solvents, Wipff and coworkers also observed TBP speciation with uranyl ions[36, 37] and hydrogen bonding with water and nitric acid[35, 37, 38]. In addition to impacting speciation, the protonated nitric acid model hydrogen bonds to the TBP phosphoryl oxygen and increasing the acid concentration in the interfacial layer of TBP. This results in a larger heterogeneous interfacial mixing region which enhances complexation of TBP with metal nitrate salts. Benay and Wipff computed the potential of mean force (PMF) for transfer of uranyl ions between phases for TBP[39] as well as amide[40] and 18-crown-6 ligands[41]. While numerous aspects of interfacial behavior have been investigated in these and other studies[42–46], TBP model validation in an organic environment, the necessary first step before studying more complex organic phase association and speciation, has received less attention.

1.7 Evaluation of TBP Potentials

Many force fields have been employed to simulate TBP in organic solvents. Molecular dynamics simulations studying TBP in solution have used AMBER[47], Chemistry at HARvard Macromolecular Mechanics (CHARMM)[48] and Optimized Potential for Liquid Simulations (OPLS)[49] force fields. Khomami and coworkers have reevaluated the AMBER TBP model originally implemented by Wipff *et al.*[50]. That original model used the default inter- and intramolecular parameters of the AMBER force field and the semiempirical Modified Neglect of Differential Overlap (MNDO) method for computing atomic charges. They found that the original AMBER TBP model overpredicted bulk density and average molecular dipole, while underpredicting the diffusion constant. Khomami *et al.* attempted to modify that model and validate it with various pure TBP phase physiochemical properties including diffusion, density and average molecular dipole. Their modifications to the AMBER model included testing different charge sets calculated from a more accurate density function theory (DFT) calculation with and without an empirical scaling factor applied to the phosphate group

atoms as well as modifications to the AMBER default 1-4 van der Waals interaction scaling factor[51]. By reducing the atomic charges, using OPLS van der Waals parameters for the butyl tails, and to a lesser degree by reducing the 1-4 van der Waals scaling factor, all three physical properties (density, dipole and diffusion constant) were improved relative to experimental values. They have since used their several different modified AMBER TBP models to address water extraction in a biphasic system[52] and TBP self-interaction in an *n*-dodecane diluent[53].

Leay *et al.* measured TBP diffusion and molecular association using the OPLS force field[54]. However, they observed “filament” formation by TBP in dodecane, a finding they later rejected as unphysical and attributed to exaggerated dipole of the OPLS model[55]. That group later optimized the OPLS parameters to better fit experimental mixing enthalpy and small angle x-ray scattering profiles of TBP/alkane mixtures[56]. Mondal and Balasubramanian[57] similarly studied the orientations of TBP dimers in octane and computed x-ray and neutron scattering profiles of those structures. Most recently, and concurrently with the research in this thesis, Vo *et al.* used the Generalized AMBER Force Field (GAFF)[32] to simulate TBP[58, 59]. They validated[59] their model against TBP dimerization and trimerization constants in *n*-dodecane solvent that they measured experimentally[60].

1.8 MD Simulation with Metal Ions

Actinide metal ion-ligand interactions have been investigated with computational chemistry extensively in the literature[61–73]. Wipff and coworkers implemented hybrid MD/QM methods to investigate uranyl coordination by water, nitrate anions and extracting ligands including TBP[34, 36, 61, 63–65]. They also developed a non-polarizable classical MD potential for the uranyl cation[67, 68] that is still implemented in the literature[74]. Ye *et al.* used that uranyl potential to study nitrate-uranyl association in the aqueous phase. They found that increasing nitrate concentration results in increased coordination to uranyl[74]. The nitrate associates with the aqueous uranyl ion to replace a single water molecule, preserving the five-fold planar coordination. Relative to experiment, simulation somewhat overpredicted

the degree of nitrate association with the uranyl metal center at all nitrate concentrations. The uranyl MD potential developed by Wipff[67] has been reevaluated in light of new experimental data indicating its underestimation of the uranyl-water interaction strength and water coordination residence times[75]. Most recently, a different uranyl polarizable potential has been developed with an emphasis on replicating the lifetimes of water association[76]. However, all of these existing literature models were developed for aqueous environments and are not suitable for organic phase coordination in the nitrate/TBP systems where the coordination number of the uranyl dioxo cation changes from 5 to 6, as depicted in Figure 1.2. In addressing this shortcoming of the uranyl models, studies have forced bidentate coordination of the nitrate anions to the aqueous uranyl model through restraint potentials[36, 39], or sacrificed realistic organic phase coordination to accurately capture aqueous phase and interfacial coordination[77]. There does not exist a uranyl model developed to replicate organic phase coordination.

1.9 Thesis Outline

As discussed in the preceding literature review, all of the non-interfacial (i.e. organic phase only) simulations of TBP have attempted to validate pure-phase TBP behavior or TBP self-association in an alkane solvent. Multiple times in the literature, small microemulsions of water extracted by TBP near the interface have been spuriously referred to as “third phases”[36, 43], rather than using “third phase” to describe the organic phase splitting into macroscopically distinct phases. Third phase formation results in a separate, thermodynamically stable, bulk phase and is therefore not solely an interfacial phenomenon but rather governed by association and solubility of the extracted complexes[78]. To wit, after forming a third phase with TBP, water and nitric acid, one can physically remove a stable third phase from the three phase system. Upon cooling, this heavy organic phase can separate into two phases, but with the application of heat, reform the heavy phase. Therefore, to understand the nature of organic phase complexation and inter-complex association, simulations of organic phase systems are conducted in this thesis.

Chapter 2 investigates the association of TBP and DAAP in *n*-dodecane and *n*-octane solvents. Existing AMBER models that employ charge scaling to better replicate dipole and density are shown to substantially underpredict self-association in alkane solvents. The GAFF force field with modifications to certain dihedral parameters is used instead to model TBP and DAAP to accurately capture the dipole and density while retaining the correct solution phase self-association.

In Chapter 3, this updated potential is applied to TAP and DBBP, in addition to TBP and DAAP, and simulations are conducted with a wide range of organic solvents. The potentials are further fitted to pure phase enthalpy of vaporization and validated for volume change on mixing and enthalpy of mixing for TBP/alkane solutions. Extractant-extractant and extractant-solvent interactions are characterized for alkane and polar organic solvents, including diethyl ether, toluene and isopropanol.

In Chapter 4, hydrogen bonded cluster formation is characterized using network analysis for water and nitric acid extraction by TBP in *n*-dodecane. Equilibrium binding constants are computed to describe the relative hydrogen bond strengths and predict total hydrogen bond populations. Clusters of specific composition and topology are measured and the cluster size distributions are measured for high water and acid loading. The large cluster formation approaching the third phase transition under high acid and water loading is not found to be consistent with reverse micelle formation, as presumed in the literature, but rather is consistent with a percolation transition wherein a system-spanning hydrogen bonded cluster forms.

Organic phase behavior of extracted uranium-centered clusters is investigated in Chapter 5. A potential is developed for a restrained, associated uranyl-nitrate complex which replicates the QM-derived TBP association energies. The uranyl-center complex is used in simulations of post-contact *n*-dodecane organic phases for TBP, TAP and DBBP. The effects of the organic solvation environment is investigated through comparison of a pure *n*-dodecane phase and a PUREX-type solvent with excess TBP and extracted nitric acid and water. The

inter-cluster interactions and their directionality are measured and compared between extractants for a range of uranium concentrations. Variables found to impact this association, and therefore presumed to influence the cluster solubility and third phase tendencies, are identified for investigation in future research.

CHAPTER 2

A MOLECULAR DYNAMICS STUDY OF TRIBUTYL PHOSPHATE AND DIAMYL AMYL PHOSPHONATE SELF-AGGREGATION IN DODECANE AND OCTANE

Modified from a paper published in *The Journal of Physical Chemistry B*¹.

*Michael J. Servis*², *Caleb A. Tormey*³, *David T. Wu*⁴, *Jenifer C. Braley*⁵

2.1 Abstract

A molecular dynamics model for tributyl phosphate (TBP) and diamyl amyl phosphonate (DAAP) is presented using the Generalized AMBER Force Field (GAFF) and the AM1-BCC method for calculated atomic charges with a modification to the phosphorus-containing dihedral parameters. The density and average molecular dipole in a neat liquid simulation, and dimerization in *n*-dodecane and *n*-octane diluents, compare favorably to experimental values. At low extractant concentration, investigation of the dimer structure reveals the offset “head-to-head” orientation as the predominant structure over a range of TBP and DAAP concentrations with a phosphoryl oxygen separation distance between dimerized extractants of 3 to 5.5 Å. At high extractant concentrations, a graph analysis of extractant aggregates was used to determine concentrations of each aggregate size and the average coordination number, which gives a measure of the linearity of the aggregates. For aggregates up to 7 extractant molecules, the mean free energy of association per molecule was found to be 0.55-0.59 kcal/mol and 0.72 kcal/mol for TBP and DAAP, respectively. In both diluents, TBP formed large aggregates more frequently than DAAP and those aggregates were more

¹Adapted with permission from *The Journal of Physical Chemistry B* **2016** 10 (120). 2796-2806. Copyright 2016 American Chemical Society.

²Primary Author and Researcher

³Co-author

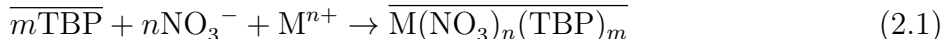
⁴Advisor

⁵Corresponding Author and Advisor

nonlinear than their DAAP equivalents. This finding anticipates differences in aggregation chemistry between TBP and DAAP in PUREX extraction systems.

2.2 Introduction

The Plutonium URanium EXtraction (PUREX) process is implemented in a closed nuclear fuel cycle to recover fissile isotopes of uranium and plutonium from used nuclear fuel. PUREX is a solvent extraction technique wherein the spent nuclear fuel is dissolved in a 3 to 4 molar nitric acid aqueous solution. That solution is contacted with an organic phase containing $\sim 30\%$ tributyl phosphate (TBP) by volume in kerosene[79]. Kerosene has similar physiochemical properties to the *n*-dodecane and *n*-octane evaluated in this manuscript. After contact, TBP selectively recovers hexavalent and tetravalent U and Pu, respectively. The general expression used to describe metal extraction by TBP is presented in Equation 2.1. Here, the overbar indicates an organic phase species. The extracted nitrate anions serve to charge neutralize the complex[80–82].



Solvent extraction is a tunable, many-component system such that an atomic-level understanding of the many molecular interactions would greatly enhance the process design. To that end, PUREX-type systems with TBP have been studied before with molecular dynamics simulation. Previous studies have examined a diverse set of questions related to metal ion recovery by TBP. Simulation studies from Wipff and coworkers have covered topics such as interface behavior and metal ion coordination, as well as alternative diluents such as supercritical CO₂ and chloroform[34–36, 38, 61, 63, 65, 68]. Other researchers have investigated organic phase TBP association and extraction mechanics[46, 54]. Khomami and coworkers have investigated the extraction mechanics of the uranium nitrate complex[51, 77, 83].

Recently, research has focused on vetting the physical integrity of TBP models used in these simulations with experimental data. Khomami *et al.* have investigated modifications to the TBP model in a neat liquid phase[50] and in *n*-dodecane[53]. Those papers were the

first to compare TBP thermophysical properties to experimental values and investigate the use of modifications to refine TBP model accuracy. However, as these modifications were implemented to match certain physical properties largely through the use of an *ad hoc* scaling factor on the atomistic coulombic charges, they have lost fidelity in other aspects, such as organic phase structuring. While these previous efforts provided significant advancements regarding the limitations of previous TBP models, this current study provides a different TBP model that replicates the desired physical properties without the use of a scaling factor that compromises accurate representation of the organic phase structure. Recently, Vo *et al.* proposed a similar TBP model aimed at matching experimental values of those properties[58]. Comparisons between that recent model and the one generated in this study are discussed in this manuscript. For clarity, the model presented here is referred to as GAFF/p. The model given by Vo *et al.* is referred to as GAFF/vdw as the primary deviation from the default GAFF parameters in that model is an adjustment to the O2 van der Waals parameters.

This paper will describe the TBP and diamyl amyl phosphonate (DAAP) models, generated with the same methodology, including bond, angle and dihedral parameters as well as the method for generating atomic charges. The self-aggregation in *n*-dodecane and *n*-octane of DAAP compared to TBP is also of interest as the aggregation of the two extractants in PUREX post-extraction systems deviates significantly with respect to metal ion limiting organic concentration and third phase formation[31]. Characterization of extractant aggregation at PUREX concentrations is experimentally challenging. To access this important chemical behavior, molecular simulation is coupled with graph analysis, performed in part with the ChemNetworks software[84], to study dimerization as well as the extractant self-aggregation that occurs especially at higher concentrations. The results of this manuscript suggest that the proposed extractant model may provide an improved model for the study of TBP and similar extractants in aliphatic diluents most relevant to used nuclear fuel re-processing.

2.3 Methodology

2.3.1 TBP model details

The Assisted Model Building with Energy Refinement (AMBER) family force fields, both all atom and united atom with AMBER94 and AMBER99 parameter sets, have been used in the literature for simulations of TBP. However, those parameters are not necessarily well suited for small organic molecules such as TBP and DAAP. The Generalized AMBER Force Field (GAFF)[32] parameter set is implemented here to generate a TBP model that provides better replication of physical properties relevant to organic phase self-interaction than other AMBER parameter sets. The AMBER potential function is shown in Equation 2.2.

$$\begin{aligned} V = & \sum_{bonds} k_l(l - l_0)^2 + \sum_{angles} k_\theta(\theta - \theta_0)^2 + \\ & \sum_{dihedrals} \sum_n \frac{1}{2} V_n [1 + \cos(n\phi - \gamma_n)] + \\ & \sum_{j=1}^{N-1} \sum_{i=j+1}^N \epsilon_{ij} \left[\left(\frac{r_{0ij}}{r_{ij}} \right)^{12} - 2 \left(\frac{r_{0ij}}{r_{ij}} \right)^6 \right] + \frac{C q_i q_j}{r_{ij}} \end{aligned} \tag{2.2}$$

The terms defining the total potential, V , represent, in order, bond, angle, torsion, Lennard-Jones and electrostatic potentials. Bond length, equilibrium bond length and the bond stretching constants are given as l , l_0 and k_l , respectively. The bond angle, θ , has its parameters defined similarly. The dihedral potential for every dihedral in the system with dihedral angle ϕ is a sum over a number of n Fourier components. Each n value is associated with an amplitude, V_n , and phase shift γ_n . The Lennard-Jones potential, summed over atom combinations with separation r_{ij} , have a potential well depth parameter ϵ_{ij} and equilibrium distance r_{0ij} . The Coulombic interaction is defined for pairs of atoms with charges of q_i and q_j at a separation of r_{ij} with constant $C = \frac{1}{4\pi\epsilon_0}$. The non-bonded contributions of the first term are only calculated for atom combinations not connected in a bond or angle. Coulomb and van der Waals “1-4” interactions are scaled with factors of 5/6 and 1/2, respectively.

The GAFF force field is compatible with the AMBER99 force field in that they share non-bonded parameters of the Lennard-Jones and electrostatic potentials, the last term in Equation 2.2. Those non-bonded parameters are not given here as they are the same parameters that have been used in previous TBP models with AMBER99[50]. The bonded parameters, which compose the first three terms of Equation 2.2 that determine intramolecular atomic interaction, are different from those of the AMBER99 force field and are provided below.

Figure 2.1 shows the AMBER nomenclature used for the TBP and DAAP atoms in this paper. The bonded parameters used for TBP and DAAP are given in Table 2.1, Table 2.2 and Table 2.3. These bond, angle and dihedral parameters are taken from GAFF, except for the notable deviation in the dihedral parameters when phosphorus is one of the two center atoms. This dihedral adjustment is discussed with the matching of the experimental dipole value in the results section.

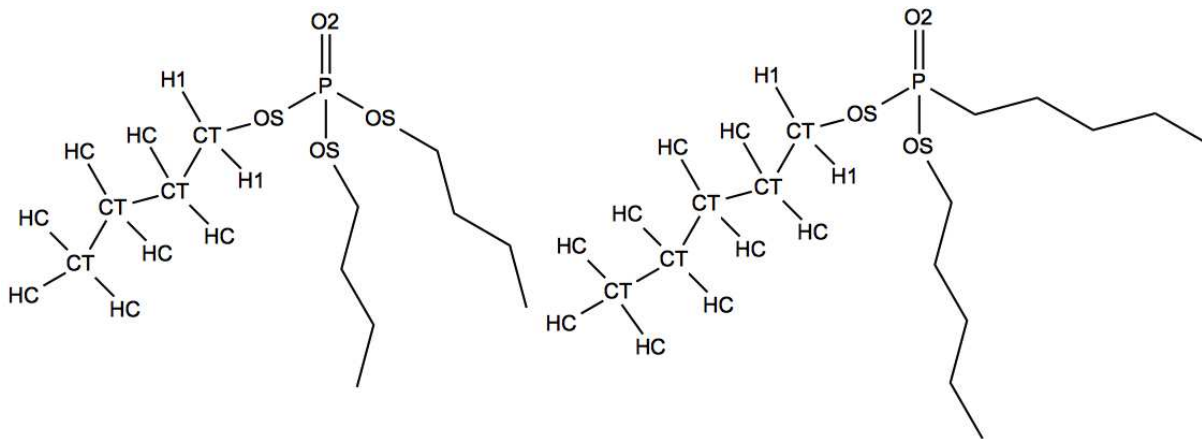


Figure 2.1: AMBER atom type designations for TBP (left) and DAAP (right).

In the literature, atomic charges for TBP models have been calculated with density functional theory (DFT) and semi-empirical electronic structure calculations[50]. Here, the semi-empirical method Austin Model 1 (AM1), with the bonded charge correction (BCC), was implemented to calculate TBP, DAAP and alkane diluent charges. This technique is intended for use with the GAFF force field[85, 86].

Table 2.1: GAFF equilibrium bond length and bond energy parameters.

Bond	l_0 [Å]	k_l [kcal mol ⁻¹ Å ⁻²]
O2-P	1.481	487.7
P-OS	1.602	342.5
P-CT	1.813	259.7
OS-CT	1.439	301.5
CT-CT	1.535	303.1
CT-H1	1.093	335.9
CT-HC	1.092	337.3

Table 2.2: GAFF equilibrium angle and angle energy parameters.

Angle	θ_0 [deg]	k_θ [kcal mol ⁻¹ deg ⁻²]
O2-P-OS	116.09	44.0
O2-P-CT	112.50	39.9
OS-P-OS	102.46	45.2
OS-P-CT	103.83	40.6
P-OS-CT	118.00	78.5
P-CT-CT	114.24	77.0
P-CT-H1	109.64	53.8
OS-CT-CT	108.42	67.8
OS-CT-H1	108.82	50.8
CT-CT-CT	110.63	63.2
CT-CT-H1	110.07	46.4
CT-CT-HC	110.05	46.4
H1-CT-H1	109.55	39.2
HC-CT-HC	108.35	39.4

Table 2.3: GAFF equilibrium dihedral angle and dihedral energy parameters. Asterisk indicates modified parameters.

Dihedral	n=1		n=2		n=3	
	V_n [kcal mol ⁻¹]	γ_n [deg]				
O2-P-OS-CT*	2.00	180	3.00	180		
O2-P-CT-CT*			0.80	180		
O2-P-CT-H1*			0.80	180		
OS-P-OS-CT*	2.00	180	3.00	180		
OS-P-CT-CT*			0.80	180		
OS-P-CT-H1*			0.80	180		
CT-P-OS-CT*			2.40	0		
P-OS-CT-CT					1.15	0
P-CT-CT-CT					1.40	0
P-CT-CT-HC					1.40	0
P-OS-CT-H1					1.15	0
OS-CT-CT-CT					1.40	0
OS-CT-CT-HC	0.25	0				
CT-CT-CT-CT	0.20	180	0.25	180	0.18	0
CT-CT-CT-H1					0.16	0
CT-CT-CT-HC					0.16	0
H1-CT-CT-HC					0.15	0
HC-CT-CT-HC					0.15	0

For each extractant and diluent, the molecular structure was geometry optimized with a DFT calculation using the B3LYP level of theory with the TZP basis set. AM1-BCC charges were generated by an AM1 single point calculation on that DFT optimized geometry. The BCC was applied in the form of an amount of charge moved between each pair of bonded atoms as determined by the bonded atom types. The BCC methodology and values for every pair of atoms in GAFF is given the literature by Wang *et al.*[86]. Table 2.4 gives the BCC values for the combinations of bonded atoms present in the TBP and DAAP molecules. BCC values, in fundamental charge units, are added to the first atom listed and subtracted from the second. Table 2.5 shows the calculated AM1-BCC charges used in these simulations for TBP and DAAP.

Calculations were performed in the MOPAC package[87] included in the Amsterdam Density Functional (ADF) software[88]. Calculated charges were averaged over the two or three symmetric *O(Butyl)* or *O(Amyl)* legs, for DAAP and TBP respectively, to remove differences between identically located atoms.

Table 2.4: BCC values for the bonded atom combinations that exist in TBP and DAAP.

Atoms	BCC [<i>e</i>]
O2-P	0.2707
OS-P	0.2336
CT-P	0.4078
CT-OS	0.0718
CT-H1	0.0393
CT-HC	0.0393
CT-CT	0.0000

2.3.2 Simulation systems and conditions

All molecular dynamics simulations were completed using the GROMACS 4.5.5 software package[89]. TBP, DAAP and diluent models were represented with all atom flexible models using periodic boundary conditions. Particle-Mesh Ewald summation was used for long range electrostatic summation. A 15 Å cut-off was used for short range electrostatics and van der

Table 2.5: TBP and DAAP AM1-BCC charge sets. For DAAP, charges for the two carbon tails with a bridging oxygen are listed together first with the third tail without an oxygen listed after.

Atom	AM1-BCC [e]
TBP	
O2	-0.7963
P	1.5955
OS	-0.5682
CT ₁	0.1644
CT ₂	-0.0834
CT ₃	-0.0814
CT ₄	-0.0921
H1 ₁	0.0467
HC ₂	0.0567
HC ₃	0.0417
HC ₄	0.0347
DAAP	
O2	-0.7863
P	1.3613
OS	-0.5782
CT ₁ (with OS)	0.1874
CT ₂	-0.0834
CT ₃	-0.0764
CT ₄	-0.0754
CT ₅	-0.0891
H1 ₁	0.0437
HC ₂	0.0547
HC ₃	0.0387
HC ₄	0.0387
HC ₅	0.0327
CT ₁ (no OS)	-0.2556
CT ₂	-0.0394
CT ₃	-0.0744
CT ₄	-0.0764
CT ₅	-0.0891
H1 ₁	0.0757
HC ₂	0.0467
HC ₃	0.0377
HC ₄	0.0377
HC ₅	0.0317

Waals interactions. All simulations were performed within the isobaric isothermal NPT ensemble using a leap-frog Verlet integrator. Pressure was set to 1 bar with the Berendsen barostat. The temperature was set to 300 K with the velocity-rescale modified Berendsen thermostat.

Neat TBP and DAAP simulations were carried out for 10 ns with a 1 fs time step starting from an initial configuration of a loosely packed $8 \times 8 \times 8$ lattice of randomly oriented extractant molecules. The initial lattice was energy minimized using a steepest descent algorithm. The extractant molecules condensed and equilibrated over the first 8 ns of simulation. Dipole and density data was taken as an average over the last 2 ns of simulation.

For mixed organic phase simulations, a lattice of extractant and diluent molecules was generated corresponding to the highest extractant concentration. This system was allowed to mix for 40 ns until equilibration under NPT conditions. Organic phase systems with lower extractant concentrations were generated from these coordinates through removal of the appropriate number of extractant molecules. Mixed organic phase simulations were run for 60 ns with a 2 fs time step, except for the lowest TBP concentration, corresponding to 0.04 M TBP or DAAP by volume, which was run for 80 ns. In both cases, data were recorded after an initial 10 ns equilibration period until the end of the simulation. The 0.04 M extractant organic phases were simulated three times to further improve statistics for the reported simulation dimerization value.

The list of mixed organic phase simulation compositions is provided in Table 2.6. The number of each type of molecule, diluent and resulting extractant concentration are provided. Each concentration was performed with the GAFF model as well as the AMBER99 TBP models explored in the literature by Cui *et al.* with both DFT and Modified Neglect of Differential Overlap (MNDO) calculated charge sets. Neat TBP data of the literature models were taken from their corresponding literature source, while mixed TBP/diluent organic phase dimerization data were generated in this study for those models.

Table 2.6: Extractant concentrations for organic phase simulations. Neat TBP, DAAP and mixed composition details.

Ext. conc. <i>mol/L</i>	<i>N</i> Ext. TBP/DAAP	<i>N n</i> -dodecane for TBP/DAAP	<i>N n</i> -octane for TBP/DAAP
Neat Ext.	512/512	—	—
0.97	105/108	350/412	—
0.23	20/20	350/412	—
0.18	15/16	350/412	—
0.15	12/12	350/412	—
0.12	10/10	350/412	—
0.10	8/8	350/412	—
0.08	7/7	350/412	—
0.06	5/5	350/412	—
0.04	3/3	350/412	—
0.97	105/108	—	489/576
0.23	20/20	—	489/576
0.18	15/16	—	489/576
0.15	12/12	—	489/576
0.12	10/10	—	489/576
0.10	8/8	—	489/576
0.08	7/7	—	489/576
0.06	5/5	—	489/576
0.04	3/3	—	489/576

2.3.3 Analysis methods and definitions

Average densities and molecular dipole moments for TBP and DAAP were computed for the neat extractant simulations. The instantaneous electric dipole moment vector for a molecule with a atoms is defined in Equation 3.1 where q_a and \mathbf{r}_a are the charge and position of atom a and \mathbf{r}_{COM} is the center of mass position of that molecule.

$$\mathbf{p} = \sum_a q_a (\mathbf{r}_a - \mathbf{r}_{COM}) \quad (2.3)$$

Extractant connectivity when assessing dimer and higher order aggregate formation was computed with ChemNetworks. Graph analysis of MD trajectories was assessed every 200 ps. That sampling frequency was chosen to match the observed correlation time of extractant dimers so as not to sample too often and process redundant information while simultaneously not sampling too rarely and discarding useful data. An edge between two extractant molecule vertices was defined for ChemNetworks as occurring when the O2 phosphoryl oxygen atoms of two molecules are within 5.5 Å of each other. The choice of cut-off distance and exclusion of an inter-dipole angle requirement to the dimer definition are discussed in the results section. A list of edges was produced in each system at each sampling time step. Those results were analyzed with code developed for this study to determine the average relative occurrence and average coordination number of each graph size. The average coordination number, the average number of edges extended from the vertices of a given graph, is defined for a graph as twice the total number of edges in the graph divided by the number of vertices. For example, a linear trimer consists of three vertices connected by two edges results in an average coordination number of 4/3. If the first and third vertices were also connected, the average coordination number for the graph would increase to 2. Thus, a higher average coordination corresponds to a more nonlinear graph.

2.4 Results

2.4.1 Neat TBP and DAAP simulations

The neat liquid phase GAFF/p TBP and DAAP simulations were completed to provide model validation through comparison to the default GAFF models as well as data given in the literature for the scaled and unscaled AMBER99 TBP models[50], the GAFF/vdw TBP model[58] and experimental values of density[90] and average molecular dipole moment[91–93]. Table 2.7 shows those results. The density for the GAFF/p model presented here is similar to the GAFF/vdw and AMBER99 models, within 1% the experimental value.

The unscaled average molecular dipole values for AMBER99 models are significantly higher than the experimental value. This difference led Cui *et al.* to apply a scaling factor of 0.7 for the AMBER99/DFT model and 0.6 for the AMBER99/MNDO model to the calculated atomic charges[50]. The Coulombic scaling is chosen such that the resulting dipole is within the experimental range, with their results shown in Table 2.7 denoted with an asterisk. Using the default GAFF parameters, the TBP dipole is underpredicted with a value of 2.90 ± 0.04 debye. The GAFF/vdw TBP model generated by Vo *et al.* increased the dipole by altering the O2 van der Waals parameters: the potential well radius was increased while the well depth was significantly reduced. The resulting dipole is higher than the experimental range, although less so than the unscaled AMBER99 models[58].

Altering the O2 van der Waals parameters, however, will impact the inter-molecular interactions and structuring, making it not ideal for the organic phase simulations of interest. As addressed in the following section, the dimerization constant obtained by Vo *et al.* is lower than the experimental value. This is attributed to the reduced attractive potential of the O2 atom that is relevant to the head-to-head dimer interactions. To match the experimental dipole without impacting the intermolecular potentials that influence dimerization, we instead change the intramolecular potential via the dihedral parameters. The dihedral pa-

rameters in GAFF are not as well characterized as in AMBER99 as most GAFF dihedrals, including all phosphorus-containing dihedrals, are defined only by the central two atoms. Thus, the default GAFF dihedrals are only approximate and a likely source of the GAFF TBP model deviations from the experimental TBP behavior vis-à-vis the average molecular dipole.

We hypothesize that to correct the underpredicted dipole given by the default GAFF parameters, we should increase the separation of the negative TBP head group from the net positively charged tails. For the GAFF/p model, we increased the phosphorus-containing torsion potentials such that the carbon tail orientations are now more extended. The relative atomic positions within the rather rigid head group were unchanged, but the resulting change in the carbon tail orientations led to a shift of the average TBP center of mass approximately 0.1 Å away from the head group. A similar magnitude of change in the distance to the molecular center of mass was also observed in the carbon tails. The more rigid torsion potentials thus increased the dipole by increasing the separation of the positive and negative portions of the TBP molecule. We calculate the GAFF/p dipole to be 3.28 ± 0.02 debye at 300K, which is in close agreement with the experimentally measured values of 3.28, 3.32 and 3.35 debye. A dipole value of 3.67 debye has also been reported for TBP[94], but this value is significantly higher than the other reported values and is considered an outlier. While the values of 3.35 and 3.67 debye were obtained at 25° C instead of 20° C for 3.28 and 3.32 debye, the 5° change in temperature is not expected to result in a significant enough increase to justify inclusion of the outlier value. To verify this, we performed simulations at both 20° and 25° C and found the dipole increased by only 0.01 debye, which is within the measurement uncertainty.

The GAFF DAAP model presented here further supports the validity of using the modified torsion parameters. While the DAAP model accurately replicates the density, using the default GAFF dihedral parameters for phosphorus-containing dihedrals results in a dipole of 4.19 ± 0.04 debye. This value overestimates the dipole when compared to the estimated

experimental range of 3.1 ± 0.2 debye calculated with unpublished data using the Onsager equation[92]. By using the same modification to the dihedral parameters, a simulation dipole of 2.94 ± 0.03 debye is obtained, which falls within the experimental range. The phosphorus containing dihedrals, as a result of the missing bridging oxygen and resulting phosphoryl group asymmetry, are not the same dihedrals that exists in TBP. The improved computational and experimental agreement that occurs as a consequence of the modified phosphorus torsion terms for the TBP and DAAP GAFF supports that using this adjustment is robust and transferable to other trialkyl phosphate- or phosphonate-type extractants.

Other metrics have been applied for TBP model validation in the literature including heat of vaporization and density change with TBP volume fraction in *n*-dodecane. These properties are of interest, but for the intended application of assessing organic phase aggregation of trialkyl phosphate and phosphonate extractants, replication of the electric dipole and dimerization constant may be more appropriate properties to validate. The excess volume of mixing TBP and *n*-dodecane, as assessed by Cui *et al.* for the AMBER99 models in the literature[53], is less than 1% of the total combined volume. They asserted that correctly predicting the sign of the volume change indicates successful model behavior. For the GAFF/p model the excess volume of mixing for the 0.97 M TBP and DAAP systems were positive but overpredict the TBP experimental value at $5.1 \text{ cm}^3/\text{mol}$ and $7.9 \text{ cm}^3/\text{mol}$, respectively, compared to an experimental value of $0.6 \text{ cm}^3/\text{mol}$ for TBP at 0.3 mole fraction TBP.

The heat of vaporization for the GAFF/p TBP and DAAP were calculated as 25.3 ± 0.5 and 28.2 ± 0.9 kcal/mol, respectively. The value for TBP is higher than the experimental value of 22.7 kcal/mol but close to the value reported by Vo *et al.* for the default GAFF parameters. The GAFF/vdw model, which was fit to the density and heat of vaporization by adjusting the attractive portion of the LJ potential, gives a value of 24.08 ± 0.04 kcal/mol for the TBP heat of vaporization. While this method will lower the heat of vaporization, as the short range LJ potential is the most significant energy contribution difference between

the liquid and gas phases, maintaining intermolecular potentials that govern aggregation behavior, such as dimerization as discussed in the following section, is of more concern for the GAFF/p model. Furthermore as discussed by Vo *et al.*, the default GAFF parameters result in a “gel” phase for the pure alkane, where the diluent molecules adopt a stacked structure. Instead of avoiding this unphysical behavior through LJ attractive potential adjustment as utilized by Vo *et al.*, we modified the torsion potentials for the *n*-dodecane and *n*-octane models to omit dihedrals with atom combinations consisting of two hydrogen atoms. The density and heat of vaporization for the dihedral-adjusted *n*-dodecane model are 732 ± 0.5 kg/m³ and 16.9 ± 0.1 kcal/mol, respectively, compared to experimental values of 744 kg/m³ and 14.7 kcal/mol[58]. Though not matching as closely as the LJ-adjusted model used by Vo *et al.* fit to the density and heat of vaporization, the values for these properties are still reasonable.

Table 2.7: Simulation density and dipole for neat TBP and DAAP liquids. Default GAFF, GAFF/p, GAFF/vdw, AMBER99 and scaled AMBER99 literature TBP models are compared with experimental values. Percent error with respect to the corresponding value is given for each simulation result. The asterisk denotes literature models with atomic charge scaling factors.

Molecule	Data source	Dipole (<i>debye</i>)	Percent difference	Density (<i>kg/m</i> ³)	Percent difference
TBP	experiment[90–93]	3.28-3.35	—	972.1	—
TBP	GAFF/p	3.28 ± 0.02	1 ± 1	980 ± 2	0.8 ± 0.2
TBP	default GAFF	2.90 ± 0.04	13 ± 1	980 ± 2	0.8 ± 0.2
TBP	GAFF/vdw[58]	3.58 ± 0.34	8 ± 10	971 ± 7	0.1 ± 0.7
TBP	AMBER99/DFT[50]	3.91 ± 0.11	18 ± 3	984	1.2
TBP	AMBER99/MNDO[50]	4.97 ± 0.11	50 ± 3	981	0.9
TBP	AMBER99/DFT*[50]	2.99 ± 0.04	10 ± 1	980	0.8
TBP	AMBER99/MNDO*[50]	3.23 ± 0.04	3 ± 1	975	0.3
DAAP	experiment	3.1 ± 0.2	—	928[95]	—
DAAP	GAFF/p	2.94 ± 0.03	5 ± 1	927 ± 1	0.1 ± 0.1
DAAP	default GAFF	4.19 ± 0.04	35 ± 1	927 ± 1	0.1 ± 0.1

2.4.2 Extractant/Diluent Organic Phase Simulations

Snapshots of GAFF/p TBP aggregates in *n*-dodecane are shown in Figure 2.2. Figures Figure 2.2a-c show the two dimers in solution in the 0.12 M simulation. The diluent is not shown for clarity. The dipole of a given TBP molecule approximately points along the P=O axis that connects the highlighted phosphorus and phosphoryl oxygen atoms, shown in green and red respectively. The angle between the dipoles of the TBP molecules in the dimers here is close to 180 degrees. Note the offset between the two P=O axes, presumably to lessen the local electrostatic repulsion between the phosphoryl O2 oxygen atoms. Figures Figure 2.2d-f show a linear timer, a cyclic trimer and a tetramer from the 0.97 M simulation.

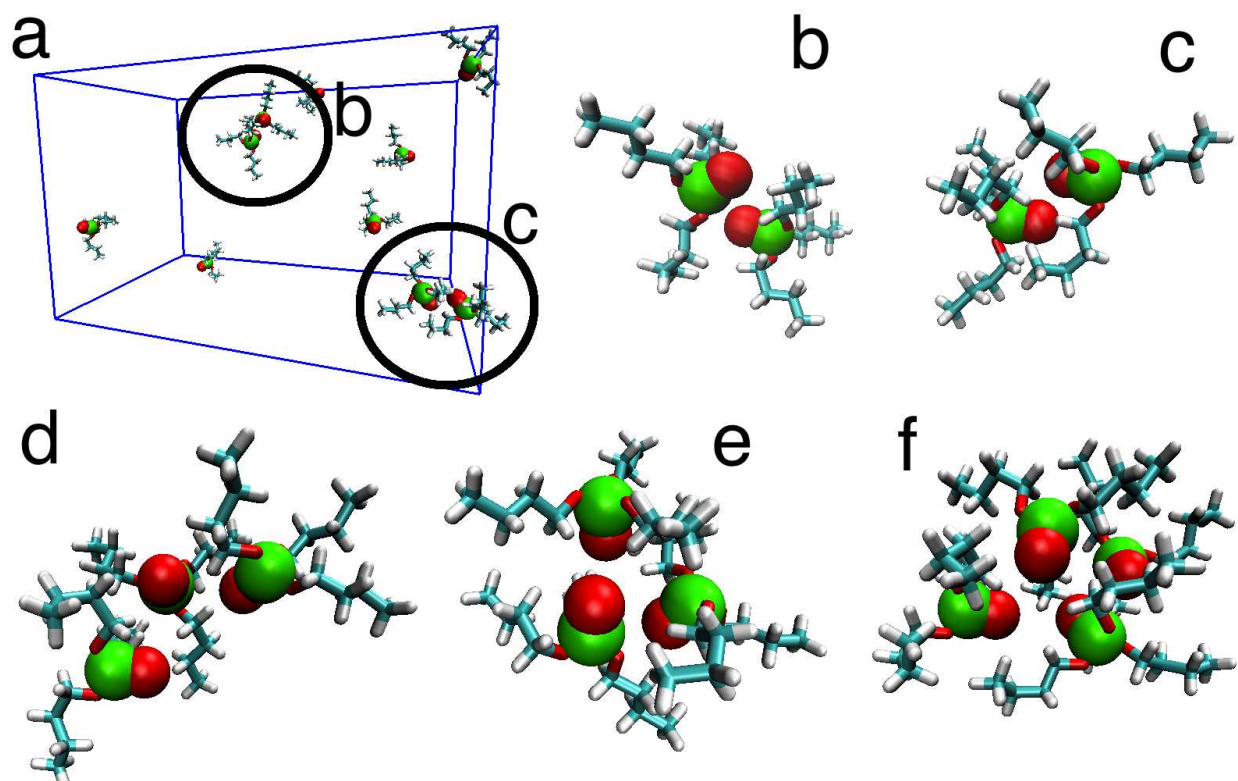


Figure 2.2: a) Snapshot of 0.12 M GAFF/p TBP in *n*-dodecane, with the two dimers in the simulation, circled in frame a, shown enlarged in b and c. d-f) A linear timer, a cyclic trimer and a tetramer from the 0.97 M TBP simulation. Diluent is omitted for clarity. Oxygen atoms are depicted in red, phosphorus in green, and carbon tails in blue and white for carbon and hydrogens, respectively.

Structure and aggregation, including dimerization, measurements of TBP and DAAP in *n*-dodecane and *n*-octane organic phases were calculated for the GAFF/p model as well as both scaled AMBER99 literature TBP models. To capture the structure of TBP and DAAP aggregates and ensure the connectedness criterion defining an edge does not over- or undercount interactions, the distribution of relative positions and orientations of TBP and DAAP molecules is measured. The question of what cut-off to use in identifying dimers and whether or not to include an orientation restriction on the dimer definition was addressed by plotting the distribution of O2-O2 atom distances and angles between the P=O bond. The angle between two TBP dipoles is defined such that two head-to-head molecules, where the O2 atoms are facing each other, is $\theta = 180$ degrees. A head-to-tail orientation corresponds to $\theta = 0$ degrees. The inset in Figure 2.3 shows a schematic of these orientations.

The orientation and distance distribution plots are shown in Figure 2.3a, b and c for the 0.97 M TBP, 0.97 M DAAP and 0.04 M TBP in *n*-dodecane simulations. Note that all configurations are recorded in these data, not just those that qualify as belonging to an aggregate. Furthermore, these distributions are normalized by a factor of $4\pi r^2 \sin(\theta)$ according to the differential volume at a particular value of θ and r . The color schemes for the 0.97 M TBP and DAAP panels are normalized to molecule number to allow for direct comparison between extractants. The color bar gives the orientation probability density normalized with a $2\pi r^2 \sin(\theta)$ factor such that the total number of counts over the range of 0 to 360 degrees and 0 to 8 Å is equal to unity. Analogous plots for the other extractant, concentration and diluent combinations, while not given here, contained similar features. While the number of individual configurations is low for the 0.04 M plot, resulting in less signal to noise, the position and angle dependence are similar to those in the 0.97 M system. Thus, the fundamental TBP and DAAP interactions of dimer pairs in dilute conditions is similar to those in the high order aggregations at high extractant concentrations studied here.

The region of most frequently observed angle and distance combinations occurs above 150 degrees with a tail extending down to lower angles, within a distance range of 3 to 5.5 Å. The population of head-to-tail configurations was not significant, and tail-to-tail dimers, with an inter-dipole angle near $\theta = 0$ and a O2-O2 distance range larger than the range found for head-to-head dimers, were not observed. Radial distribution functions (not shown) for O2-O2, P-P and O2-P pairs in pure TBP have peaks at 4.7, 5.9 and 5.1 Å respectively. These distances reflect configurations in which the P=O2 dipoles between interacting TBP molecules are aligned such that the four P and O2 atoms form a quadrilateral where the average O2-O2 and O2-P distances are shorter than the P-P distance. These measurements and observations in the dimer and aggregate snapshots indicate that extractant dimers form primarily in a nearly head-to-head orientation with the molecular axes offset from each other presumably due to O2-O2 repulsion, as has been previously proposed[53, 58].

The inter-dipole angle versus O2-O2 distance distribution plot for DAAP, shown in Figure 2.3b looks similar to the plot for TBP but with fewer total counts in the peak region. Note that the presence of unexpected high counts near 0 and nearly 180 degrees, as well as for low O2-O2 r values, reflects a greater noise level due to the proportionally lower number of configurations at the polar angles and small radial distances compared to intermediate angles and larger radii. In the 0.4 M TBP system, dimers were observed from viewing the trajectories to be transitory and persist from 1 to 5 ns. Larger aggregate lifetimes, marked by transitions between N-mers to (N-1)- or (N+1)-mers, were more transient. Trimer lifetimes observed in the 0.23 M TBP simulation ranged from 0.24 to 1.2 ns. Larger aggregates than trimers were not observed in sufficient quantity to report a meaningful lifetime range.

The cut-off distance of 5.5 Å specified in the Methods is determined by this distribution plot. The cut-off needs to encapsulate all of the relevant extractant interactions while not extending so far that extraneous extractant pairs are counted. This plot indicates that there is a clear delineation in distance between dimer interactions and noise, lending confidence to the choice of cutoff used in the dimer definition. There is no orientation restriction used

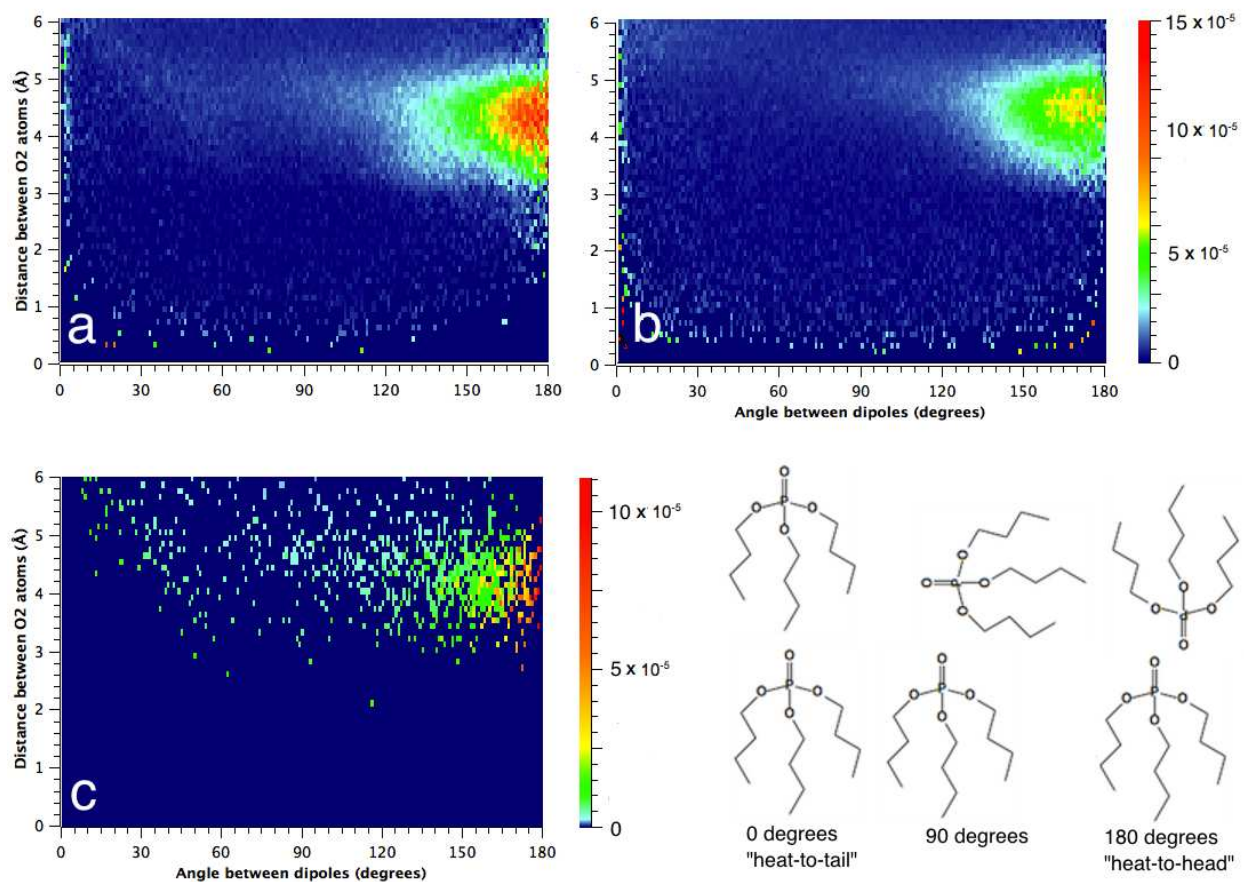


Figure 2.3: Angle versus distance frequency plot for GAFF/p 0.97 M TBP, 0.97 M DAAP and 0.04 M TBP in *n*-dodecane, shown in a, b and c respectively. The orientation convention is also illustrated. The color bar indicates the normalized count density in units of $\text{Å}^{-1} \text{deg}^{-1}$.

here because, while the nearly “head-to-head” orientation is preferred for both high and low concentration systems, at low concentration there are interactions observed over the entire orientation range. Furthermore, as observed in Figure 2.2d-f, there are TBP orientations outside of the “head-to-head” region in the pictured trimers and tetramer. To identify these aggregates while using the same criterion for all inter-extractant interactions, no orientation restriction was applied.

To validate the GAFF/p TBP model’s ability to accurately replicate organic phase self-interaction, the simulation dimerization constant is calculated and compared to the experimentally determined value. The dimerization constant is defined as the equilibrium constant for the dimerization reaction shown in Equations 2.4 and 2.5.



$$k_{dim} = \frac{[\text{TBP}_{dim}]}{[\text{TBP}_{mon}]^2} \quad (2.5)$$

The experimental dimerization constant was measured for dilute TBP at 0.01 M concentration in *n*-dodecane to be $2.6 \pm 0.1 \text{ (mol/L)}^{-1}$ [94, 96]. As the IR spectroscopy method used to determine this dimerization constant does not distinguish between TBP in dimers or larger aggregates, a value for the dimerization constant was computed using data from dilute TBP concentrations where the concentration of higher order aggregates are negligible. Nonetheless, this dimerization constant can still be expected to describe the monomer/dimer ratio given in Equation 2.5 even at higher TBP concentrations, where there are simultaneous equilibria with higher order TBP aggregates. Thus, even though it is too computationally expensive to simulate the dilute system for long enough time to achieve sufficient statistics, the dimerization constant can still be assessed from the systems simulated here.

The dimer concentration at each total extractant concentration from 0.04 to 0.23 M for the GAFF/p TBP model is plotted in Figure 2.4. In Figure 2.4 we also plot values for the dimer concentration from the experimental dimerization constant assuming there are only monomers and dimers comprising the total TBP concentration. Once the TBP concentra-

tion reaches a value where higher order aggregates are non-negligible and the total TBP concentration does not consist only of monomers and dimers, the experimental Equation 2.5 low-concentration extrapolation line overpredicts the dimer concentration. Dimer concentrations measured in simulation using the modified AMBER99 literature models and the GAFF/p DAAP model are plotted for comparison.

Note the total concentration values in Figure 2.4 are corrected for the finite size of the simulation systems. The actual concentration observed by a single extractant molecule other than itself deviates from the nominal concentration for a small number of extractant molecules, i.e. when $(N - 1) \approx N$ is not valid. For the dimer concentration calculations, the total extractant concentration is thus corrected by a factor of $N(N - 1)/N^2$ to obtain the effective concentration.

For *n*-dodecane, shown in Figure 2.4a, agreement between extrapolated experimental dimerization and GAFF/p model dimerization is excellent through 0.18 M TBP, after which the simulation dimer concentration is lower than the extrapolated experimental value for reasons discussed above. The modified AMBER99/DFT and AMBER99/MNDO models underpredict the dimerization at all concentrations. The DAAP dimerization is lower, although not significantly, than TBP for the GAFF/p models at nearly every concentration. To the authors' knowledge there is no experimental dimerization constant for DAAP to compare the simulation values.

The dimerization constants were directly computed from Equation 2.5 using the simulation dimer and monomer concentrations obtained with the aggregate graph analysis and plotted in Figure 2.4c at each of the simulated concentrations. Average values for the dimerization constants taken over all concentrations from 0.04 to 0.23 M are given in Table 2.8. The GAFF/p TBP model gives a simulation dimerization constant of $2.8 \pm 0.8 \text{ (mol/L)}^{-1}$, quite close to the experimental value of $2.6 \pm 0.1 \text{ (mol/L)}^{-1}$. The dimerization constant of the GAFF/vdw TBP, assessed by Vo et al., was $1.2 \pm 0.03 \text{ (mol/L)}^{-1}$ [58]. This value is presumed to be lower than the dimerization constant for the GAFF/p model due to the

reduced van der Waals potential on the O2 atom. Vo *et al.* also report a value of 2.2 ± 0.5 , although that value is calculated by counting higher order aggregates as dimers. The AMBER99 models both significantly underpredict the dimerization constant. These dimerization constants and those calculated for the modified AMBER literature models are given in Table 2.8.

Table 2.8: Dimerization constants calculated from simulation for GAFF/p and scaled AMBER99 TBP models are given with the experimental and GAFF/vdw[58] values. Computed GAFF/p DAAP dimerization constants are also given. Percent error is given relative to the corresponding experimental value, if applicable.

Molecule	Data source	Diluent	Dimerization constant (mol/L) ⁻¹	Percent difference
TBP	experiment[94, 96]	<i>n</i> -dodecane	2.6 ± 0.1	—
TBP	GAFF/p	<i>n</i> -dodecane	2.8 ± 0.8	8 ± 30
TBP	GAFF/p	<i>n</i> -octane	2.6 ± 0.5	0 ± 20
TBP	GAFF/vdw[58]	<i>n</i> -dodecane	1.2 ± 0.03	50 ± 1
TBP	AMBER99/DFT[50]	<i>n</i> -dodecane	0.19 ± 0.04	93 ± 2
TBP	AMBER99/MNDO[50]	<i>n</i> -dodecane	0.07 ± 0.02	97 ± 1
TBP	AMBER99/DFT[50]	<i>n</i> -octane	0.20 ± 0.05	92 ± 2
TBP	AMBER99/MNDO[50]	<i>n</i> -octane	0.09 ± 0.03	97 ± 1
DAAP	GAFF/p	<i>n</i> -dodecane	1.7 ± 0.5	—
DAAP	GAFF/p	<i>n</i> -octane	1.3 ± 0.3	—

Dimerization in *n*-octane for all models is plotted in Figure 2.4b. The experimental dimerization constant is assumed to be the same as that for *n*-dodecane[15]. The actual value is expected to be slightly higher, as it would likely fall between the reported values for *n*-dodecane (2.6 ± 0.1) and hexane (2.9 ± 0.1)[96]. Here, the GAFF/p model and calculated experimental dimer concentrations are in excellent agreement up to 0.15 M TBP. The modified AMBER99 literature models underpredict dimerization at all concentrations. At 0.04 M TBP, the GAFF/p model gives a dimerization constant of 2.6 ± 0.5 . These values are also given in Table 2.8.

Assessment of the increasing appearance of higher order aggregates other than dimers in the range of 0.04 to 0.23 M TBP is necessary to understand and characterize the low concentration TBP behavior. Extractant aggregates are defined through the graph con-

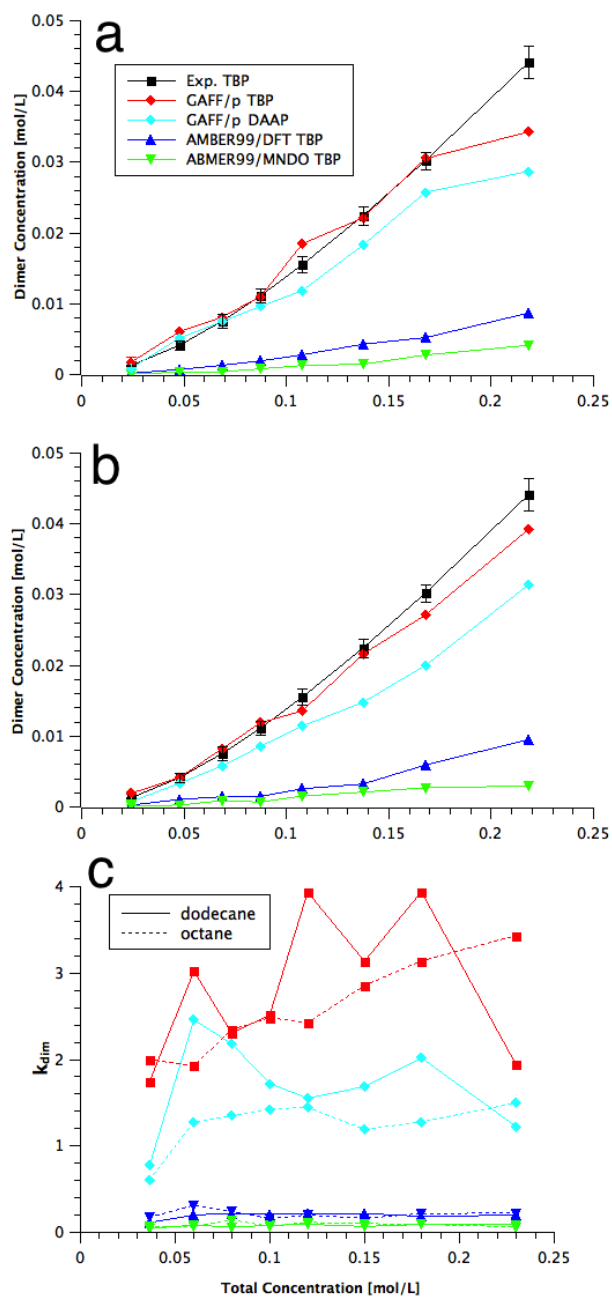


Figure 2.4: The dimer concentration versus total organic phase extractant concentration is plotted for each TBP and DAAP model and the extrapolated experimental value. Results for *n*-dodecane are given in a and *n*-octane in b. The dimerization constant for TBP and DAAP in both diluents at each simulated concentration is given in c.

nectivity criterion described in the Methods section. The concentration of each GAFF/p TBP or DAAP aggregate size that occurred in simulations for each of the four combinations of extractant and diluent are shown in Figure 2.5. Those plots show the number of each aggregate by size per extractant molecule. While no trimers are observed for the 0.04 M simulation, they are observed to a degree at each of the higher concentrations. Tetramers and pentamers were not significantly formed until after 0.1 M in these simulations. The speciation shows that TBP, while similar in the number of dimers formed, has notably higher occurrences of trimers and tetramers than DAAP over the same range of concentrations. The reduced aggregation of DAAP relative to TBP is suspected to result from increased steric crowding due to the additional alkyl tail length. The differences in speciation between diluents is not significant. It should be noted that the finite size effects that were corrected for in the dimer assessment apply here. For each aggregate size, the total concentration was adjusted to reflect the effective concentration observed in simulation by that size aggregate. As different aggregate sizes deplete the simulation box of extractant molecules to different degrees, the corrected concentration that a given aggregate is subjected to is dependent on aggregate size. The concentrations of each aggregate size were therefore scaled by a factor of $\prod_{i=1}^M (N + 1 - i)/N$ where N is the total number of extractant molecules in the system and M is the aggregate size. Therefore, for a given system with a nominal total extractant concentration, the corrected concentration is different for each aggregate size.

While low extractant concentration simulations are useful for validating model behavior with respect to the dimerization and observing the onset of higher order aggregation, the PUREX process is performed at roughly 1 M TBP. The complex TBP and DAAP self-interaction at that high concentration is difficult to assess experimentally. We characterize and quantify TBP and DAAP aggregation at those high concentrations. Figure 2.6a shows the aggregate size distribution for 0.97 M TBP and DAAP in *n*-dodecane and *n*-octane. The speciation depicted here for the PUREX-applicable 0.97 M extractant concentration shows trends similar to the low concentration systems: larger aggregates occur in greater

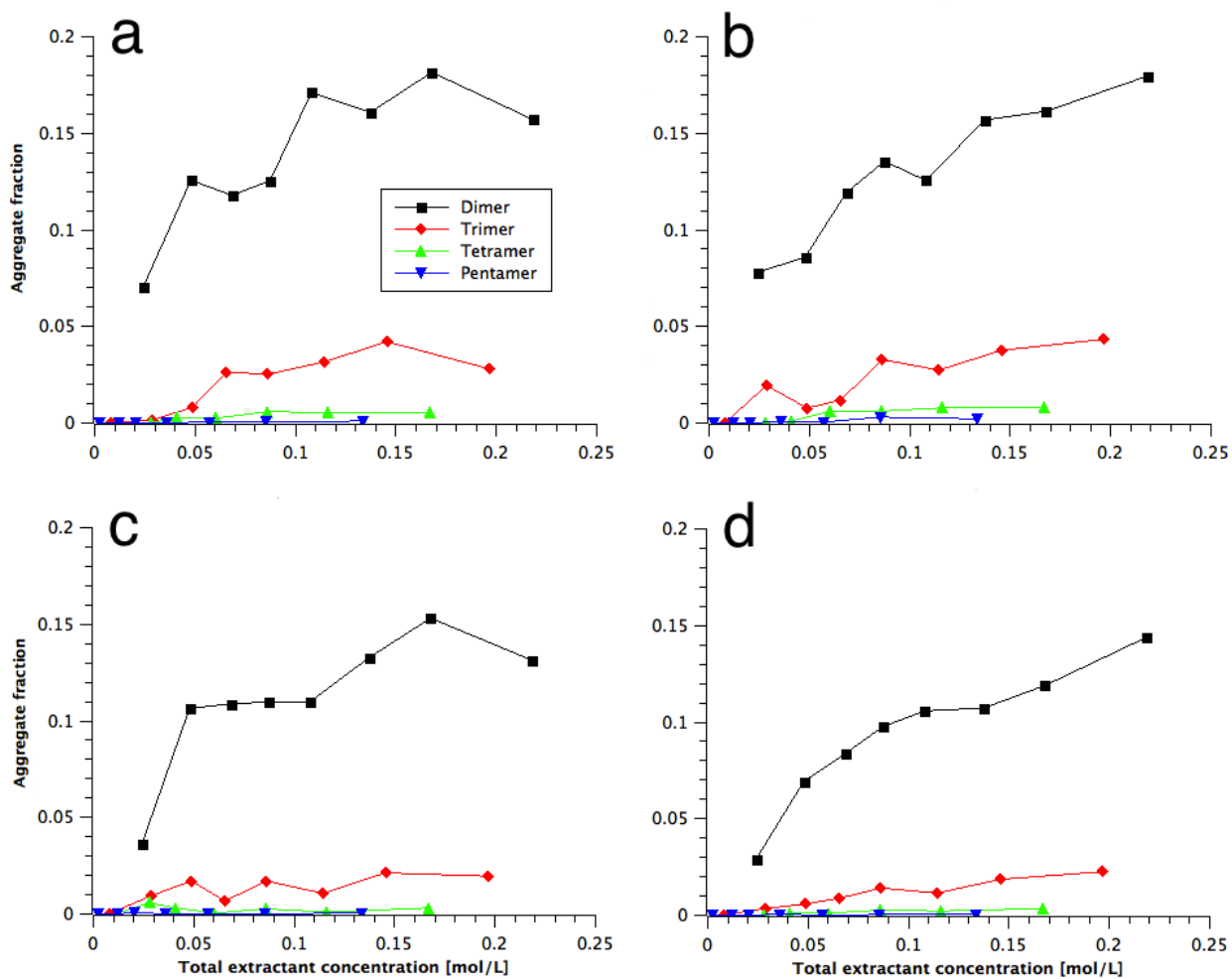


Figure 2.5: The speciation, in number per extractant molecule, of 2nd to 5th order TBP and DAAP aggregates are plotted for each extractant and diluent combination for a) TBP in *n*-dodecane, b) TBP in *n*-octane, c) DAAP in *n*-dodecane and d) DAAP in *n*-octane.

concentrations for TBP than DAAP in both diluents. The nearly linear trend of the log aggregate concentration versus aggregate size plot indicates that there is a characteristic probability associated with the incorporation of each successive extractant molecule that is approximately independent of aggregate size, and can be interpreted in terms of an association equilibrium constant. The equilibrium constant, k , is defined as the concentration of M -mer divided by the concentration of $(M - 1)$ -mer times the monomer concentration. It can be related to the difference in interaction mean free energy between an aggregate of size M and M monomers via the equation

$$k = e^{-M(\mu_M^0 - \mu_1^0)/k_B T}. \quad (2.6)$$

In the exponent, the difference in interaction mean free energy of an N -sized aggregate, $M\mu_M^0$, and M monomers, $M\mu_1^0$, is divided by Boltzmann's constant k_B times the temperature T . The concentration versus aggregate size data in Figure 2.6a were fitted to an exponential to evaluate $(\mu_M^0 - \mu_1^0)/kT$. For TBP in *n*-dodecane and *n*-octane, respectively, $(\mu_M^0 - \mu_1^0)$ is 0.55 and 0.59 kcal/mol per molecule. For DAAP, a value of 0.72 kcal/mol per molecule was obtained for both diluents, corresponding to the lower concentrations of the larger sized aggregates compared with TBP. The concavity of the log concentration versus aggregate size curve indicates that as the aggregate size increases, the interaction free energy increases slightly with increasing M . This may reflect the increasing steric penalty for aggregate formation at larger aggregate sizes that is not accounted for in Equation 4.4.

To further characterize aggregation in the high extractant concentration systems, the average coordination number, defined in the Methods section, in the aggregate graphs are shown in Figure 2.6b. With vertices representing the TBP or DAAP molecules, the average coordination number of those vertices is a measure of the nonlinearity or compactness of the aggregate. Figure 2.6b indicates that, in both diluents, the TBP systems have a higher average coordination number for all aggregate sizes than DAAP. Figure 2.6b also shows a linear reference graph, indicating the average coordination number of a completely linear aggregate of each size for comparison. In addition to forming trimer and larger aggregates

more frequently than DAAP, TBP aggregates of all sizes are more compact.

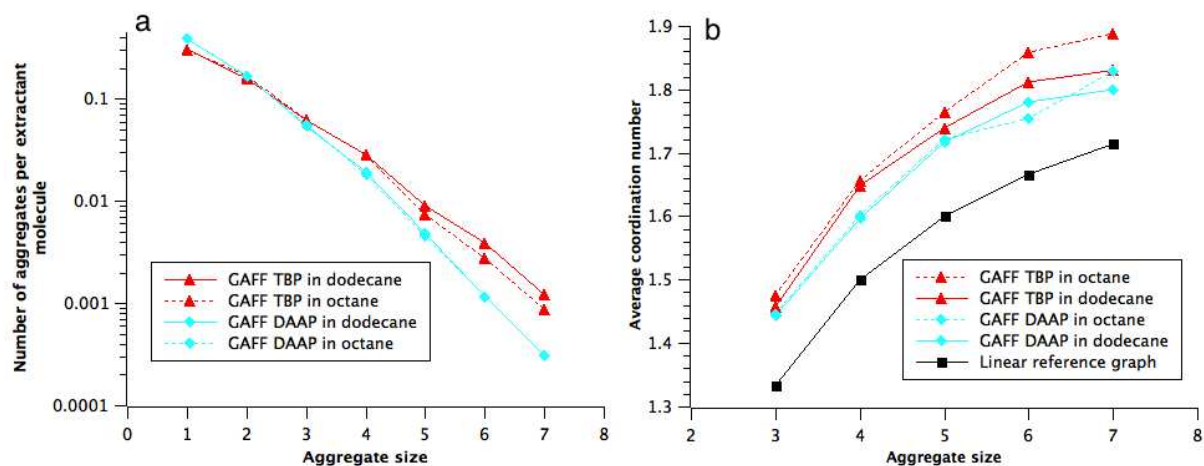


Figure 2.6: a) Average number of extractant aggregates per extractant molecule, for varying aggregate size. b) The average coordination number for each aggregate size. TBP and DAAP at 0.97 M in both *n*-dodecane and *n*-octane are plotted together in each panel.

2.5 Conclusions

A new TBP and DAAP model is presented for use in classical molecular dynamics, particularly in organic phase simulations, using the Generalized AMBER Force Field with an adjustment to the phosphorus-containing dihedrals. The AM1 semi-empirical method with a bonded charge correction is implemented for calculating partial atomic charges. The model's density, molecular dipole and dimerization constant are evaluated and compared to existing literature models and experimental data. Recent AMBER99 TBP models with Coulombic scaling, while matching the density and dipole, underpredicted dimerization. The GAFF/vdw TBP model, while similar to the one presented here, overpredicts the experimental dipole and underpredicts dimerization. In this paper, we show that both of these discrepancies are corrected when the generic dihedral potentials of GAFF are replaced with stiffer torsion parameters for phosphorus-containing dihedrals. These corrections were shown to correct the DAAP dipole as well from the overpredicted value given by the standard GAFF torsion potentials. To further modify the GAFF/p model to match experimental density and

heat of vaporization, we expect that a LJ potential parameter refinement could be performed while avoiding modifications that impact dipole and dimerization agreement rendered by the GAFF/p torsion adjustment.

Both extractants were simulated in *n*-dodecane and *n*-octane over a range of concentrations from 0.04 to 0.97 M to assess aggregate speciation and inter-extractant structure. DAAP and TBP self-interactions were found to exist primarily in the head-to-head orientation with an inter-dipole angle range of 150 to 180 degrees at an O2-O2 separation of 3 to 5.5 Å. Using output from the ChemNetworks software, a graph analysis was performed on the aggregate structures in the extractant/diluent simulations. The GAFF/p TBP dimerization constant assessed over the low concentration systems matched the experimental value, indicating that the GAFF/p model successfully replicates the fundamental organic phase self-interaction of TBP. Speciation of the extractant aggregates was measured at higher concentrations. While the choice of diluent did not significantly affect aggregation, DAAP did not form tetramer or larger aggregates as frequently as TBP presumably due to greater steric repulsion between its longer hydrocarbon tails. TBP aggregates at 0.97 M had larger average coordination numbers and thus were more compactly connected than equivalent DAAP aggregates. The probability distribution of aggregate size was approximately exponential, consistent with a fixed probability for each additional extractant molecule to be included in the aggregate, up to at least a 7-mer. The corresponding differences in interaction free energy between aggregates and their monomer components were determined for each extractant in each diluent. This trend, if valid for higher aggregates, would have implications for third phase formation. The combination of experimental agreement for the density, dipole and dimerization lend confidence to use of the GAFF/p TBP and DAAP models in simulations studying organic phase TBP self-interaction and aggregation.

2.6 Acknowledgements

The authors thank the Colorado School of Mines High Performance Computing center for computational resources and Nuclear Regulatory Commission Faculty Development Award

NRC-HQ-11-G-38-0062 for funding.

CHAPTER 3

THE ROLE OF SOLVENTS IN ORGANIZATION AND ASSOCIATION OF NEUTRAL ORGANOPHOSPHORUS EXTRACTANTS

3.1 Abstract

The choice of organic solvent is known to impact distribution and phase partitioning in solvent extraction systems, although study of this behavior has been largely qualitative. To provide a more quantitative and molecular scale understanding of extractant and solvent association in solvent extraction, molecular dynamics studies of binary extractant/solvent systems are conducted for several organophosphorus solvating extractants across a range of organic solvents. Classical molecular dynamics potentials are optimized for the extractants in pure phase simulations. These potentials are then validated with binary extractant/solvent solutions by comparison to experimental data for volume change on mixing and mixing enthalpies. The excellent agreement with available experimental data indicate these models are practical for systems where extractant-solvent mixing energetics drive extracted complex solubility and phase behavior. Trends in association free energy, mixing enthalpy and deviations from ideal mixing volume are reported for each extractant and solvent binary mixture. Contributions to those properties depending on extractant and solvent molecular structure are investigated, including the enthalpic favorability of extractant/toluene solutions compared to diethyl ether and *n*-hexane.

3.2 Introduction

In liquid-liquid solvent extraction, an amphiphilic extractant molecule in a nonpolar solvent selectively recovers metal ions from an acidic aqueous phase. The solubility of extractant-metal clusters in the organic phase impacts partitioning energetics as well as

the metal solubility limit before third phase formation[78]. In third phase formation, the organic phase splits into two phases, the heavier of which contains nearly all the extractant and extracted polar solutes while the lighter phase contains primarily the organic solvent. The molecular structure of the extractant and organic solvent molecules affects the solubility of those clusters, informs the polar solute partitioning and the maximum metal loading before phase splitting[4], and thus the efficiency per contact. While metal distribution to the organic phase and the limiting concentration before third phase formation have been shown to depend strongly on the extractant and solvent structures, predictive modeling of those properties is lacking.

In Plutonium Uranium Redox EXtraction (PUREX)-type solvent extraction processes, a solvating organophosphorus extractant, such as tributyl phosphate (TBP), in an hydrocarbon solvent is contacted with a nitric acid aqueous phase to selectively extract tetra- and hexavalent metal ions from trivalent ones. Extraction efficiency under high metal and acid loading, particularly approaching third phase formation, is affected by the aggregation chemistry of the extracted complexes[22]. For rare earth element extraction systems that employ multi-coordinate extractants, like octyl(phenyl)-N,N-diisobutylcarbamoylmethylphosphine oxide (CMPO), third phase formation and general organic solubility are even more relevant concerns[97]. Effectively modeling the impact of extractant and solvent structure on solubility will aid in the design of such extraction systems.

Rao *et al.* determined the limiting organic concentration (LOC) for thorium extraction by TBP in different organic solvents. This work identified empirical trends in aliphatic solvents where decreasing the chain length or introducing branching to the solvent increased the LOC, making the organic phase less prone to third phase formation[30]. Aromatic and alcohol-based solvents also exhibited an increased LOC compared to aliphatic solvents. Rao and coworkers also studied variation compared to TBP in the LOC for different organophosphorus extractants in *n*-dodecane, including triamyl phosphate (TAP), dibutyl butyl phosphonate (DBBP) and diamyl amyl phosphonate (DAAP)[31]. These four extractants are depicted

in Figure 3.1. They found that changing the butyl tail groups to amyl groups, as well as changing the polar head from a phosphate to phosphonate group, increased resistance to third phase formation.

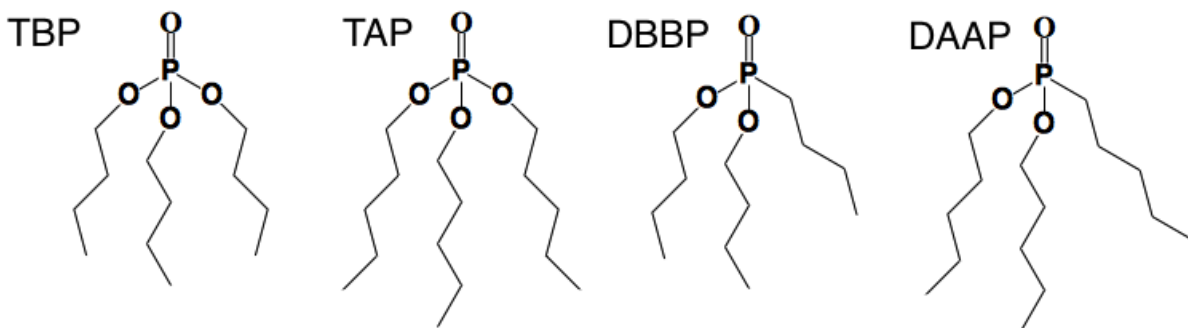


Figure 3.1: The molecular structure of: tributyl phosphate (TBP), triamyl phosphate (TAP), dibutyl butyl phosphonate (DBBP) and diamyl amyl phosphonate (DAAP).

To study these observed impacts of extractant and solvent structure on mixing energetics and mutual solubility, we conducted molecular dynamics (MD) simulations of binary solvent-extractant organic phases for different combinations of solvent and extractant molecules across a range of volume fractions. First, pure extractant and solvent systems are considered to optimize and validate extractant models with respect to experimental values of relevant pure phase physicochemical properties, including density, average molecular dipole and enthalpy of vaporization. An optimized Lennard-Jones potential for the carbon atoms on the butyl and amyl tail groups are fitted for the extractants for use in conjunction with the phosphorus-containing dihedral parameters previously reported for this class of extractants[98, 99]. The carbon atom L-J parameters were chosen for optimization to reduce the density and enthalpy of vaporization of the extractants because they have previously been optimized in the literature to reduce intermolecular attraction with *n*-dodecane that leads to an unphysical gel phase transition[58]. Using the optimized extractant models, properties of mixed phase simulations are investigated for each combination of extractant and diluent for a range of extractant volume fractions. The extractants are mixed with each of eight solvent

molecules: *n*-dodecane, *n*-decane, *n*-octane, *n*-hexane, 4-propyl heptane, toluene, diethyl ether and isopropanol. Additionally, benzene and ethyl propyl ether were simulated for a subset of the extractants and extractant volume fractions. Aliphatic diluents were selected to identify trends in linear chain length, from *n*-hexane to *n*-dodecane, and the impact of branching in the 4-propyl heptane. Toluene, diethyl ether and isopropanol are studied to investigate the impact of other extractant-solvent interactions, including molecular packing, polar interactions and hydrogen bonding. In the mixed organic phases, the extractant association free energy, enthalpy of mixing and volume change on mixing is measured and compared to available experimental data. Trends in those properties between extractants and solvents are discussed, with consideration to the polar and nonpolar extractant-solvent interactions present in those binary systems and how those interactions affect extractant-extractant association and extractant solubility. Validating molecular models and characterizing the binary phase extractant-solvent interactions and properties, including structure and solubility, will aid future research in rational design of solvent extraction systems.

3.3 Methodology

3.3.1 Force Fields

Extractant and solvent molecules were modeled with the Generalized AMBER Force Field (GAFF)[32] potential. The AM1-BCC method[85, 86] was used for deriving partial atomic charges for each extractant and diluent molecule using the methods we have previously reported[98]. Charges for the extractant molecules are given in Figure 3.2 and solvent molecules in Figure 3.3. Optimizations to the default parameters were made for both the extractant molecules and the alkane solvents and are described below.

For the extractants, we use previously reported adjustments to the phosphorus-containing dihedral parameters for the extractant molecules[98]. To further improve the pure phase thermodynamic properties of the extractants without impacting experimental agreement with

other properties like dimerization constant, in this study we optimized the Lennard-Jones parameters for the carbon atoms on the extractant alkyl tails. Dimer formation for the updated TBP and DAAP models is not significantly different from perviously reported values. We simulated the pure extractant systems for each extractant across combinations of σ and ϵ Lennard-Jones parameters for the carbon atom sites. To avoid inadvertent consequences of significantly deviating from the default parameters, we limited the parameter optimization scan to within 5% of the default values. The optimized σ and ϵ values were identified using a least squares criterion on the percent difference between simulation data and available experimental density, dipole and enthalpy of vaporization data. While the density data is available for each extractant, values for the other two properties are only available for TBP. Table 3.1 gives the experimental and optimized simulation values for the fitted properties. The best fit over the set of available data was achieved with scaling the default parameters by 96% and 103% for σ and ϵ , respectively, giving values of 3.2637 Å and 0.1127 kcal/mol.

The optimized carbon atom van der Waals parameters developed by Vo *et al.*[58] for *n*-dodecane, which prevent an unphysical gel phase transition that occurs with the default GAFF potential[58, 100], are used here for all alkane solvents. The density, molecular dipole moment and enthalpy of vaporization for the pure solvent system simulations are compared to available experimental data in Table 3.2. The GAFF parameters used here accurately replicate these properties across the range of solvent molecules investigated with a 1.1% average error.

The average molecular dipole is defined as the system time average of the instantaneous molecular dipole for that molecule type, given in Equation 3.1, where q_a and \mathbf{r}_a are the partial atomic charge and position of atom a and \mathbf{r}_{COM} is the center of mass of that molecule.

$$\mathbf{p} = \sum_a q_a (\mathbf{r}_a - \mathbf{r}_{\text{COM}}) \quad (3.1)$$

The enthalpy of vaporization, ΔH_{vap} , at a given temperature and pressure,

$$\Delta H_{\text{vap}} = H_{\text{gas}} - H_{\text{liquid}} = U_{\text{gas}} - U_{\text{liquid}} + p(V_{\text{gas}} - V_{\text{liquid}}) \quad (3.2)$$

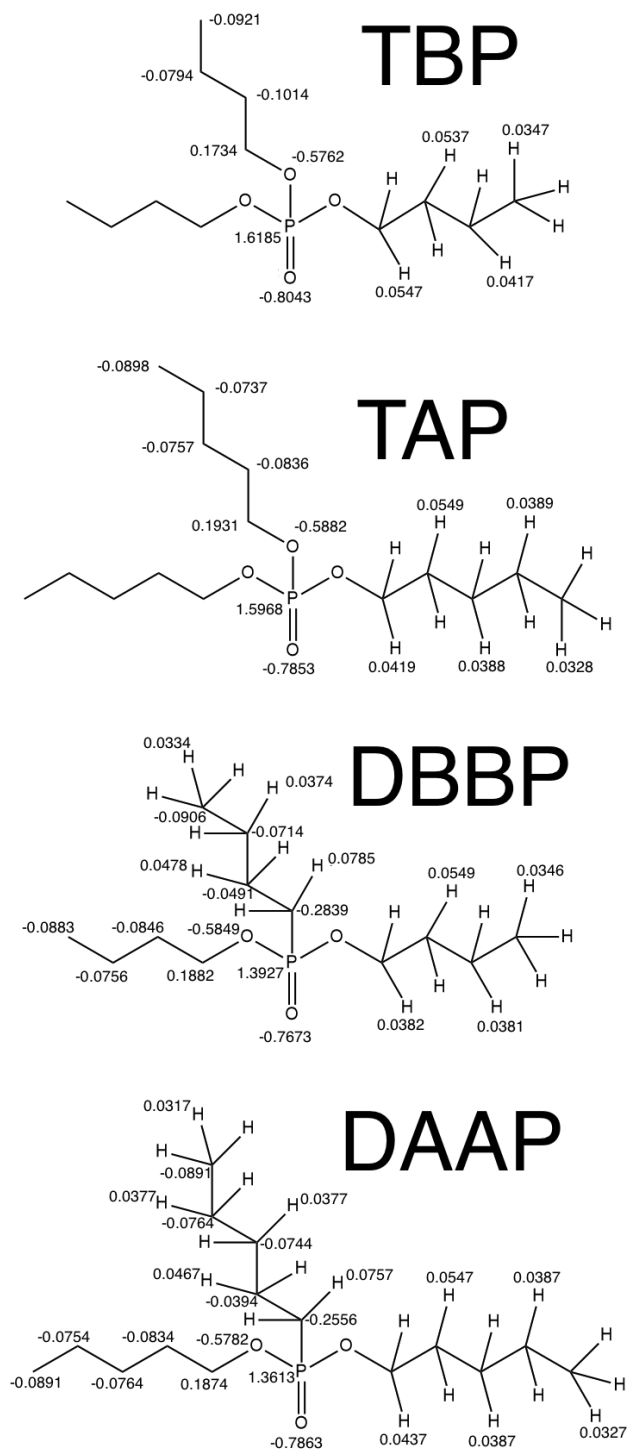


Figure 3.2: Atomic charges for the extractant molecules are given in fundamental charge units. Charges are only given once for symmetric atoms.

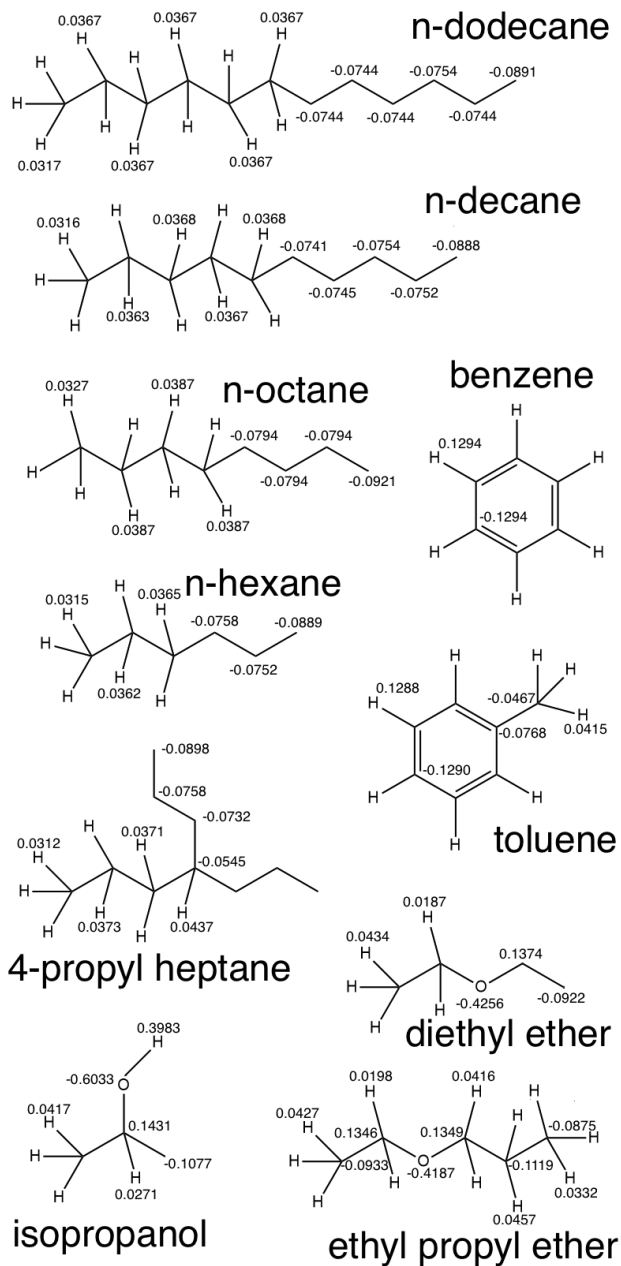


Figure 3.3: Atomic charges for the solvent molecules are given in fundamental charge units. Charges are only given once for symmetric atoms.

where H_{gas} and H_{liquid} are the gas phase and liquid phase enthalpies, U_{gas} and U_{liquid} the respective internal energies, p the pressure and $V_{\text{gas}} - V_{\text{liquid}}$ the change in volume upon vaporization.

Assuming the liquid phase volume is much smaller than the gas phase volume and ideal gas behavior, Equation 3.2 is simplified to

$$\Delta H_{\text{vap}} = H_{\text{gas}} - H_{\text{liquid}} = U_{\text{gas}} - U_{\text{liquid}} + RT \quad (3.3)$$

where R is the universal gas constant. The effects of non-ideal gas behavior are typically small compared to the total enthalpy of vaporization quantity and thus ignored in the simplification.

Table 3.1: Physiochemical properties for the four extractants, with available experimental data used in the optimization fitting, are given for the pure extractant systems with optimized force field potentials.

	Density <i>kg/m³</i>		Dipole <i>debye</i>		ΔH_{vap} <i>kJ/mol</i>	
	sim.	exp.	sim.	exp.	sim.	exp.
TBP	978±1	972.4[90]	3.348±0.003	3.28, 3.32, 3.35[91–93]	97.1±0.1	95.0[58]
TAP	952±1	937.3[101]	3.486±0.004		109.0	
DBBP	947±1	948[31]	2.884±0.005		86.7	
DAAP	918±1	929.1[95]	2.944±0.005		102.1	

3.3.2 Simulation Systems and Conditions

Molecular compositions for the simulations are given in Table 3.3. For the binary systems, the extractant volume fraction was varied from 5% to 90% with molecules numbers chosen for an approximately 250 nm³ simulation box size. The pure component system compositions are also given in Table 3.3. The GROMACS 4.5.5 software package[89] was used for all simulations. The isobaric isothermal NPT ensemble with periodic boundary conditions and a leap-frog Verlet integrator were used for all simulations. Pressure was set to 1 bar with the Berendsen barostat using a 2 ps time constant and temperature to 300 K with the Berendsen thermostat using a 0.1 ps time constant. Particle-Mesh Ewald summation was used for long-

Table 3.2: Physicochemical properties of the simulated pure solvent systems are given with available experimental data[102].

	Density <i>kg/m³</i>		Dipole <i>debye</i>		ΔH_{vap} <i>kJ/mol</i>	
	sim.	exp.	sim.	exp.	sim.	exp.
n-Dodecane	741	745			62.0	61.4
n-Decane	718	730			53.3	51.5
n-Octane	686	703			41.5	41.9
n-Hexane	635	655			30.6	31.5
4-Propyl Heptane	724	733			53.2	48.5
Diethyl Ether	711	713	1.37	1.15	27.7	27.3
Ethyl Propyl Ether	733	739	1.56		34.8	31.4
Toluene	839	867	0.33	0.36	36.5	38.8
Benzene	851	876			29.5	33.9
Isopropanol	793	786	2.08	1.66	45.6	45.7

range electrostatic summation with a 15 Å cut-off for short range electrostatic and van der Waals interactions. The LINCS algorithm was used for constraining hydrogen-containing bonds to enable a 2 fs time step. Each system was simulated for 70 ns from an initially unmixed configuration. Of the 70 ns run time, the first 20 ns were used for equilibration and the final 50 ns for sampling.

3.4 Results

3.4.1 Volume Change on Mixing

The volume change on mixing of the extractant and solvent molecules is investigated here as a measure of the molecular packing in the mixture compared to the pure phases. In addition to testing force field behavior, this metric gives insight into extractant-solvent interactions. Volume change on mixing has also been used as a measure of force field accuracy for TBP in *n*-dodecane[53]. Here, we compare the TBP and *n*-dodecane models used in this study to experimental values of volume change on mixing as well as two literature models[53, 56]. Mixing volume data is also given for the remaining extractants and solvent

Table 3.3: The number of molecules of each type for simulations of a given extractant volume fraction.

	0%	5%	10%	30%	50%	70%	90%	100%
TBP		28	56	166	278	388	500	500
TAP		24	46	138	232	324	416	416
DBBP		28	56	170	284	398	512	512
DAAP		24	48	142	236	330	424	424
n-Dodecane	626	626	592	460	328	198	66	
n-Decane	720	720	682	530	378	228	76	
n-Octane	848	848	804	626	446	268	90	
n-Hexane	1080	1080	1022	796	568	340	114	
4-Propyl Heptane	720	720	682	530	378	228	76	
Diethyl Ether	960	1398	1324	1030	736	442	148	
Ethyl Propyl Ether	1288				644			
Toluene	960	1320	1250	972	694	416	138	
Benzene	1688				844			
Isopropanol	1000	1826	1730	1346	962	576	192	

combinations. The percent volume change on mixing, $\% \Delta V_{\text{mix}}$, is calculated as the percent difference between an ideally mixing system and the actual resulting volume observed in simulation, given in as

$$\% \Delta V_{\text{mix}} = \frac{V_{\text{mix}} - (N_{\text{mol,extr}} V_{\text{mol,extr}} + N_{\text{solv}} V_{\text{solv}})}{V_{\text{mix}}} \times 100 \quad (3.4)$$

where N_{extr} and N_{solv} are the number of extractant and solvent molecules, respectively, in the mixed system. The pure phase volumes per molecule are $V_{\text{mol,extr}}$ and $V_{\text{mol,solv}}$ for the extractant and solvent, and V_{mix} is the volume of the mixed phase.

Figure 3.4 shows the TBP/dodecane percent volume change on mixing across a range of TBP volume fractions for the optimized GAFF TBP model developed for this study along with two literature AMBER TBP models[53] and corresponding experimental data[90, 103]. The two AMBER literature models, denoted in that study as DFT and MNDO signifying their atomic charge calculation methods, were simulated with the OPLS force field for dodecane. All three TBP models predict the same experimentally observed positive volume change on mixing trend across the volume fraction range, which indicates looser packing

in the mixture compared to the pure phases. The GAFF model presented here accurately replicates the percent volume change on mixing for the low TBP concentrations, including the range most relevant to the PUREX process at 30%, and corresponding to the highest percent volume change on mixing. At high TBP volume fractions, the optimized GAFF model underpredicts the experimentally observed decrease in the percent volume change on mixing following a maximum at 50% TBP. The AMBER TBP models also reproduce the general shape of the curve, although with more noise in the profile leading to ambiguity in the peak percent volume change on mixing. Particularly for TBP volume fractions below 50%, the optimized GAFF model shows improvement over existing literature models for volume change on mixing in *n*-dodecane.

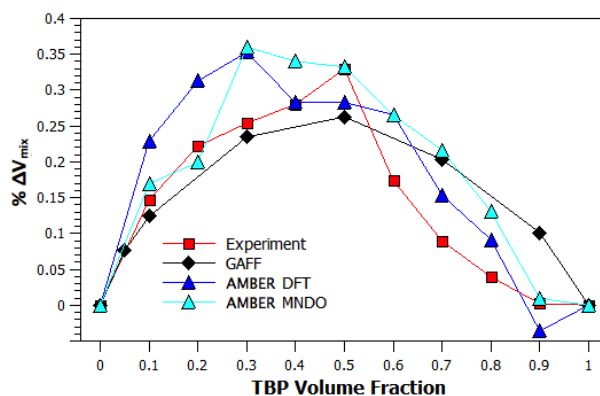


Figure 3.4: The percent volume change on mixing for the TBP/dodecane mixture is shown for the TBP model used here, along with the two AMBER models[53] and experimental values[90].

The percent volume change on mixing for the remaining extractants and solvents are given in Figure 3.5. The most significant increase in volume for each extractant was upon mixing with isopropanol, particularly for higher extractant volume fractions. The alkane solvents followed the same trend for each extractant with lower chain length corresponding to better mixing, i.e., lower $\% \Delta V_{\text{mix}}$, with *n*-hexane giving a negative percent volume change on mixing. The branched alkane 4-propyl heptane mixed better than *n*-decane, which has the same number of carbon atoms, but less well than *n*-octane. Both toluene and diethyl

ether gave a negative percent volume change on mixing.

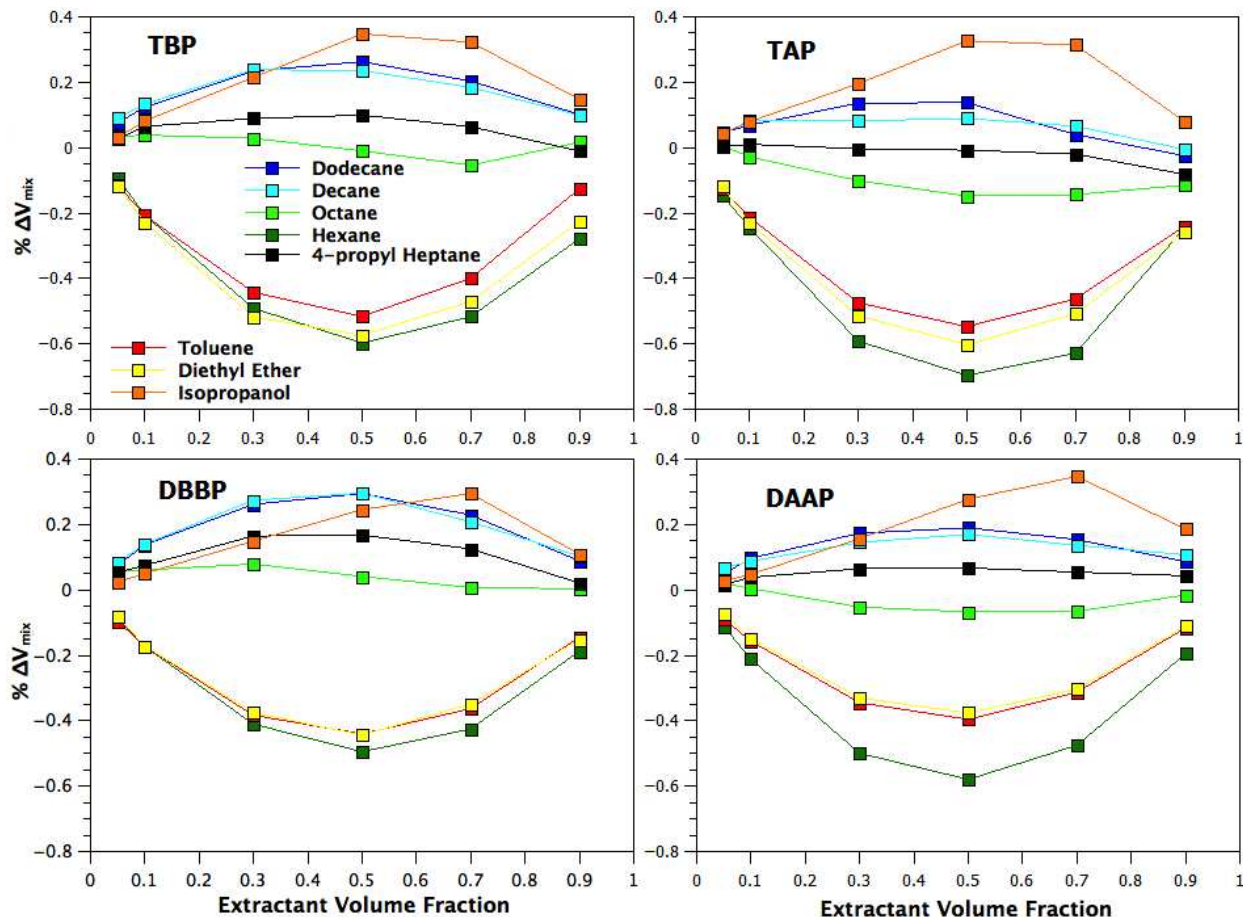


Figure 3.5: The percent volume change on mixing for each binary system is plotted across the range of extractant volume fractions for each extractant.

3.4.2 Enthalpy of Mixing

The enthalpy of mixing is defined as

$$\Delta H_{\text{mix}} = U_{\text{mix}} - (N_{\text{extr}}U_{\text{mol,ext}} + N_{\text{solv}}U_{\text{mol,solv}}) + p(V_{\text{mix}} - (N_{\text{solv}}V_{\text{solv}} + N_{\text{extr}}V_{\text{extr}})) \quad (3.5)$$

where U_{mix} is the energy of the mixed system, $U_{\text{mol,extr}}$ or $U_{\text{mol,solv}}$ are the per molecule energy of the pure extractant or solvent phases. It measures how enthalpically favorable a mixed extractant/solvent solution is compared to the pure components. In addition to accounting for the change in distance-dependent intermolecular forces as a result of changes in molecular

packing, the enthalpy of mixing is also impacted by other contributors to internal energy such as formation or disruption of polar interactions between extractant and solvent molecules. This property captures extractant-solvent interactions that determine mutual solubility of extractant and solvent.

There is experimental data for the enthalpy of mixing for TBP across a range of volume fractions in three of the solvents considered in this study: *n*-dodecane, *n*-hexane and benzene. The enthalpy of mixing for TBP in *n*-dodecane has also been investigated by simulation for a TBP model using the default OPLS parameters with and without refinement to the partial atomic charges[56]. Figure 3.6 shows the enthalpy of mixing values for the TBP model presented here compared to experimental data in *n*-dodecane and *n*-hexane to the OPLS simulation data for the *n*-dodecane system. The simulation results for the modified GAFF model, for both *n*-dodecane and *n*-hexane systems, match the experimental data exceptionally well across the entire range of TBP volume fractions. The default OPLS and refined OPLS models from the literature capture the trend in mixing enthalpy, although the specific values are not as accurate as the modified GAFF model. Accurately replicating the enthalpy of mixing curve lends confidence to the models used here to describe extractant-solvent interactions and for future studies that employ these models to investigate organic phase systems where extractant self-association and solvent-dependent solubility are relevant.

The enthalpy of mixing data for the each binary system simulated in this study are plotted in Figure 3.7. The enthalpy of mixing for the alkane solvents decreases with linear alkyl chain length with the 4-propyl heptane lying between *n*-decane and *n*-octane. Diethyl ether shows almost no change in enthalpy on mixing across the range of volume fractions. Toluene shows favorable mixing at all volume fractions. Isopropanol, due to hydrogen bond formation with the extractant phosphoryl oxygen, gives the most favorable enthalpy of mixing.

3.4.3 Extractant Self-Association

Numerous experimental[104] and simulation[56–58, 98] studies have shown that TBP molecules interact primarily through a “head-to-head” anti-parallel alignment of the dipoles

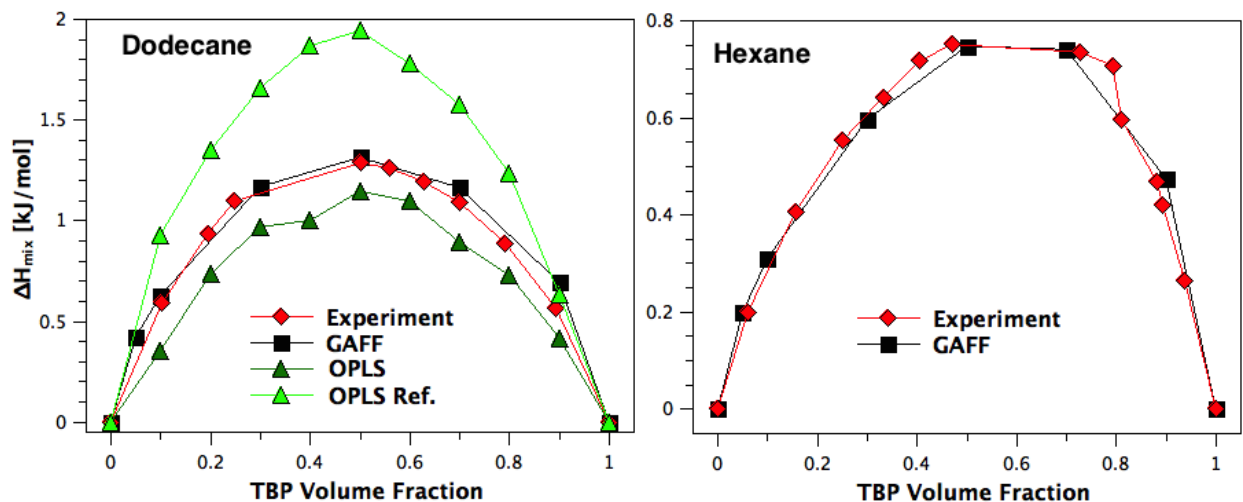


Figure 3.6: The enthalpy of mixing for the TBP/dodecane (left panel) and TBP/hexane (right panel) binary mixtures are plotted versus extractant volume fraction. Experimental data[103] is plotted in red diamonds, the modified GAFF TBP developed here with optimized GAFF *n*-dodecane is plotted with black squares. The OPLS and refined OPLS simulation data[56] are plotted with dark and light green triangles, respectively, for the *n*-dodecane systems only.

that point along the P=O bond. We have previously investigated TBP self-association, both in the form of dimerization and higher order association[98]. Good agreement was observed between the dimerization constant measured for the GAFF TBP model and the experimental value determined through IR spectroscopy. Other literature AMBER models with phosphoryl group charge scaling[50] were found to significantly underpredict the strength of TBP self-association. For the set of extractants and solvents studied here, we are interested in trends in association behavior resulting from both changing extractant structure, where the dipole magnitude and the length of the nonpolar alkyl tails of the extractant is varied, and solvent structure, where molecular packing and degrees of polarity that may disrupt inter-extractant interactions are expected to affect extractant self-association.

We previously established a criterion for extractant association[98] based on the distance and inter-dipole angle probability distribution for TBP and DAAP, wherein two molecules are considered associated if the phosphoryl oxygens are within 5.5 Å of each other. To quantify the extractant self-association, we consider the formation equilibrium constant

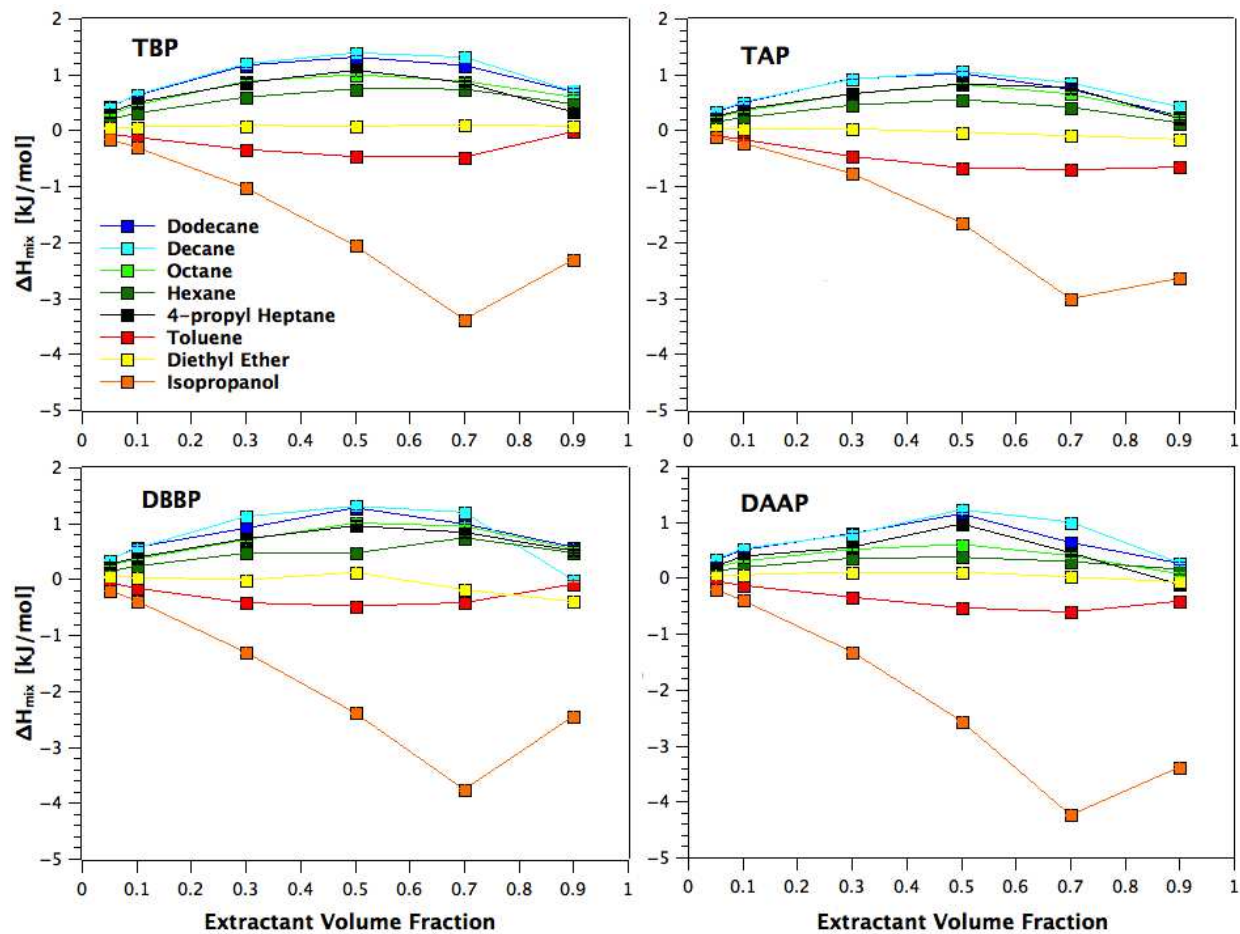


Figure 3.7: The enthalpy of mixing for each binary system is plotted versus volume fraction for each extractant.

$$k = e^{-M(\mu_M^0 - \mu_1^0)/k_B T} \quad (3.6)$$

for the equilibrium reaction



where X_M denotes a cluster of M extractants, X . The per molecule association free energies are defined as μ_M^0 and μ_1^0 for an M -mer and monomer, respectively, and $k_B T$ is the Boltzmann constant times the temperature[105]. Therefore, an exponential distribution of aggregate sizes correspond to a constant average association free energy over the range of that distribution. Deviation from the exponential distribution would indicate M -mers that are more or less energetically favorable per monomer than average across aggregation sizes.

Figure 3.8 plots the log of the number density versus aggregate size for the 30% extractant systems. Each panel corresponding to each of the four extractant molecules. The 30% extractant volume fraction is plotted here because it is the most applicable volume fraction to PUREX-type extraction systems. In determining the association free energy from the slopes of these plots, particularly for the long chain alkanes, a notable difference in association free energy is observed between dimer formation (given by the slope between aggregate sizes 1 and 2) and the remaining aggregate sizes. Therefore, we report the slope values for the dimer association separately from the average association energy of the remaining aggregate sizes. These values are given in Table 3.4 for each extractant and diluent combination in the 30% systems. Uncertainties are reported for the linear fitting of the μ values.

On average, the aliphatic diluents show a larger difference between the association free energy for dimers and for the remaining higher order aggregates than seen for other solvents. Toluene and diethyl ether show steeper slopes over the whole aggregate size range than the alkanes, indicating a more positive, less favorable association free energy. The association for isopropanol is even more limited, with less than 3% of extractants dimerized or otherwise associated with another extractant. For all of the alkanes, the dimer association energy trend between extractants was consistently TBP < DAAP < TAP < DBBP, where lower values

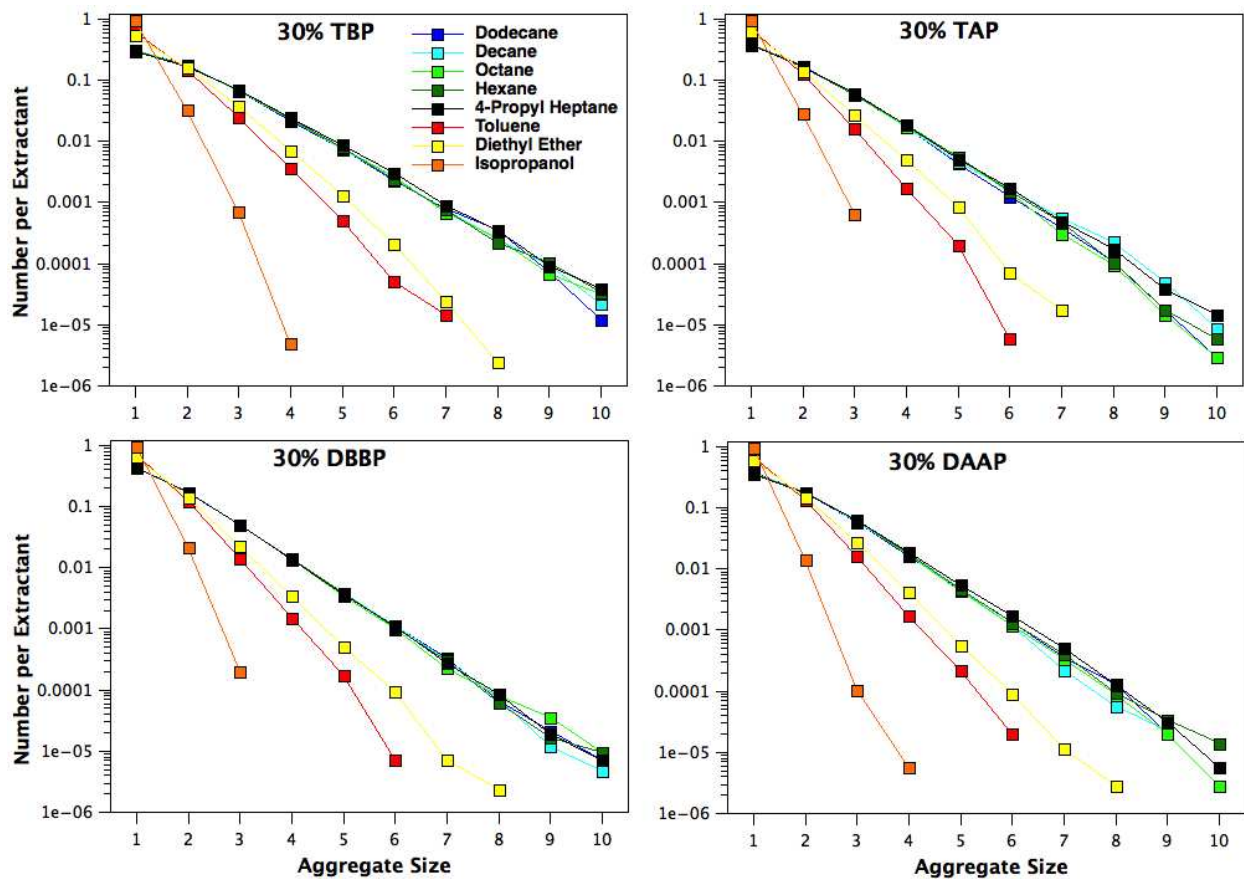


Figure 3.8: The distribution of aggregate sizes for the 30% extractant systems are plotted on a semilog scale for each solvent and extractant combination.

Table 3.4: The association free energies for extractant dimer formation and higher order associations are given below for each extractant and diluent combination for the 30% extracting volume simulations.

	association free energy, μ $k_B T$	TBP	TAP	DBBP	DAAP
n-Dodecane	dimer	0.56	0.83	0.95	0.76
	trimer+	1.15 ± 0.04	1.35 ± 0.04	1.28 ± 0.09	1.27 ± 0.03
n-Decane	dimer	0.60	0.86	0.94	0.72
	trimer+	1.12 ± 0.02	1.19 ± 0.03	1.33 ± 0.02	1.33 ± 0.03
n-Octane	dimer	0.62	0.85	0.94	0.71
	trimer+	1.11 ± 0.02	1.37 ± 0.04	1.23 ± 0.03	1.36 ± 0.03
n-Hexane	dimer	0.56	0.86	0.91	0.70
	trimer+	1.09 ± 0.02	1.30 ± 0.03	1.28 ± 0.03	1.22 ± 0.02
4-Propyl Heptane	dimer	0.57	0.82	0.93	0.72
	trimer+	1.07 ± 0.01	1.19 ± 0.01	1.28 ± 0.01	1.27 ± 0.03
Toluene	dimer	1.43	1.72	1.76	1.63
	trimer+	1.86 ± 0.05	2.4 ± 0.2	2.4 ± 0.1	2.19 ± 0.03
Diethyl Ether	dimer	1.21	1.46	1.55	1.39
	trimer+	1.84 ± 0.07	1.85 ± 0.06	1.88 ± 0.05	1.86 ± 0.03
Isopropanol	dimer	3.38	3.52	3.82	4.25
	trimer+	4.4 ± 0.3	3.8	4.6	3.9 ± 0.6

indicate more association.

3.5 Discussion

3.5.1 Isopropanol

Isopropanol most effectively reduced extractant association among the solvents studied, as evidenced by the highest association free energy for each extractant. The prevalent and readily observable hydrogen bonding of the isopropanol alcohol hydrogen with the phosphoryl oxygen of the extractant effectively prevents the preferred head-to-head orientation[104] that is favored by extractant self-association. Among the extractant types, however, the effects of isopropanol hydrogen bonding are not uniform. Figure 3.9 replots the percent volume change on mixing and the change in enthalpy on mixing for the four binary extractant/isopropanol systems.

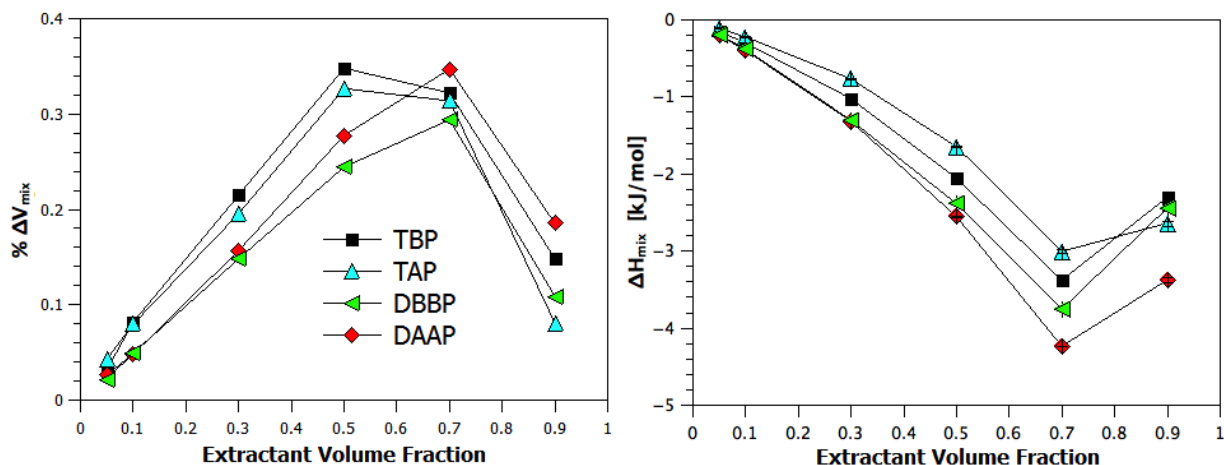


Figure 3.9: Volume change on mixing and enthalpy of mixing data for the four extractants in isopropanol are replotted here for comparison between those solvent and extractant types.

The four extractants have a minimum mixing enthalpy at 0.7 extractant volume fraction, corresponding to the volume fraction closest to a 1:1 extractant to solvent molar ratio where the maximum possible number of 1:1 extractant:isopropanol species exists. The change in

enthalpy resulting from hydrogen bond formation is not highest for TBP and DBBP, which have the smaller molecular volumes, compared to TAP and DAAP, even though there are more total extractant molecules and therefore more possible hydrogen bonds. (Note that the number of isopropanol molecules at the 0.7 extractant volume fraction is in excess of the number of extractant molecules for all extractant types.) Rather, the phosphonate extractants show the most enthalpically favorable mixing, implying stronger hydrogen bonds with their more electronegative phosphoryl oxygens. The radial distribution function (RDF) for the extractant phosphoryl oxygen to the OH hydrogen of the isopropanol is plotted in Figure 3.10 for the 50% and 70% extractant volume fractions. The DAAP RDF shows a higher peak at 0.17 nm corresponding to hydrogen bonding, while the other three extractants have similar hydrogen bonding peak heights. The second peak at around 0.4 nm corresponds to isopropanol hydrogen bonded to the isopropanol directly hydrogen bonded to the extractant. These peaks are more prevalent with more isopropanol in excess of extractant where more isopropanol-isopropanol hydrogen bonds are possible.

These data imply a complicated relationship between hydrogen bonding, mixing enthalpy and volume change on mixing. If the poorly packing 1:1 species is responsible for the large positive percent volume change on mixing and the favorable mixing enthalpy, one would expect DAAP to have the most positive and most negative values, respectively, for those properties. The order of the extractants between these properties is not in fact preserved. Therefore, the volume change is not simply proportional to the number of 1:1 species. The interpretation of the volume change is further complicated by the different extractant volume fractions for the maximum volume change on mixing. The phosphate extractants peak at 50% while the phosphonates peak at 70%, implying the peak percent volume change on mixing extractant volume fraction is not a function of extractant size (and therefore mole fraction) but rather depends on the difference in hydrogen bonding strength of the phosphoryl oxygen between phosphate and phosphonate groups as well.

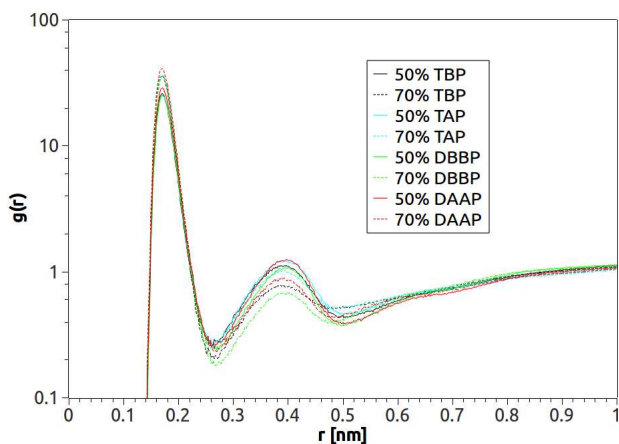


Figure 3.10: The radial distribution for the isopropanol alcohol hydrogen and the extractant phosphoryl oxygen, which form the extractant-solvent hydrogen bond, is plotted for the four extractants for the 50% and 70% extractant volume fraction systems.

3.5.2 Alkyl Wetting

The term wetting has been used[4] to describe the compatible contact between alkyl tails of the extractant with the solvent for metal-containing systems where the metal-centered extracted complexes are described as forming a “reverse micelle” with the extractant carbon tails directed outward into the solvent. In the literature, improved wetting, where the solvent-extractant alkyl groups more effectively overlap, is correlated to better solubility of the extracted complex and therefore a higher LOC. For the case of the binary mixtures considered here, even without metal ions present, the concept of wetting can still describe alkane solvent interaction with the alkyl tails of the extractant molecules.

The percent volume change on mixing is used to interpret how the different length aliphatic solvents and extractant alkyl tails affect packing efficiency. The differences in the enthalpy of mixing then measure how this impacts the energetics of the mixture for the different solvent chain lengths. This data is replotted in Figure 3.11 to compare extractants for *n*-dodecane and *n*-hexane. The mixing enthalpies for each extractant in the alkane solvents are uniformly unfavorable across the alkane series, with the unfavorability decreasing with decreasing alkane chain length (only *n*-hexane and *n*-dodecane shown).

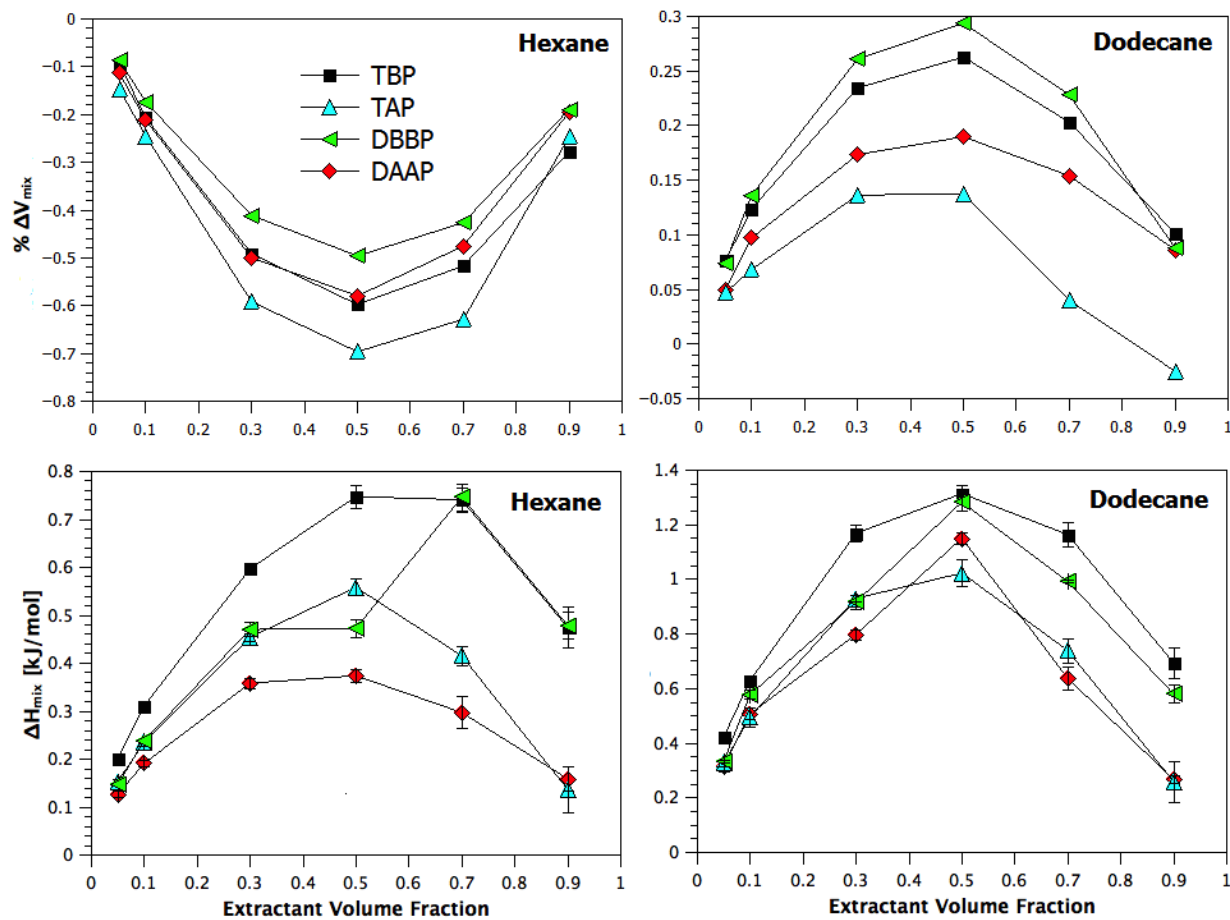


Figure 3.11: Percent volume change on mixing and enthalpy of mixing for the four extractants in *n*-dodecane and *n*-hexane are replotted here for comparison between solvent and extractant types.

TBP and DBBP have smaller molecular volumes than TAP and DAAP, and TBP and TAP have larger average molecular dipoles than DBBP and DAAP. Between the two extractant chain lengths, the change in enthalpy and volume on mixing is decreased with amyl, compared to butyl, tails across the alkane solvent series. This could indicate that, in general, more similarly sized extractant and solvent chain lengths result in more efficient molecular packing. The closer packing of the shorter *n*-hexane solvent in the mixed phase with the extractant reduces the average distance between atom sites and therefore strengthens the van der Waals interactions, making the mixture more enthalpically favorable. However, while the alkane solvent chain length affects the sign of the volume change on mixing, the enthalpy of mixing does not indicating it is dominated by another energetic contribution that is discussed in the following section.

3.5.3 Solvent Dilution of Extractant Dipole Interactions

If the enthalpy of mixing were primarily a function of packing, the sign change between *n*-dodecane and *n*-hexane for the mixing volume would be expected for the mixing enthalpy as well. The mixing enthalpy does become less positive, showing the impact of the improved packing, but it is apparent that it is not the only factor contributing to the mixing enthalpy. As the association energies of the extractants discussed previously do not change dramatically between alkanes, the contributions of the polar interactions between the solvent and extractant to the mixing enthalpy can be identified. Disruption of the polar extractant association through dilution of the extractant in the mixed phase, rather than enhanced van der Waals attraction from more effectively overlapped alkyl chains, dominates the mixing enthalpy. This is evidenced by the dipole association-driven enthalpy of mixing for the higher dipole phosphate extractants being more unfavorable than the phosphonate extractants with comparatively lower dipoles for the same carbon tail length.

3.5.4 Diethyl Ether and Extractant-Solvent Polar Interaction

To investigate the impact of solvent polarity, diethyl ether is compared to *n*-hexane as a linear molecule of similar length with the ether oxygen providing a molecular dipole moment. With diethyl ether, the volume change on mixing for each extractant was negative and similar in magnitude to *n*-hexane while the mixing enthalpy is close to zero and without a pronounced trend across volume fraction. For reference, these properties for diethyl ether are replotted in Figure 3.12 to compare between extractants. As was illustrated in Figure 3.11, for the alkane solvents, longer carbon tail groups resulted in lower volume changes on mixing. However, for diethyl ether the phosphate extractants has a significantly more negative percent volume change on mixing irrespective of alkyl tail length due to their increased dipole moment relative to phosphonate extractants resulting in more close dipole associations with the solvent. The error in the enthalpy of mixing for the diethyl ether simulations is large relative to the absolute values, leading to noise in apparent trends across the volume fractions in addition to the error captured in the block averaging.

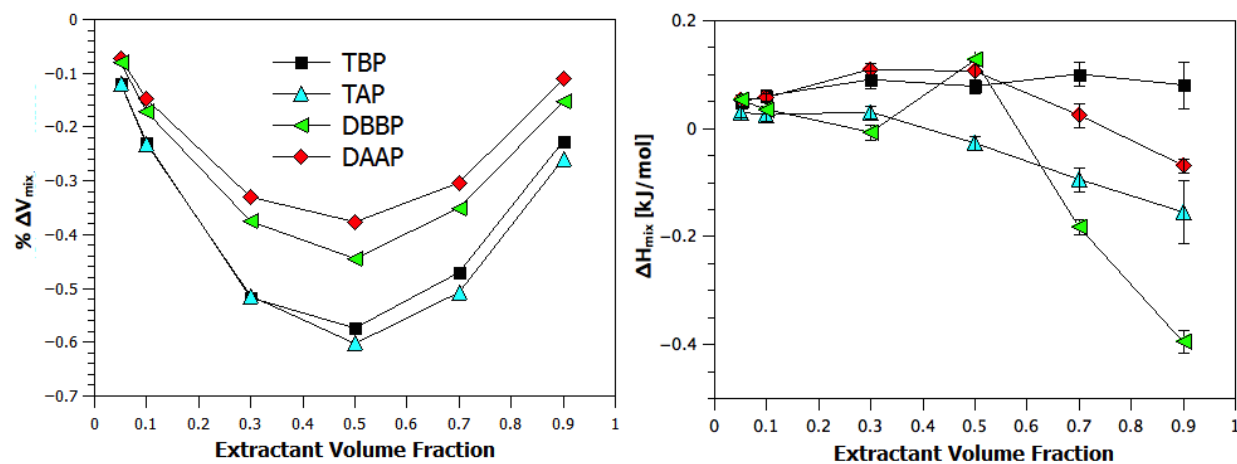


Figure 3.12: Volume change on mixing and enthalpy of mixing data for the four extractants in diethyl ether are replotted here for comparison between solvent and extractant types.

Table 3.4 shows a significantly more positive association free energy in the diethyl ether systems as compared to the alkane series. The polar interaction of the extractants with the

diethyl ether reduce the relative favorability of extractant-extractant association. The mixing enthalpy difference, averaged across the extractants for the 30% extractant system, between *n*-hexane and diethyl ether is 0.414 kJ/mol compared to a difference between *n*-hexane and *n*-dodecane of -0.483 kJ/mol. The impact of the ether oxygen on mixing enthalpy is thus similar to the impact of changing alkane chain length from *n*-dodecane to *n*-hexane. This may therefore be the case for other properties dependent on solvent-extractant interaction, possibly including extracted metal complex solubility: the thorium LOC in *n*-dodecane and *n*-hexane differ by a factor of 1.85[31].

To understand the packing differences that lead to the observed volume change on mixing trend, the extractant-diethyl ether RDFs are considered. Figure 3.13 show the extractant phosphoryl oxygen to solvent ether oxygen radial distribution function for the 50% extractant system for each extractant. The first peak, located near 0.45 nm, is higher for the phosphate extractants. The first peak corresponds to coordination of the solvent molecule near the extractant head group. The phosphate extractants, with larger molecular dipoles than the phosphonates, are more likely to be found in this orientation. This is in contrast to the isopropanol systems where solvent-extractant hydrogen bonding is governed by phosphoryl oxygen partial charge, which is stronger for the phosphonate groups compared to phosphate. The diethyl ether-extractant oxygen to oxygen RDFs also show a different grouping for the peak near 1 nm, where the butyl tail extractants have the peak at a closer radial distance than the amyl tail extractants. The dependence of alkyl tail length indicates that this second peak corresponds to the diethyl ether dipole aligned with the extractant dipole, positioned behind the carbon tails of the extractant.

Ethyl propyl ether was also simulated for the 50% TBP system as another comparison to *n*-hexane, as its length is closer to *n*-hexane than diethyl ether's. The percent volume change on mixing for ethyl propyl ether was -0.36 for the 50% TBP system, less negative than the value of -0.57 for diethyl ether and -0.60 for *n*-hexane. The reduction in linear length from ethyl propyl ether to diethyl ether improved packing with TBP to a similar

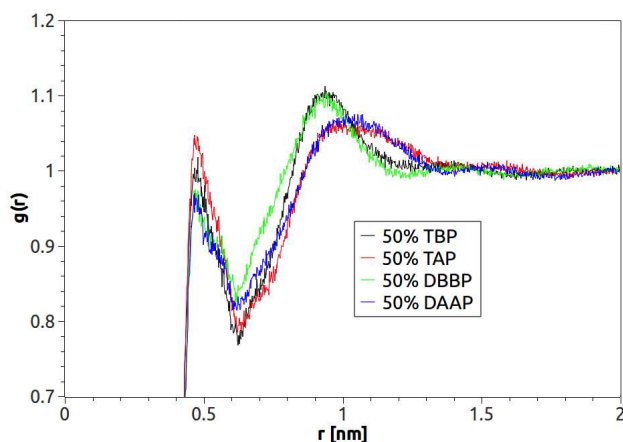


Figure 3.13: The radial distribution for the ether oxygen in diethyl ether and the extractant phosphoryl oxygen is plotted for the four extractants for the 50% extractant volume fraction systems.

degree as replacing the bridging oxygen with another carbon site. The mixing enthalpy for ethyl propyl ether is 0.07 kJ/mol, compared to 0.08 kJ/mol for diethyl ether in the same 50% TBP system. This indicates that, as with the alkane solvent systems, the ether oxygen and the related polar interactions are more responsible for the magnitude of the mixing enthalpy than the change in molecular packing resulting from increasing the linear molecular length.

3.5.5 Comparing *n*-Hexane, Diethyl Ether and Toluene

As shown in Figure 3.5, toluene has a similar volume change on mixing profile across volume fractions as diethyl ether and *n*-hexane for each extractant. Unlike diethyl ether and *n*-hexane, however, the enthalpy of mixing for toluene is uniformly favorable, as shown in Figure 3.7. These data for toluene with the four extractants are replotted together in Figure 3.14. Extractant association is weaker in toluene than diethyl ether, which is weaker than hexane. The enthalpically favorable mixing in toluene is thus in spite of reduced extractant-extractant polar association. The favorable mixing enthalpy of TBP with another very similar aromatic solvent, benzene, has been attributed to extractant polarization of the aromatic π electrons of the solvent[103]. However, the force fields used here do not include polarization. Therefore, if polarization were the primary factor in the mixing enthalpy,

we would expect a significantly less negative value in simulation as compared to experiment. As there is no experimental data for the toluene/extractant system, we compared simulation results of the TBP/benzene system to experiment. The 50% TBP/benzene simulation gives $\Delta H_{mix} = -0.233$ kJ/mol while the experimental value for 49.9% TBP gives -0.257 kJ/mol. This close agreement suggests that the mixing enthalpy is largely captured in these simulations and not, therefore, primarily a result of the polarizability.

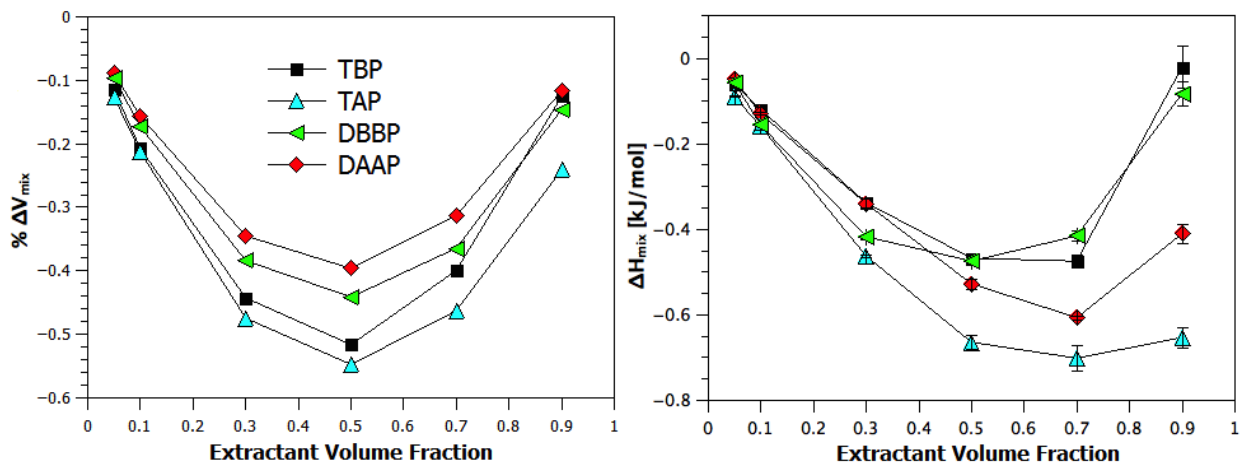


Figure 3.14: Percent volume change on mixing and enthalpy of mixing data for the four extractants in toluene are replotted here for comparison between solvent and extractant types.

Toluene and benzene show a surprisingly high mixing enthalpy with the extractants studied despite the negative mixing volume and lack of strong polar association with the extractants. As compared to benzene, toluene gives an even more favorable mixing enthalpy with a value of -0.468 kJ/mol for the 50% TBP system. The percent volume change on mixing is similarly lower in magnitude for benzene, with a value of -0.388 compared to -0.516 for toluene in the 50% TBP system. In addition to the extractant-solvent polar interactions present with toluene, given by the 0.33 D dipole moment of toluene, the closer packing in the extractant/toluene system further improves the mixing enthalpy compared to benzene. Investigation of the carbon-carbon RDFs, plotted in Figure 3.15 for the extractant and solvent molecules in the TBP/toluene and TBP/benzene systems does not indicate that

the difference between those solvents is a result of behavior for a specific extractant-solvent orientation. Rather, the carbon-carbon distances across the range of radial distances are uniformly higher for the 50% TBP simulations, including for most observed peaks. The more negative mixing enthalpy for toluene compared to benzene is therefore likely a result of closer packing across many molecular orientations rather than a specific single orientation as might be expected if toluene-extractant dipole alignment was responsible for more favorable mixing with toluene compared to benzene.

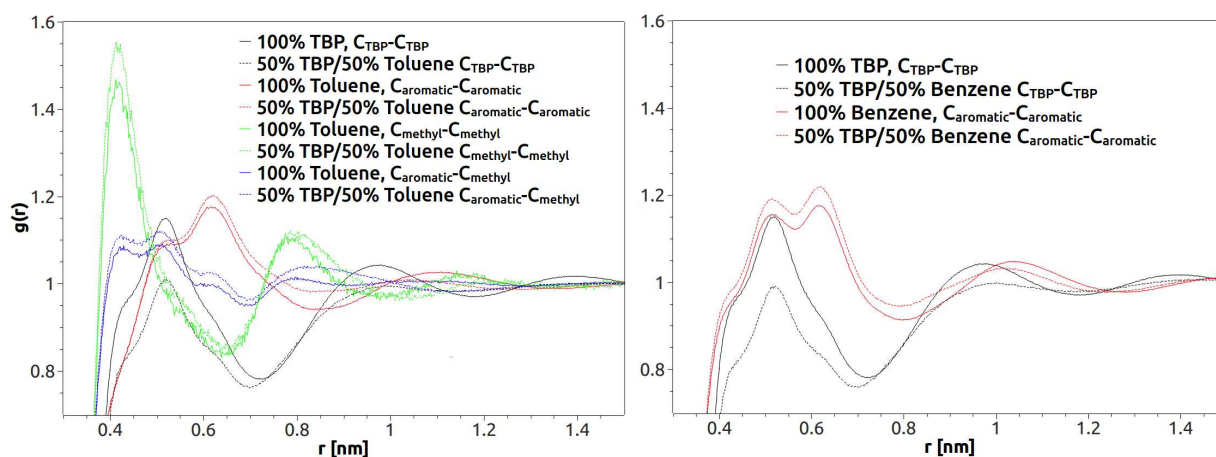


Figure 3.15: The aromatic and aliphatic carbon-carbon radial distribution functions for the pure TBP, toluene and benzene systems as well as the 50% TBP with toluene and benzene systems are plotted.

The questions remains: if polar solvent-extractant interactions are not present or dominant for *n*-hexane, toluene or benzene, and the percent volume change on mixing is similar, why is the mixing enthalpy for TBP in toluene and benzene significantly more favorable than *n*-hexane? The difference in mixing enthalpy between *n*-hexane and toluene is 1.215 kJ/mol for the 50% mixture with TBP. The contributions to the potential energy of those two mixtures are considered here. In toluene, the contributions to the change in potential energy upon mixing from the short range Coulombic repulsion and long range Coulombic attraction nearly cancel each other out, with a net change for the mixture of 0.066 kJ/mol. However, this is not the case for *n*-hexane, where the net change in Coulombic potential

for the mixture results in a 0.593 kJ/mol. This difference can be attributed to the lower dielectric constant of *n*-hexane of 1.89 compared to 2.30[106] for toluene. Roughly half of the difference in mixing enthalpy between *n*-hexane and toluene is accounted for in this way. Of the remaining 0.688 kJ/mol of the difference between toluene and *n*-hexane in mixing enthalpy, 0.294 kJ/mol results from lower net Lennard-Jones potential energy for toluene. Therefore, we find that the difference in dielectric constants between the nonpolar organic solvents, while small compared to the dielectric constant of polar solvents such as water, is the primary factor in the difference in energetics of the mixed solutions. However, the dielectric constant for diethyl ether is higher than toluene, so this explanation does not also resolve the difference between toluene and diethyl ether.

The extractant volume fraction with the minimum mixing enthalpy is higher for the amyl and butyl extractants. This is attributed to the difference in extractant mole fractions for a given volume fraction, where the minimum corresponds to a given mole fraction rather than volume fraction. The minimum mixing enthalpy corresponding to a particular extractant mole fraction indicates that a particular ratio of extractant to solvent achieves the most favorable mixing rather than a specific volume ratio between the two. This is observed with isopropanol due to hydrogen bonding, but not with the other solvents studied. The reason for this occurring for toluene is not obvious and is difficult to discern unless extractants with reasonably different mole per volume ratios are compared.

3.6 Conclusions

The mixing and association behavior of four neutral organophosphorus extractant molecules has been investigated over a range of volume fractions for organic solvent molecules differing in length, branching, dipole and chemical functionality. To carry out these studies, MD potentials for the extractants were first fit to a range of pure extractant phase bulk properties. Those models were then validated with binary TBP/solvent phase behavior, with excellent agreement with experiment found for percent volume change on mixing and mixing enthalpy. These models can be applied to future studies of organic phase phenomenon

such as third phase formation where capturing extractant-solvent interactions that govern extracted complex solubility and phase behavior is necessary.

Trends in extractant association, mixing volume and enthalpy of mixing were compared between extractants and solvents and explained in terms of specific molecular interactions. Alkane/extractant solutions resulted in a volume change on mixing highly dependent on alkane chain length, attributed to solvent-extractant alkyl chain packing compatibility, with positive values for *n*-dodecane and negative values for *n*-hexane. Although the mixing enthalpy was positive for all alkanes, decreasing solvent chain length was similarly correlated with decreasing enthalpy of mixing. Alkane chain branching had a similar effect to slightly reduced the effective chain length observed for those properties. Extractant hydrogen bonding to isopropanol led to a significantly increased percent volume change on mixing and gave the most enthalpically favorable solvent mixtures. Diethyl ether polar association with the extractant molecules, both near the phosphoryl oxygen “head” of the extractant molecule and with the carbon tail region, led to an increased mixing volume similar to the similarly sized *n*-hexane solvent, but with a small change in enthalpy on mixing. Interestingly, toluene mixtures exhibited a reduction in mixing volume similar to *n*-hexane and diethyl ether, but gave a favorable change in mixing enthalpy. Rather than resulting from polarization induced by the permanent TBP dipoles as proposed in the literature, this was attributed, in part, to the mixture’s more favorable long range Coulombic potential energy allowed by the relatively higher dielectric constant of toluene. The model development and analysis of the energetics of binary phase solutions presented here can be used to guide future investigation into solubility-dependent mixed organic phase solvent extraction systems.

CHAPTER 4
NETWORK ANALYSIS AND PERCOLATION TRANSITION IN HYDROGEN
BONDED CLUSTERS: NITRIC ACID AND WATER EXTRACTED BY TRIBUTYL
PHOSPHATE

Modified from a paper published in *Physical Chemistry and Chemical Physics*¹.

*Michael J. Servis*², *David T. Wu*³, *Jenifer C. Braley*⁴

4.1 Abstract

Extraction of polar molecules by amphiphilic species results in a complex variety of clusters whose topologies and energetics control phase behavior and efficiency of liquid-liquid separations. A computational approach including quantum mechanical vibrational frequency calculations and molecular dynamics simulation with intermolecular network theory is used to provide a robust assessment of extractant and polar solute association through hydrogen bonding in the tributyl phosphate (TBP)/HNO₃/H₂O/dodecane system for the first time. The distribution of local topologies of the TBP/HNO₃/H₂O hydrogen bonded clusters is shown to be consistent with an equilibrium binding model. Mixed TBP/HNO₃/H₂O clusters are predicted that have not been previously observable in experiment due to limitations in scattering and spectroscopic resolution. Vibrational frequency calculations are compared with experimental data to validate the experimentally observed TBP-HNO₃-HNO₃ Chain structure. At high nitric acid and water loading, large hydrogen-bonded clusters of 20 to 80 polar solutes formed. The cluster sizes were found to be exponentially distributed, consistent with a constant average solute association free energy in that size range. Due to the deficit

¹Adapted with permission from *Physical Chemistry and Chemical Physics* **2017** 19 (18). 11326-11339. Copyright 2017 Royal Society of Chemistry.

²Primary Author and Researcher

³Corresponding Author and Advisor

⁴Corresponding Author and Advisor

of hydrogen bond donors in the predominantly TBP/HNO₃ organic phase, increased water concentrations lower the association free energy and enable growth of larger cluster sizes. For sufficiently high water concentrations, changes in the cluster size distribution are found to be consistent with the formation of a percolating cluster rather than reverse micelles, as has been commonly assumed for the occurrence of an extractant-rich third phase in metal-free solvent extraction systems. Moreover, the compositions of the large clusters leading to percolation agrees with the 1:3 TBP:HNO₃ ratio reported in the experimental literature for TBP/HNO₃/H₂O third phases. More generally, the network analysis of cluster formation from atomic level interactions could allow for control of phase behavior in multi-component solutions of species with a variety of hydrogen bond types.

4.2 Introduction

Organic-aqueous solvent extraction systems are used in *f*-element (lanthanide and actinide) hydrometallurgical applications[79], wherein neutral, adduct-forming solvating extractants recover nitric acid (HNO₃) and water (H₂O), as well as the metal ion of interest. The co-extraction of HNO₃ and H₂O with the target metals is generally benign from a separations perspective, since both evaporate during formation of the *f*-element oxides preferred for transport or storage, but the hydrogen bonding networks that result from their presence could be responsible for the undesirable phenomenon of third phase formation. In third phase formation, the organic phase partitions into two phases: a light phase, primarily comprised of organic diluent, and a heavy phase, containing significant amounts of extractant and extracted polar solutes. This is thought to occur when the extracting ligand extracts sufficiently many polar solutes that the resulting aggregates grow large enough and polar enough to no longer be organic soluble. Third phase formation has been observed in a variety of extraction systems, occurring even without metal ions[97], depending on the extractant molecule(s), organic solvent, acid type and acid concentration[15–18, 97, 107]. Third phase formation is often problematic due to incompatibility of the separations equipment with three-phase based separations and, for nuclear fuel cycle applications, the unanticipated

concentration of plutonium that could lead to excess heating or a criticality incident.

The Plutonium Uranium Redox EXtraction (PUREX) process is, historically, the most studied solvent extraction system and is used to recover uranium and plutonium from used nuclear fuel. In PUREX, an organic phase, consisting of tributyl phosphate (TBP) in a kerosene diluent, is contacted with an aqueous phase containing used fuel dissolved in concentrated nitric acid[79]. The TBP selectively recovers hexavalent and tetravalent actinides from the aqueous phase, leaving behind trivalent fission products and transuranics. The extracted TBP-metal ion complexes include charge neutralizing nitrate anions and coextracted water. Even without the presence of metal ions in the aqueous phase, TBP extracts nitric acid and water from the aqueous phase. Third phase formation has been reported for the PUREX system for high nitric acid concentrations without metal ions[3], although the mechanism for this phase transition is not established. In PUREX systems, and other metallurgical separation processes, the aggregation of the extracted complexes influences extraction behavior[108] and third phase formation. Atomistic level understanding of the aggregation resulting from hydrogen bonding network formation in these systems could be used to identify third phase formation, understand interactions that encourage the phase transition and design extraction systems that avoid the onset of third phase formation.

Experimental interpretation of third phase formation with metal ions in the PUREX system has involved modeling extracted complexes in small angle scattering using the Baxter model of sticky hard spheres, a simplified analytic model made with the assumption that the clusters are reverse micelles containing a single metal ion[18]. However, recent diffusion NMR spectroscopy has shown that the Baxter model may not accurately capture inter-aggregate interactions[109]. While numerous PUREX experimental studies have evaluated metal ion extraction, including third phase formation[15–18], less emphasis has been placed on understanding water and nitric acid extraction in concentrated acid systems and the resulting aggregation behavior of non-metal containing systems. Moreover, given that acid type has been shown to impact third phase formation[21, 29, 97], and other extraction systems such as

TRansUranic EXtraction (TRUEX) readily form third phases without metals[97], studying interactions between acid, water and ligand without metal ions is expected to help understand the common attributes of third phase formation in the presence of metal as well. However, small angle x-ray scattering experiments have indicated that the hard sphere reverse micelle interpretation used to explain third phase formation in metal-containing PUREX systems is not applicable to the acid and water only systems[23]. For this and other acid-only extraction processes prone to third phase formation such as TRUEX[22], atomistic-level understanding of polar solute cluster formation could inform the choice of candidate form factors for corresponding small angle scattering experiments.

For extraction systems without metal, a possible mechanism for the third phase transition is the formation of an extended percolating cluster. Percolation has been used to describe gelation transitions resulting from physical or chemical interactions in self-assembling liquids[110–114] and polymer solutions[115, 116]. For multi-site, multi-component self-associating liquids, understanding the clustering behavior of these systems on a molecular level could enable control and prediction of the percolation threshold. Control of liquid-liquid phase transitions of heterogeneous systems also has direct relevance to temperature dependent solvent systems[117], where an initially homogenous solution is driven biphasic to facilitate separation.

Previous studies have addressed water and nitric acid extraction by TBP using experimental and theoretical techniques. Experimental approaches to this subject have included modeling extraction stoichiometries using aqueous phase activities but do not address organic phase equilibrium structures and speciation[118]. To better understand PUREX-type systems from a molecular level, and specifically the molecular interactions that drive aggregation, the organic phase structures of TBP/nitric acid/water complexes and the hydrogen bonded clusters they form are characterized here using molecular dynamics (MD), quantum mechanical calculations and infrared (IR) spectroscopy. MD simulation has been used to study TBP extraction of nitric acid and water in the literature[34–38]. These studies re-

ported snapshots of TBP coordination and, in a supercritical CO₂ diluent, measured the average number of each type of hydrogen bond between TBP, nitric acid and water. Measuring the average number of each hydrogen bond type, however, is not sufficient to describe the cluster sizes or topologies present, as different topologies will have the same numbers of constituent hydrogen bonds. Detailed topological information can describe how clusters are formed and how speciation under moderate acid conditions gives way to large cluster formation characteristic of a third phase system.

Knowledge of site-site hydrogen bonding interactions that connect polar solutes into clusters and the speciation of those clusters can allow interpretation and assignment of experimental characterization techniques, such as spectroscopy, as well as prediction of extraction efficiency and phase partitioning. An understanding of hydrogen bonding equilibrium could also allow for prediction of that behavior through factors influencing that binding equilibrium, including the available hydrogen bond donor and acceptor site pairs, the relative interaction strengths of those pairs and their concentrations. Using this framework, one could then account for variables known to impact speciation and phase behavior, such as molecule types and temperature.

A quantitative description of the clustering behavior in the organic phase, especially under high acid conditions where the topologies become increasingly complex, requires a more complete analysis. This means significantly longer simulation run times, on the order of 100 ns compared to the 1 to 5 ns of previous studies, are needed to adequately sample less frequently occurring topologies. The network analysis approach developed here to characterize solute connectivity resulting from hydrogen bonding allows for quantitative descriptions of local cluster topology and overall cluster metrics such as size distribution and composition for specific molecule site types. Experimental validation of local TBP coordination behavior is conducted by comparing the topology of the 1:2 TBP:HNO₃ complex to existing experimental IR spectroscopic data[28] and corresponding quantum mechanical (QM) frequency calculations performed for this study. Relative hydrogen bond strengths of the different

types of hydrogen bonds present in this system are determined using equilibrium binding constants fit to simulation data. The compositions and topologies of clusters are characterized by the occurrence of specific structures and substructures. Finally, the size distribution and composition of large clusters, observed at high nitric acid and water extraction where third phase formation has been observed in the experimental literature[3], are determined to identify a possible mechanism of cluster growth and third phase formation.

4.3 Methodology

4.3.1 Force Fields

Nitric acid and water extraction by TBP has been studied in MD simulation by Wipff and coworkers in chloroform[34–36, 38] and supercritical CO₂[37]. Those previous simulation studies observed significant hypercoordination of the TBP phosphoryl oxygen, *i.e.*, accepting multiple concurrent hydrogen bonds. This behavior is contradicted by IR spectroscopic evidence[28] and we suspect may result from the exaggerated molecular dipole of the TBP model used[50]. Thus, updated MD potentials, particularly for TBP, are needed.

The Generalized AMBER Force Field (GAFF)[32] flexible, all-atom parameters were used to model the TBP, *n*-dodecane and nitric acid molecules in this system. Several force fields, including AMBER[50–53, 74, 77, 83], CHARMM[46], OPLS[56] and GAFF[58, 59] have been used to model TBP in the literature. We previously reported a TBP model[98] with modified GAFF parameters and AM1-BCC calculated charges[85, 86] that accurately replicated experimental values of the dimerization constant[96] and electric dipole[91, 92, 96], expected to be relevant to organic phase aggregation behavior. This manuscript shows the recently developed TBP model[98] does not engage in hypercoordination. To avoid inadvertent introduction of unphysical behavior resulting from significant parameter adjustments, we optimized the phosphorus-containing dihedrals, which were not explicitly defined for the atom combinations in TBP and were thus possible sources of deviations from experimen-

tal values[98]. Previous literature models have addressed dipole matching via phosphoryl group charge scaling[50] or phosphoryl oxygen van der Waals parameter adjustments[58]. The OPLS model did not attempt to match the dipole moment[56], which is overpredicted by nearly a factor of two with the default OPLS parameters. The charge scaled AMBER models underpredict self-association[98].

The default GAFF parameters for the carbon atoms are known to be too strong, overpredicting the attraction in long chain alkanes resulting in an unphysical transition to a gel phase under ambient conditions[58, 98, 100]. Adjustment of those GAFF parameters to correct for over-attraction in fatty acids has been conducted before in the literature[119]. The optimized van der Waals parameters used by Vo *et al.*[59] for the carbon atoms in *n*-dodecane were implemented in this study to avoid the aforementioned gel phase transition.

In addition to previous changes in the dihedral potentials, we have since further optimized the van der Waals parameters for the carbon atoms on the butyl tails to improve agreement with the density and enthalpy of vaporization across the class of organophosphorus solvating extractants including diamyl amyl phosphonate, triamyl phosphate and dibutyl butyl phosphonate. This optimization process across the four extractants limited changes to the default parameters to <5%, to minimize changing property values that were previously calibrated. The resulting optimized TBP carbon atom van der Waals parameters are 3.2297 Å and 0.1127 *kcal/mol* for the σ and ϵ potential well position and depth terms, respectively, corresponding to scaling of the default values by 95% and 103%. Charges and force field parameters for TBP and *n*-dodecane, to clarify modifications from the default GAFF values, are provided in Appendix B.

Nitric acid charges were calculated using the same method as for TBP and *n*-dodecane[98] and are given in Figure 4.1. The nitric acid proton was assumed to be associated in the organic phase systems studied here. The protonation state of extracted nitric acid has been investigated in the literature using both experimental and computational techniques. IR spectroscopy[120] and conductivity measurements[121] have shown that extracted nitric

acid exists in the organic phase predominantly in the associated form. Molecular dynamics simulations of biphasic organic/aqueous systems with nitric acid have investigated the impact of modeling nitric acid as associated or dissociated on extraction by TBP into the organic phase. Those studies found that an associated nitric acid model is necessary to accurately capture nitric acid partitioning into the organic phase[35, 38, 43]. Therefore, as we are only simulating the post-contact organic phase, we model nitric acid in its associated form. Note the asymmetry in non-hydroxy oxygen charges, with the larger negative charge on the oxygen closer to the hydrogen atom. Water was modeled with the TIP4P force field as the hydrogen bonding behavior of this model compares favorably to alternative water potentials[122].

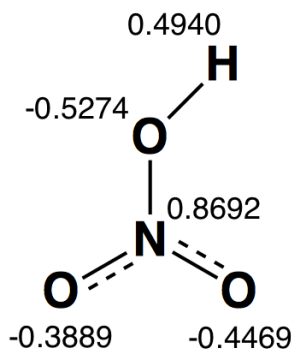


Figure 4.1: The AM1-BCC atomic charges used in the GAFF nitric acid model. Charges are given in fundamental units.

4.3.2 Simulation Systems and Conditions

The post-contact organic phase simulations presented here correspond to extraction of nitric acid and water by 20% TBP in *n*-dodecane from seven initial aqueous phase nitric acid concentrations, $[\text{HNO}_3]_{aq,i}$, ranging from 0 M to 16 M (corresponding to organic phase acid concentrations, $[\text{HNO}_3]_{org}$, between 0 and 1.25 M). The system compositions are given in Table 4.1. System compositions were taken from previously reported experimental data[118, 121, 123, 124]. At the highest acid concentrations, the extracted water concentration is not well established. Due to the lack of data and the inherent uncertainty of existing data, we simulate three different water concentrations, labeled A-C, for the 1.10 and 1.25 M $[\text{HNO}_3]_{org}$

systems. The A water concentration for the 1.10 M $[\text{HNO}_3]_{org}$ system corresponds to reported data. The amount that the water concentration increases between 1.10 and 1.25 M $[\text{HNO}_3]_{org}$ is not known, with possible higher values simulated in the B and C concentrations. To consider the impact of nitric acid concentrations, the B and C water concentrations were applied to the 1.10 M $[\text{HNO}_3]_{org}$ system as well.

Table 4.1: Numbers of molecules and their approximate concentrations for each simulation in this study. The systems correspond to a range of $[\text{HNO}_3]_{aq,i}$, with A-C in the 1.10 and 1.25 M systems indicating simulations run with a range of water concentrations.

$[\text{HNO}_3]_{aq,i}$ (M)	0	3	6	8	12	14			16		
						A	B	C	A	B	C
# H_2O	21	18	12	8	9	14	21	28	14	21	28
$[\text{H}_2\text{O}]$ (M)	0.21	0.20	0.13	0.09	0.10	0.15	0.23	0.31	0.15	0.23	0.31
# TBP	73	66	66	66	66	66			66		
$[\text{TBP}]$ (M)	0.73	0.73	0.73	0.73	0.73	0.73			0.73		
# HNO_3	0	37	61	67	86	99			113		
$[\text{HNO}_3]$ (M)	0.00	0.41	0.67	0.74	0.95	1.10			1.25		
# $\text{C}_{12}\text{H}_{26}$	350	350	305	305	302	299			296		

Molecular dynamics simulations were completed using the GROMACS 4.5.5 software package[89]. The isobaric isothermal NPT ensemble with periodic boundary conditions and a leap-frog Verlet integrator were used for all simulations. Pressure was set to 1 bar with the Berendsen barostat and temperature to 300 K with the Berendsen thermostat. Particle-Mesh Ewald summation was used for long-range electrostatic summation with a 15 Å cut-off for short range electrostatic and van der Waals interactions. The LINCS algorithm was used for constraining hydrogen-containing bonds to enable use of a 2 fs time step. Each system was run 10 times and values presented here are averages over those ten runs. Each run consisted of a 10 ns annealing time to randomize initial configurations. After annealing, the systems equilibrated for 5 ns followed by a 10 ns production run where coordinates were recorded for analysis every 20 ps. To obtain sufficiently good statistics for quantitative analysis of hydrogen bonding networks formed in these systems, 100 total ns of data were collected for each system.

4.3.3 Hydrogen Bonding Definitions

Figure 4.2 depicts the six hydrogen bond types possible between the three types of oxygen atoms (O_T , O_N and O_W) and the two types of hydrogen atoms (H_N and H_W). The subscripts designate the molecule type to which the atom belongs ($T = \text{TBP}$, $N = \text{HNO}_3$, $W = \text{H}_2\text{O}$). The bridging hydroxy oxygen of the nitric acid molecule was not observed to participate in significant hydrogen bonding. The O-H-O angle cut-off criterion used for hydrogen bond identification was 30 degrees. Increasing the angle cut-off to 45 degrees did not result in significantly different results. The distance cut-off was chosen to count only interactions within the first peak of the radial distribution function (RDF) of each atom combination, and was chosen separately for each hydrogen bond type. RDFs for each hydrogen bond type are given in Appendix B for one run of the 1.25 M system with water concentration A (1.25 M-A). The values for the distance cutoffs, given in Table 4.2, were used for all systems as they do not differ significantly between systems.

Table 4.2: The distance cutoffs applied for the different hydrogen bond types in all simulations are given here. An angle cutoff of 30 degrees was also used for each hydrogen bond type.

Hydrogen Bond	Distance Cutoff, Å
$O_T - H_N$	1.98
$O_T - H_W$	2.24
$O_N - H_N$	2.96
$O_N - H_W$	2.66
$O_W - H_N$	2.16
$O_W - H_W$	2.40

4.3.4 Network Analysis

Network analysis is used to analyze the hydrogen bond networks formed in the simulations presented here. In this network analysis, the configuration and hydrogen bonding of all the polar solutes are reduced to a system graph consisting of vertices and edges. Each solute

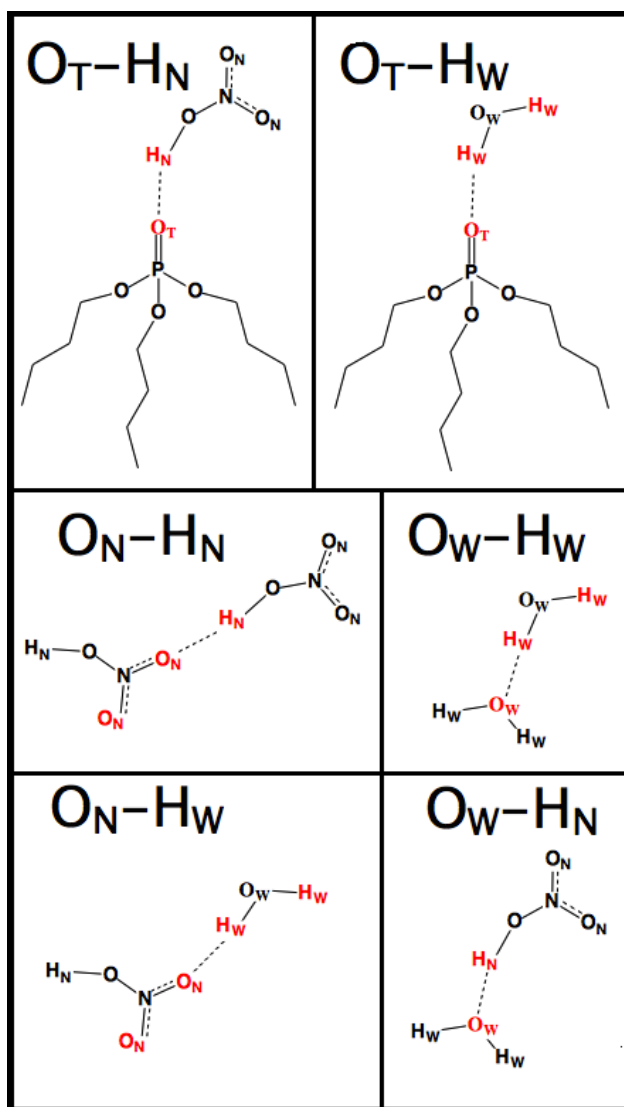


Figure 4.2: The six possible hydrogen bond types in the TBP- HNO_3 - H_2O extraction systems are depicted here with participating atoms highlighted for the given hydrogen bond type. The subscript in the atom name gives the molecule type to which the O or H atom belongs with T being TBP, N nitric acid and W water.

molecule is a vertex, and any two vertices are connected by an edge if there exists a hydrogen bond of any type between the corresponding molecules. Furthermore, a cluster is defined as a connected component subgraph of the entire system graph, i.e., a subgraph wherein any vertex in that subgraph is connected through some path to any other vertex in the subgraph, and no vertex in that subgraph is connected to a vertex outside of the cluster subgraph. Figure 4.3 shows a graph composed of seven vertices with five edges between them forming

three clusters. Note that this graph representation does not distinguish between hydrogen bond types. Nor does it distinguish multiple hydrogen bonds between two molecules, which was not observed in the systems studied here, but could arise in other systems. In the instance where two different hydrogen bond types are possible between a molecule pair (e.g., in the case of a water molecule hydrogen bound to a nitric acid molecule, where each molecule contains both a hydrogen bond donor and acceptor site), each hydrogen bond type was separately counted when measuring total hydrogen bond populations.

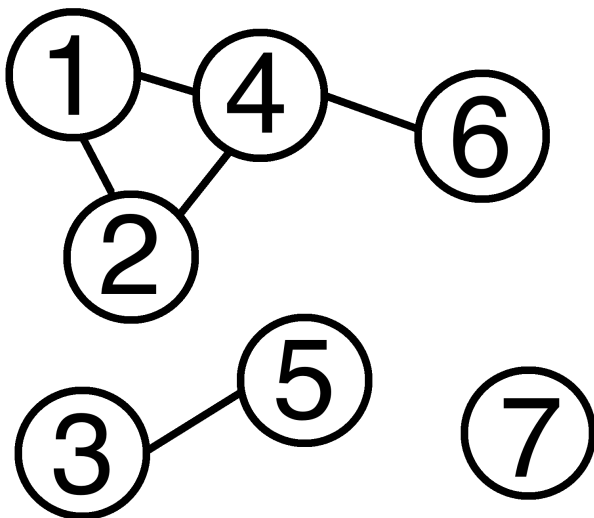


Figure 4.3: A graph with seven vertices and five edges resulting in three clusters.

The simulation trajectory file, hydrogen bond types and cut-off criteria are input to ChemNetworks[84] which generates as output a list of all hydrogen bonds present for each analyzed frame of the trajectory. From this list of hydrogen bonds, we calculate an adjacency matrix, A , defined as an $N \times N$ symmetric matrix

$$A = \begin{bmatrix} a_{1,1} & a_{1,2} & \dots & a_{1,j} & \dots & a_{1,N} \\ a_{2,1} & a_{2,2} & \dots & a_{2,j} & \dots & a_{2,N} \\ \vdots & \vdots & \ddots & \vdots & \vdots & \vdots \\ a_{i,1} & a_{i,2} & \dots & a_{i,j} & \dots & \vdots \\ \vdots & \vdots & \vdots & \vdots & \ddots & \vdots \\ a_{N,1} & a_{N,2} & \dots & \dots & \dots & a_{N,N} \end{bmatrix} \quad (4.1)$$

where N is the number of solute molecules in the system, and whose matrix element a_{ij} takes a value of one if there is at least one hydrogen bond present between a site on molecule i and a site on molecule j , and a value of zero otherwise. Therefore, the adjacency matrix

$$A = \begin{bmatrix} 0 & 1 & 0 & 1 & 0 & 0 & 0 \\ 1 & 0 & 0 & 1 & 0 & 0 & 0 \\ 0 & 0 & 0 & 0 & 1 & 0 & 0 \\ 1 & 1 & 0 & 0 & 0 & 1 & 0 \\ 0 & 0 & 1 & 0 & 0 & 0 & 0 \\ 0 & 0 & 0 & 1 & 0 & 0 & 0 \\ 0 & 0 & 0 & 0 & 0 & 0 & 0 \end{bmatrix} \quad (4.2)$$

describes the vertices, edges and resulting connectivity depicted in Figure 4.3.

The adjacency matrix is traversed to catalog all of the clusters in the corresponding frame of the trajectory. The total number of each size cluster is tallied, along with the molecular composition of those clusters, where cluster size is defined as the number of molecules participating in the hydrogen-bonded cluster. The average number of connections (edges) of each type, as defined by the identity of the molecules being connected, per molecule type is also obtained. Finally, the adjacency matrix is used to identify specific structures and substructures. A structure is defined as a cluster with a specific combination of constituent vertices (molecules types) connected by specific edges. A substructure is defined as a connected graph, also with specific vertices and edges, that may have connections to other vertices not in the substructure graph, i.e. it is a subgraph of a structure. For example, the subgraph containing 1, 2, 4 and 6 is a substructure, structure and cluster. However, the subgraph containing 1, 2 and 4 is a substructure only. Thus, the subgraphs identified in a given structure search will always be a subset of those found in the analogous substructure search.

Structure and substructure searches were performed for all simulated systems. Structure searches are implemented to identify clusters at low extracted water and nitric acid concentrations. In the high $[\text{HNO}_3]_{aq,i}$ systems, where the total number of hydrogen bonds present in the system is much larger, substructures are used to interpret hydrogen bonding topologies. For example, the local hydrogen bonding topologies of a given O_T atom are difficult to probe with specific structure searches due to the proliferation of possible cluster and thus

structure types in high hydrogen bonding concentration systems. Substructure searches capture the hydrogen bonding near the O_T atom without having to explicitly distinguish between all possible branching structures.

4.3.5 QM Calculations of 1:2 TBP:HNO₃

To compare with experimental infrared (IR) spectra, quantum mechanical (QM) vibrational analysis calculations were completed on TBP-HNO₃ coordination topologies hypothesized in the literature. Geometry optimization and vibration calculations were conducted in Gaussian09[125] using the B3LYP hybrid functional with a 6-31G(d) basis set[126]. Additional QM calculations using the ADF software[88] with the PBE and BLYP GGA exchange-correlation functionals and a TZP basis set were used to confirm the calculated peak shift. In those calculations, solvation was modeled using the conductor-like screening model (COSMO)[127] for a *n*-hexane solvent, whose dielectric most closely matches *n*-dodecane's.

4.3.6 IR Spectroscopy

Aqueous solutions were prepared from analytical grade reagents and ultra-pure (18 M Ω) deionized H₂O. The densities of all solutions were determined using a calibrated 1 mL pipette and weighing the 1 mL volume of each solution at room temperature. Dodecane was acquired from Fisher Scientific and used as received. Concentrated HNO₃ was obtained from Aldrich Chemicals, Milwaukee, WI. Stock solutions of varying nitric acid concentration were made with deionized water. TBP was acquired from Alfa Aesar and used as received to produce a 20% by volume solution with *n*-dodecane acquired from Aldrich.

TBP extraction was conducted using 1 mL total volume for both organic and aqueous phases. Pre-contact aqueous phase nitric acid concentrations were 4.4 and 13.0 M. All liquid-liquid systems were contacted for 5 minutes using a Fisher Scientific Standard Vortex Mixer and equilibrated for 5 minutes in a Clay Adams Compact II Centrifuge. The organic phase was subsampled and the complexed nitric acid was stripped through the same contacting

process with an aqueous phase of degassed water. The stripped nitric acid was subsampled and measured through acid-base titration using a sodium hydroxide solution and phenolphthalein indicator. Sodium hydroxide solutions were prepared in freshly degassed water and standardized by titration with potassium hydrogen phthalate to a phenolphthalein end point. All titration mass measurements were obtained using a Mettler Toledo PM4600 Delta Range balance. Samples of the organic phase were taken prior to stripping for spectroscopy, which was performed using a Nicolet 6700 FTIR. Organic solutions were deposited on the sampling surface and covered with a plastic shield to prevent evaporation. Spectra were taken in the range of 4000 to 600 cm^{-1} . Each spectrum contained 64 scans at 2 cm^{-1} resolution.

4.3.7 Monte Carlo Lattice Calculations

Monte Carlo (MC) calculations of bond percolation on a square lattice were conducted to determine the cluster size distribution for a finite lattice without periodic boundary conditions. The site-to-site “bonds” on a 15 by 15 square lattice were populated randomly with a given probability, p . We carried out simulations with values of p ranging from 0.22 to 0.38. Clusters formed from the lattice sites connected by the randomly generated bonds were then counted for 10,000 iterations for each of the simulated bond probabilities. The resulting distribution of cluster sizes was compared to that from MD simulation to facilitate comparison to percolation in a finite system.

4.4 Results

4.4.1 Overview

The results are organized as follows. Total hydrogen bonding is reported and discussed. Then, the observed populations of hydrogen bonds are shown to be consistent with an equilibrium binding model. Next, the hydrogen bonding data extracted from simulation are used to identify edges between molecular vertices and then identify clusters. Clusters are

analyzed to count the populations of structures and substructures. QM and IR results are compared to validate cluster geometries observed in simulation with respect to nitric acid hydrogen bonding to the TBP phosphoryl oxygen. Then, large clusters that form under high acid and water extraction are analyzed to identify a possible mechanism for the third phase transition. Lastly, the large cluster results are compared to MC finite lattice calculations of bond percolation to confirm that observed cluster size distribution statistics are consistent with percolation on a finite system.

4.4.2 Overall Hydrogen Bonding Behavior

Figure 4.4 shows the number of hydrogen bonds of each type for all systems studied normalized by the total number of oxygen atoms of that hydrogen bond type. Several observations are made from this data. First, $O_T - H_N$ is the strongest hydrogen bond in all systems where it is present. Shown in the upper left panel of Figure 4.4, the TBP hydrogen bonding participation is primarily driven by the amount of nitric acid present. When less nitric acid is present than TBP, the TBP hydrogen bonds more with water. However, as the amount of nitric acid present increases, nitric acid displaces water in hydrogen bonding with TBP, and the concentration of extracted water decreases, resulting in fewer TBP- H_2O hydrogen bonds as shown in the upper right panel of Figure 4.4. The minimum in TBP- H_2O hydrogen bonds corresponds to saturation of the TBP with nitric acid in the form of the 1:1 species. Beyond this point, for $[HNO_3]_{org} > 0.74$ M, the number of TBP hydrogen bonds increases only slightly with additional nitric acid or water. This indicates little hypercoordination of the O_T oxygen occurs. Additional nitric acid and water molecules will therefore hydrogen bond to each other rather than directly to the extractant. This is observed in Figure 4.4 where the numbers of $O_N - H_N$ and $O_N - H_W$ hydrogen bonds increase significantly from $[HNO_3]_{org} = 0.74$ to 1.25 M.

Water is observed to preferentially hydrogen bond to other water at the low acid concentration systems, $[HNO_3]_{org}$ of 0.41 and 0.67 M, rather than nitric acid. While the H_2O-H_2O hydrogen bonds do not make up the majority of water-containing hydrogen bonds, they

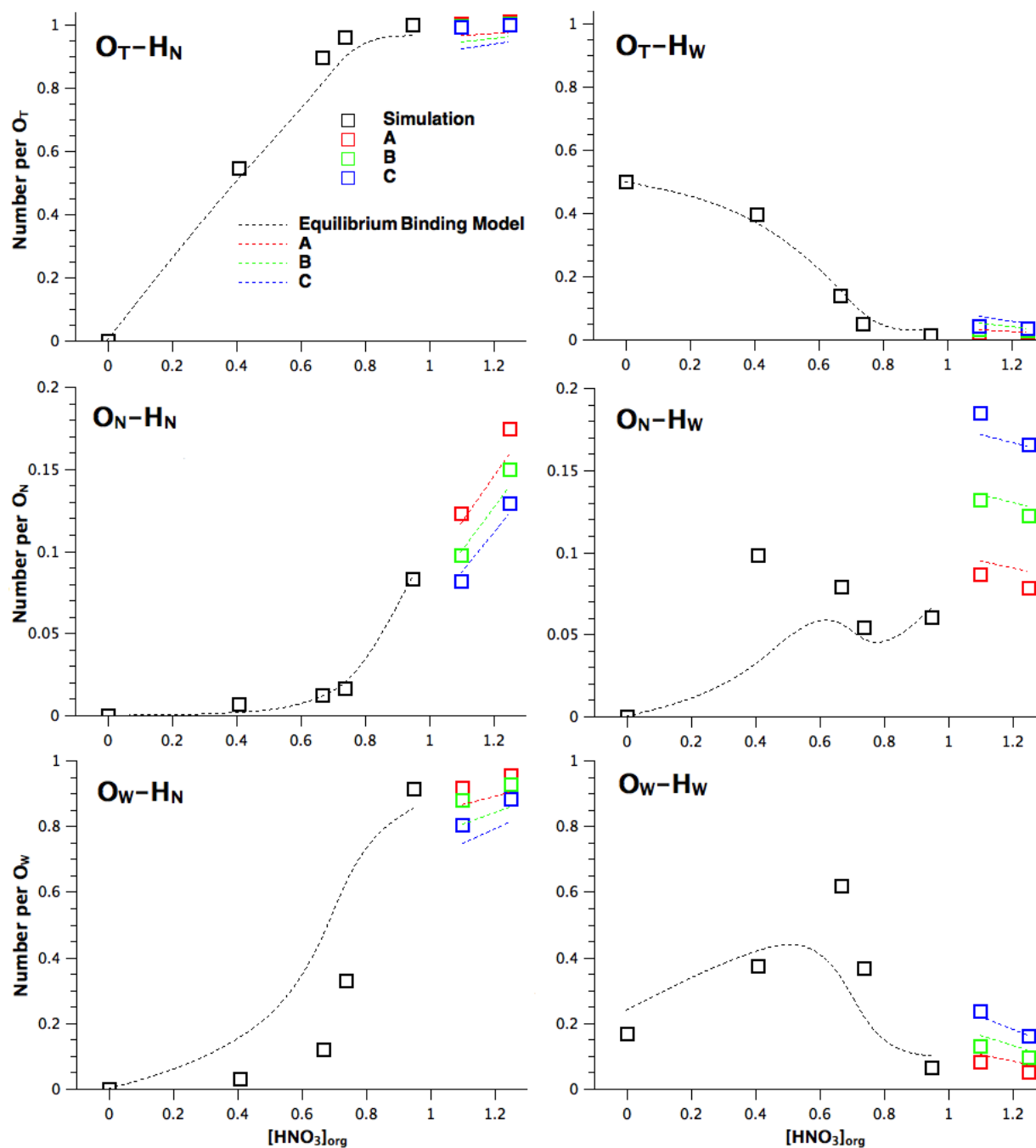


Figure 4.4: The average number of each type of hydrogen bond across all systems, normalized by the total number of oxygen atoms of that hydrogen bond type, is plotted as data points. The top panels give hydrogen bonds with the oxygen bond acceptor belong to TBP, the middle panel for nitric acid and the lower panel for water. Calculated numbers of each hydrogen bond type from the equilibrium binding model are plotted as dashed lines.

are comparable to the number of HNO₃-H₂O hydrogen bonds despite the [HNO₃]_{org} concentrations of 0.41 and 0.67 M being significantly larger than that of H₂O. The number of H₂O-H₂O hydrogen bonds increase as [HNO₃]_{org} increases from 0 to 0.67 M even as the total number of water molecules in the system decreases between systems. This is attributed to the increase in nitric acid that occupies the O_T sites, liberating the water molecules which then preferentially interact with each other rather than the already-complexed nitric acid molecules.

4.4.3 Equilibrium Binding Model

To describe the competitive hydrogen bonding equilibrium and relative binding strengths in these simulations, equilibrium binding constants were calculated for each hydrogen bond type. The equilibrium binding constant $K_{O_\alpha-H_\beta}$ of an arbitrary hydrogen bond is

$$K_{O_\alpha-H_\beta} = \frac{[O_\alpha - H_\beta]}{[O_{\alpha,free}][H_{\beta,free}]} \quad (4.3)$$

where α is the molecule type of the oxygen atom in the hydrogen bond and β is the molecule type of the hydrogen atom and $[O_{\alpha,free}]$ and $[H_{\beta,free}]$ are the concentrations of uncomplexed hydrogen bonding sites of that type.

This simplified model neglects the surrounding environment of any particular hydrogen bond, and aims primarily to give a qualitative understanding of the relative binding strengths and resulting equilibria. The equilibrium binding constants for the six hydrogen bond types were fit simultaneously to all the hydrogen bond data plotted in Figure 4.4 using a least squares criterion. The resulting binding constants are given in Table 4.3. To evaluate the goodness of the fit, these binding constants were used to calculate the number of hydrogen bonds for each system to compare to the values they were fit to. The fitted values assume no hypercoordination is possible and the hydrogen bond formation probabilities are independent for all atom sites on a molecule. The goodness of fit is an indicator of how much these assumptions impact hydrogen bond formation. The equilibrium binding model predictions for hydrogen bond formation in all systems are shown in Figure 4.4 as dashed lines. Overall,

the fit was good, implying that the binding constants using the aforementioned assumptions reasonably define the total numbers of hydrogen bonds. However, as the least squares fit weights all the data equally and more data exists for $[\text{HNO}_3]_{org} > 0.74 \text{ M}$ than $< 0.74 \text{ M}$, the fit is better in the high acid systems. We would not expect that one set of binding constants would be equally good in both high and low acid regimes as, for example, the formation of hydrogen bonded clusters at high acid (that do not occur regularly at low acid) would impact the probabilities of hydrogen bond formation differently than the more simple speciation observed at low acid. From the fitted values, there is a clear distinction in binding strength between every hydrogen bond type, with those containing O_T or H_N atoms being stronger than with other oxygen and hydrogen atoms sites.

Table 4.3: The binding constants, defined in Equation 4.3, for the six hydrogen bonds obtained through least squares fitting of the simulation data.

Hydrogen Bond	Binding Constant, $k [\text{mol}/\text{L}]^{-1}$
$\text{O}_T - \text{H}_N$	3×10^7
$\text{O}_T - \text{H}_W$	2×10^2
$\text{O}_N - \text{H}_N$	1×10^4
$\text{O}_N - \text{H}_W$	2×10^0
$\text{O}_W - \text{H}_N$	2×10^6
$\text{O}_W - \text{H}_W$	6×10^1

4.4.4 TBP, HNO_3 and H_2O Structures and Substructures

To further analyze molecular organization beyond the populations of specific hydrogen bonds, the remaining sections implement network analysis to identify and measure speciation and large clusters. Snapshots of several representative structures are given in Figure 4.5. This figure shows: I) the 1:1 TBP- HNO_3 structure, II) a 1:2 TBP- HNO_3 Chain structure, and III) a more complicated $(\text{TBP})_2(\text{HNO}_3)_3(\text{H}_2\text{O})$ cluster. The structure searches will count structures such as those shown in I and II and the substructure searches will parse the more complicated networks, such as that shown in III, that are too numerous to account for

individually.

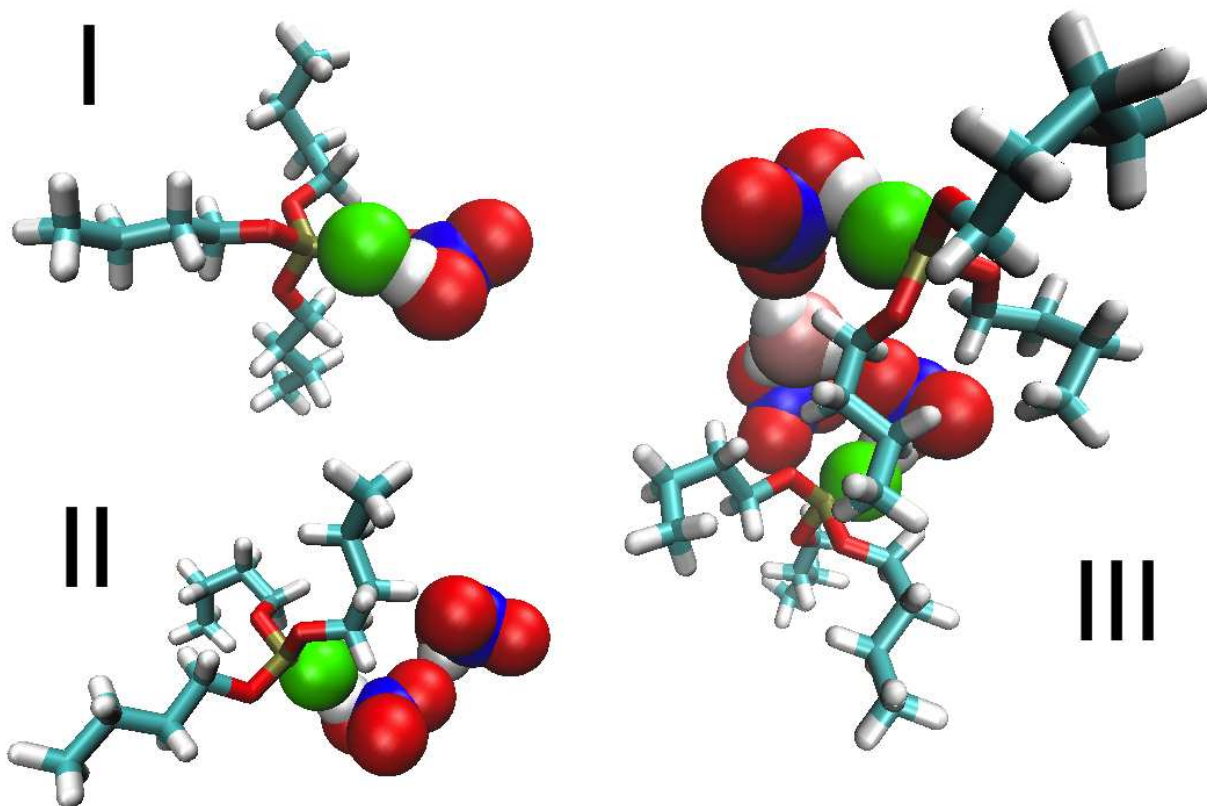


Figure 4.5: Snapshots of several hydrogen-bonded structures. Part I shows a 1:1 TBP-HNO₃ structure, part II a TBP-HNO₃-HNO₃ Chain structure and part III a (TBP)₂(HNO₃)₃(H₂O) cluster. The oxygen atoms in the nitric acid are shown in red, the nitrogen in blue and the hydrogen in white. For water, the hydrogen atoms are white and the oxygen atoms pink. The TBP atoms are depicted as solid bonds with the green phosphoryl oxygen atom expanded for visualization.

The average number of selected structures observed in simulation across the range of system compositions are given in Figure 4.6. The TBP-HNO₃ adduct is the only isolated structure to exist in significant quantities. At equal concentrations of TBP and HNO₃, about two thirds of both are in a TBP-HNO₃ structure without additional connections. TBP-H₂O is only observed before HNO₃ dominates the TBP coordination. Small amounts of the 1:2 TBP:HNO₃ Chain and Shared structures exist at high acid concentrations, both of which are disrupted by the addition of water. Small amounts of non-hydrogen bonded TBP, water and nitric acid, are observed and shown in Appendix B along with the additional structures

TBP-HNO₃-H₂O, TBP-H₂O-HNO₃ and TBP-(HNO₃)(H₂O). Not plotted are 1:2 TBP:H₂O Shared and Chain species, as these are rarely detectable. When they occur, they are typically substructures present in larger clusters as the available hydrogens for hydrogen bonding on the water molecules are nearly always coordinated.

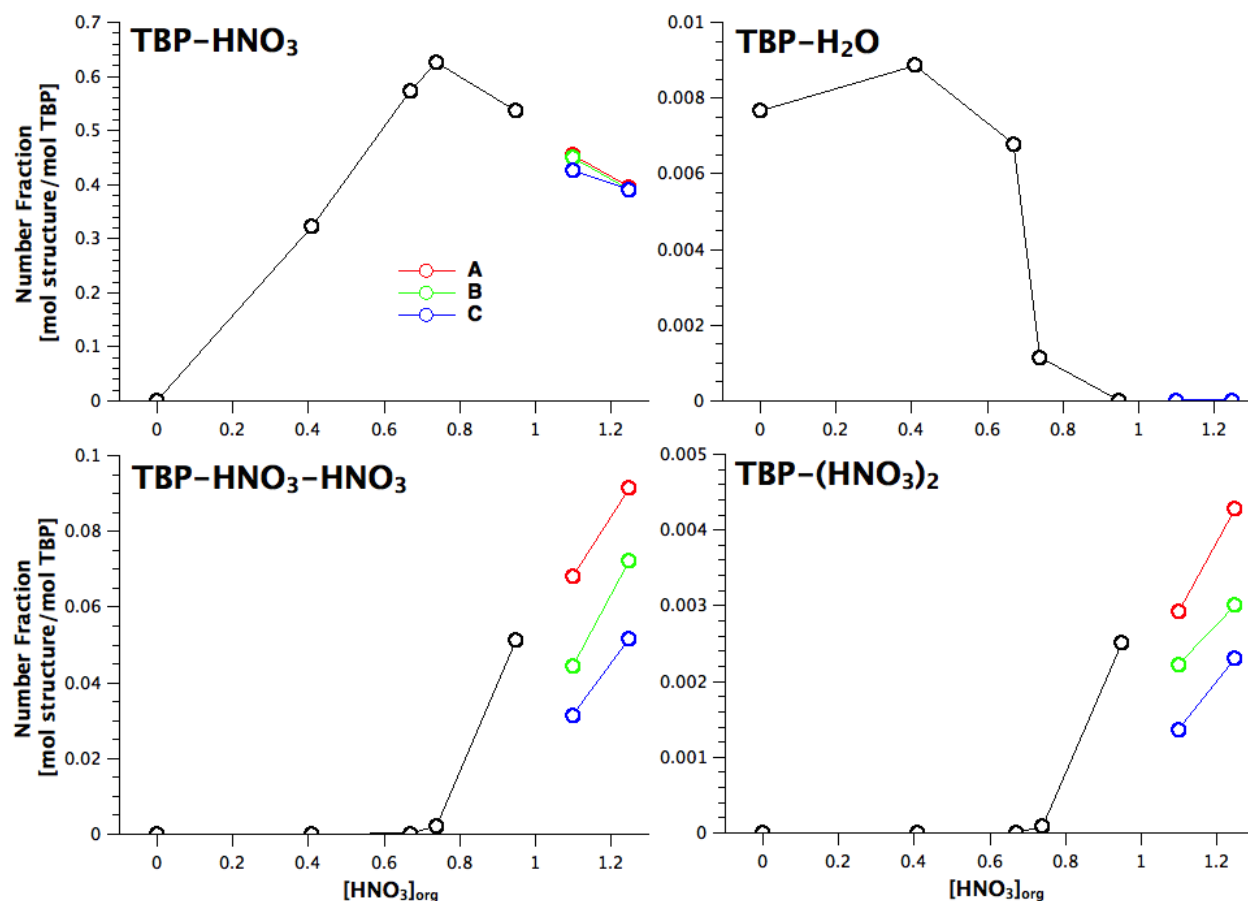


Figure 4.6: The average number observed in simulation, per TBP molecule, of the TBP-HNO₃, TBP-H₂O, TBP-HNO₃-HNO₃ Chain and TBP-(HNO₃)₂ Shared structures is plotted for each system. Systems with one water concentration are in black while the red, green and blue data points correspond to the systems with three water concentrations.

Overall, the structure search results indicate that most structures outside of the 1:1 TBP:HNO₃ are either not present or are a part of larger structures. Thus, to elucidate the local coordination behavior, substructures were analyzed. Figure 4.7 shows the average number of TBP-HNO₃-HNO₃, TBP-HNO₃-H₂O, TBP-H₂O-TBP and TBP-H₂O-H₂O substructures per TBP molecule. Corresponding results for TBP-H₂O-HNO₃, TBP(H₂O)₂,

TBP(H₂O)(HNO₃) and TBP(HNO₃)₂ substructures are given in Appendix B. Significant quantities of the TBP-HNO₃-H₂O and TBP-HNO₃-HNO₃ Chain substructures were observed, particularly in the high acid systems. Also observed, but only in the low acid systems, are the TBP-H₂O-TBP water bridge and the TBP-H₂O-H₂O Chain. Neither are significant species after ingrowth of the 1:1 TBP:HNO₃. With respect to hypercoordination of the TBP, shown in the substructures in Appendix B, up to 0.05 TBP(H₂O)(H₂O) Shared substructures per TBP were observed. This number is reduced in the high acid systems as the TBP coordination site is replaced with nitric acid molecules. In the high acid systems, on average less than 0.035 TBP(H₂O)(HNO₃) and 0.02 TBP(HNO₃)(HNO₃) Shared substructures per TBP are present at a time. The nitric acid molecule, in comparison to water, may be sufficiently large to limit TBP’s ability to participate in hypercoordination. Furthermore, as the TBP-HNO₃ hydrogen bond is the strongest such interaction in the system, the saturation of the TBP occurs as soon as there are equal numbers of nitric acid and TBP molecules. As discussed below, these findings agree with the nitric acid coordination behavior anticipated by the QM calculations and experimental IR spectroscopy.

4.4.5 QM Vibrational and IR Spectroscopic Determination of 1:2 TBP:HNO₃ Topology

The predominance of the hydrogen bonded 1:1 TBP:HNO₃ complex for $[\text{HNO}_3]_{org} < [\text{TBP}]$ is well established experimentally in the literature [120, 121], but TBP adducts, and particularly the connectivity of those adducts, beyond this species are not well understood. In particular, there have been multiple proposed structures for the 1:2 TBP:HNO₃ complex that forms as TBP extracts nitric acid beyond the 1:1 ratio[28, 128, 129]. The two possible coordination geometries for the second nitric acid molecule of the 1:2 TBP:HNO₃ complex are depicted in Figure 4.8, labeled as the “Shared” and “Chain” structures. Using IR spectroscopy, Ferraro *et al.* concluded the second nitric acid molecule hydrogen bonds to the “back” (non-hydroxy) oxygen of the first nitric acid of the already-formed 1:1 adducts[28] rather than hypercoordination of the O_T oxygen of the TBP molecule. They identified a

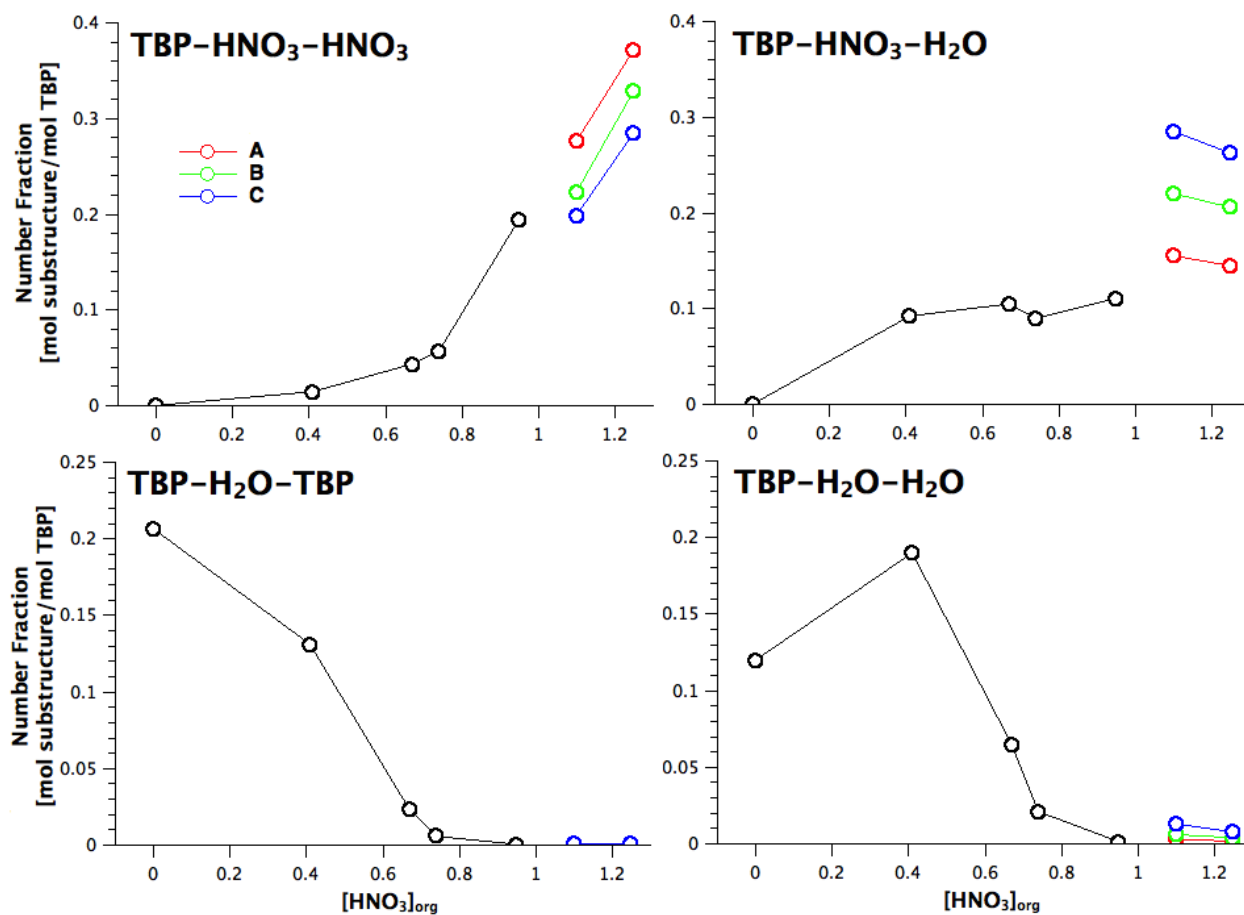


Figure 4.7: The average number observed in simulation, per TBP molecule, of the TBP-HNO₃-HNO₃ Chain, TBP-HNO₃-H₂O, TBP-H₂O-TBP and TBP-H₂O-H₂O substructures is plotted for each system. Systems with one water concentration are in black while the red, green and blue data points correspond to the systems with three water concentrations.

shift in a nitric acid O-N-O asymmetric stretch peak near 1670 cm^{-1} which occurs when TBP extracts nitric acid in excess of a 1:1 ratio. The peak shift is interpreted as a signature of a different coordination environment for the back oxygens. We investigate this hypothesis with QM calculations for these vibrational modes and more precisely assess how different coordination geometries impact the peak shift.

Based on the QM calculations, the vibrational mode near 1670 cm^{-1} , assigned in the literature to an O-N-O asymmetric stretch, was found to be highly coupled to a “wag” motion of the hydrogen bonded hydrogen atom of the nitric acid. Thus, the wavenumber

of the vibration peak is expected to be influenced by the hydrogen bonding coordination of the H_N atom. The QM calculated frequencies for the two nitric acid molecules for two different $[\text{HNO}_3]_{aq,i}$ concentrations are plotted in Figure 4.8 along with experimental spectra. The acid concentrations were chosen to be either below ($[\text{HNO}_3]_{aq,i} = 4.4 \text{ M}$) or above ($[\text{HNO}_3]_{aq,i} = 13.0 \text{ M}$) the 1:1 TBP: HNO_3 equivalence point. The lower wavenumber peak corresponds to the O-N-O stretch and H wag vibrational mode of the inner nitric acid (directly bonded to TBP) while the higher wavenumber peak corresponds to a vibration for the outer nitric acid. The QM calculated shift in peak location of 23 cm^{-1} between the first and second nitric acid molecules agrees with the experimentally observed peak shift of roughly 25 cm^{-1} for the Chain structure. In comparison, the peak shift for the Shared structure calculated by QM is only 7 cm^{-1} and arises due to asymmetry in the positioning around the O_T atom. Additional QM calculations bolster this interpretation, with the BLYP and PBE functionals with a TZP basis set giving peak separations, respectively, of 29 and 45 cm^{-1} for the Chain structure and 6 and 5 cm^{-1} for the Shared structure.

Comparison of the calculated energy shift suggests that as nitric acid is extracted beyond a 1:1 ratio, the additional nitric acid is not hydrogen bonded to the TBP. This is consistent with our simulations, as shown in the upper left panel of Figure 4.4, where only a small amount of O_T hypercoordination (seen in less than 5% of O_T atoms for each system) is observed in each combination of nitric acid and water.

The utility of simulation in understanding this extraction system, and particularly at high acid compositions, stems largely from experimental limitations for assessing the hydrogen bonding behavior. However, previous simulation studies of this system discussed in the Introduction have not captured this behavior accurately, showing hypercoordination of the O_T atom. Ensuring that simulated nitric acid coordination beyond the 1:1 ratio is primarily with other extracted nitric acid and water, and not through TBP hypercoordination, is a non-trivial and direct comparison with experiment that supports validity of the hydrogen bonding topologies observed in our simulations.

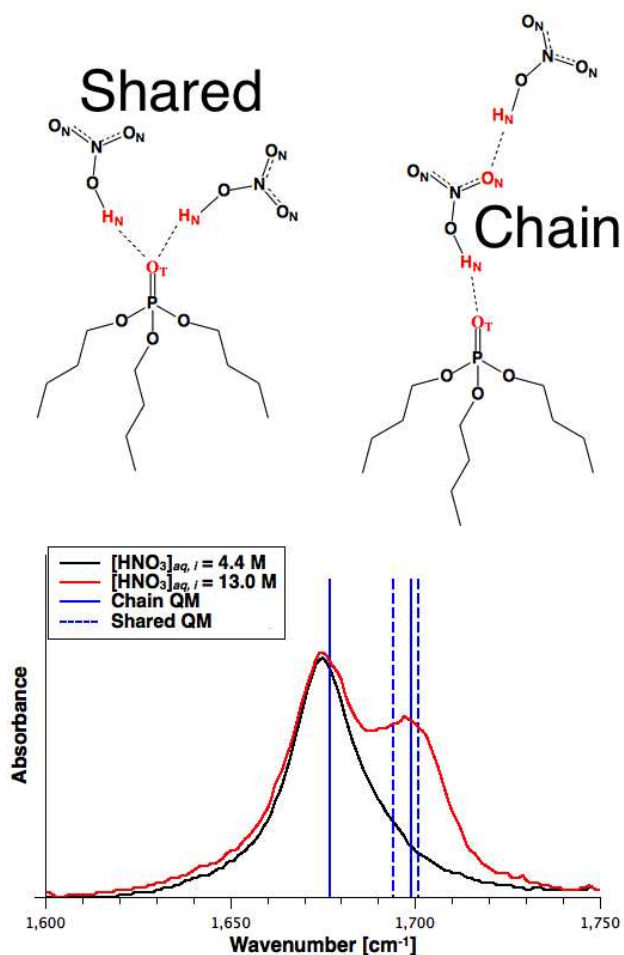


Figure 4.8: The vibrational modes for the coupled hydrogen wag and O-N-O asymmetric stretch of the nitric acid determined for the Shared and Chain configurations with QM calculations are plotted with the experimentally observed spectrum. Of the two configurations, the calculated frequencies of the vibrations for the two nitric acid molecules in the Chain structure match the peak separation observed experimentally.

4.4.6 Large Cluster Analysis

The formation of large clusters in the high nitric acid and water concentration systems where third phase formation has been reported are of interest as representative of the incipient phase transition[3]. Figure 4.9, taken from a frame of a 1.25 M $[\text{HNO}_3]_{org}$ C simulation, shows numerous clusters present. Two visually isolated clusters are highlighted. To observe the degree of cluster formation through large hydrogen bonding networks in the 1.10 and 1.25 $[\text{HNO}_3]_{org}$ systems, Figure 4.10 shows a semilog plot of the average number of a given

cluster size observed in simulation.

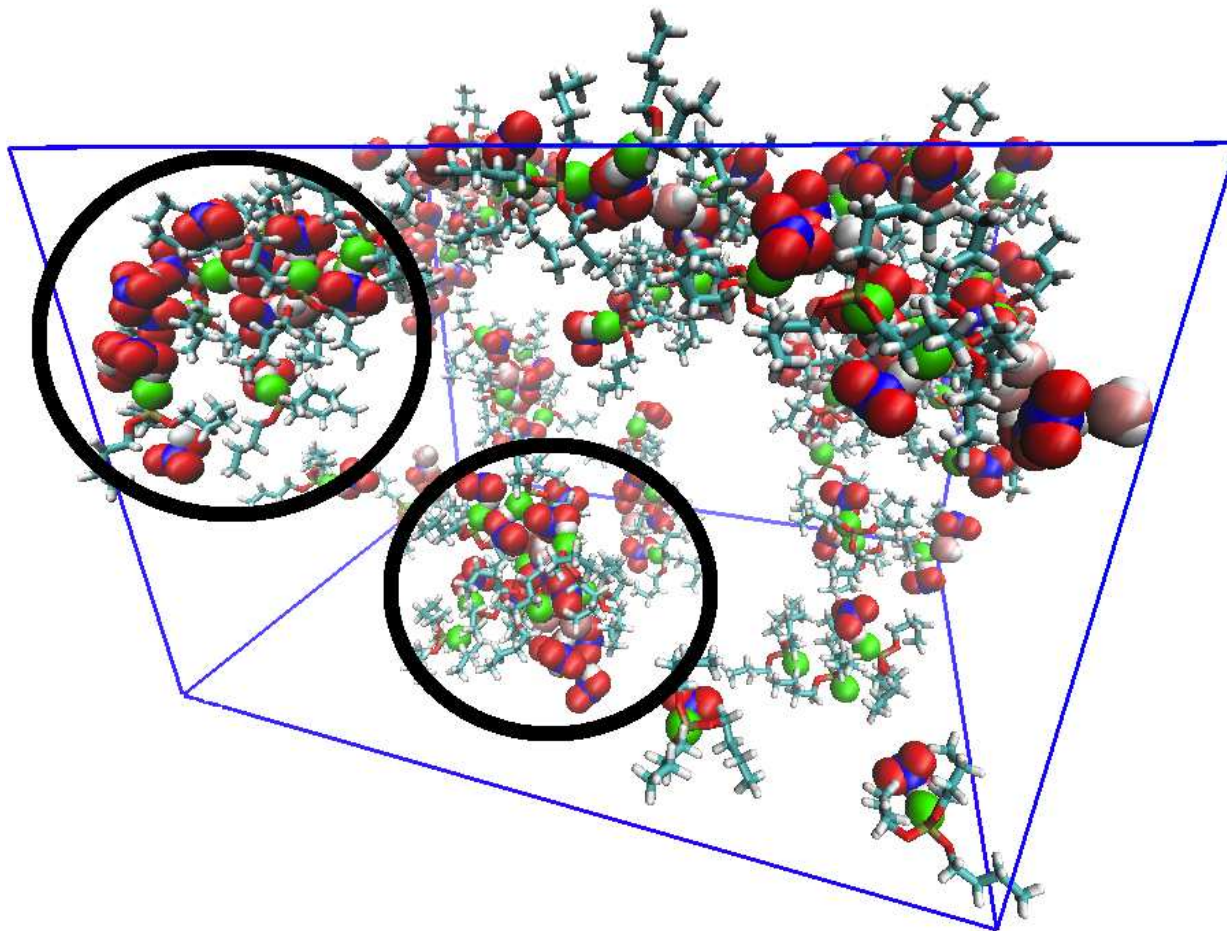


Figure 4.9: A snapshot from the 1.25 M $[\text{HNO}_3]_{org}$, 0.31 M $[\text{H}_2\text{O}]_{org}$ C system. TBP is represented with the phosphoryl oxygen atom colored green and enlarged. Nitric acid and water molecules are represented with oxygen atoms shown in red for nitric acid and pink for water. Nitrogen atoms are blue and hydrogen atoms in both molecules are white. Dodecane is omitted for clarity. Two examples of isolated clusters are highlighted.

A semilog plot of the number of clusters of size M allows identification of an average association free energy, μ , for the addition of a molecule to an $(M - 1)$ -sized cluster. The average number, N_M , of clusters of size M is

$$N_M \propto e^{-\mu M/k_B T}. \quad (4.4)$$

where k_B and T are the Boltzmann constant and the temperature, respectively[105].

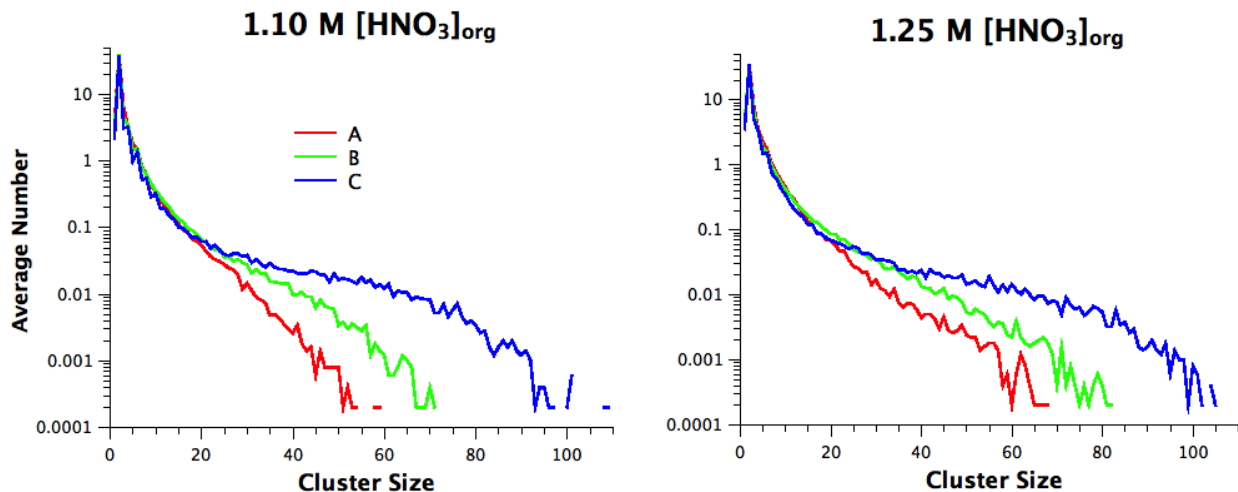


Figure 4.10: The semilog histograms of the average number observed versus cluster size are plotted for the 1.10 and 1.25 M $[\text{HNO}_3]_{org}$ A (0.15 M $[\text{H}_2\text{O}]_{org}$), B (0.23 M $[\text{H}_2\text{O}]_{org}$) and C (0.31 M $[\text{H}_2\text{O}]_{org}$) systems.

As observed in Figure 4.10 for those six systems, when the logarithm of the number observed is linear with cluster size over a range of cluster sizes, Equation 4.4 is an appropriate description of cluster formation. The constant μ value corresponds to the average free energy cost of adding a molecule to the cluster. This implies the average cost of adding a molecule to a cluster is independent of cluster size for a given range. In the data given here, this range starts near $M = 20$, where the local speciation effects that skew the low cluster sizes ends, and applies until the finite size effects of the simulation appear, resulting in increased noise and a drop-off to zero in observed concentration. For the highest water concentration (system C), the large clusters sizes are probable enough that the finite size effects may occur at lower cluster sizes, resulting in the downward inflection of the histogram before the appearance of significant noise in the data.

The average association free energy μ for 1.10 M $[\text{HNO}_3]_{org}$ C (0.31 M $[\text{H}_2\text{O}]_{org}$) is lower than for 1.25 M $[\text{HNO}_3]_{org}$ B (0.23 M $[\text{H}_2\text{O}]_{org}$) even though there are more total polar molecules in the latter system. Therefore, the value of μ is not just a function of the total number of polar solutes capable of hydrogen bonding. The addition of water reduces μ more effectively than the addition of nitric acid. As water content increases from A to C

compositions for both 1.10 M $[\text{HNO}_3]_{org}$ and 1.25 M $[\text{HNO}_3]_{org}$ systems, the slope and hence free energy for increasing cluster size decreases. At low enough slope, the free energy cost of cluster growth may be low enough to form macroscopic clusters, perhaps corresponding to third phase formation.

One test to determine if the large clusters in the 1.25 M $[\text{HNO}_3]_{org}$ C (0.31 M $[\text{H}_2\text{O}]_{org}$) system are indicative of third phase formation is to compare the composition of large clusters observed in simulation to experimental composition data. Kertes[3] reported third phase formation for a high $[\text{HNO}_3]$ system where the heavy organic phase contains a 1:3 TBP: HNO_3 ratio. We were unable to create a third phase experimentally with a 15 M $[\text{HNO}_3]_{aq,i}$ system to verify this or identify how much the water uptake increases approaching the phase boundary. In the systems simulated here, without metal ions, we do not expect small, strongly associated reverse micelles that depend on a metal center for geometric orientation. Rather, we anticipate formation of large clusters to precede phase separation.

To avoid counting speciation of small clusters when calculating the composition of large clusters, the change in large cluster composition was measured from the start of the constant average μ range, at $M = 20$, until finite size effects emerge. Depending on the choice of that limit, either $M = 60$ or $M = 80$, the TBP: HNO_3 ratio for the 1.25 M $[\text{HNO}_3]_{org}$ C system is 1:2.9 or 1:2.7, respectively. This is consistent with the 1:3 value given in the literature, and suggests that large clusters seen in simulation correspond to the aggregates in third phase formation.

We noted above that the ratio of nitric acid to water impacts the association free energy, μ , of growing the large clusters. We hypothesize that increasing water content encourages formation of larger clusters due to the need for both hydrogen bond acceptors and donors to grow extended hydrogen bond networks. In the systems studied, $[\text{TBP}]$ and $[\text{HNO}_3]$ are both much larger than $[\text{H}_2\text{O}]$, resulting in a significant excess of oxygen (hydrogen bond acceptor) sites. Cluster growth is limited by the number of hydrogen bond donor sites present in these systems. Figure 4.11 plots the total number of hydrogen bonds per molecule for nitric acid

and water in the 1.25 M $[\text{HNO}_3]_{org}$ systems. The figure shows, in addition to adding more hydrogen-bond capable atoms that yield more hydrogen bonds per atom than nitric acid, increasing the water concentration from A to C further increases the number of hydrogen bonds per water molecule. Thus, for these systems, water molecules provide hydrogen atoms in the oxygen-rich environment that enable growth of large hydrogen bonded clusters.

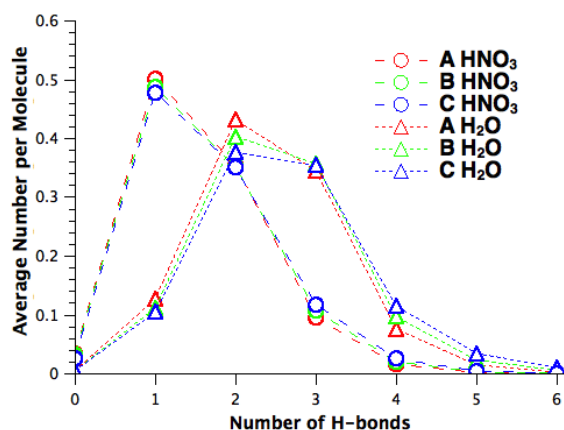


Figure 4.11: The average number of hydrogen bonds per molecule for water and nitric acid are given for the A-C systems for 1.25 M $[\text{HNO}_3]_{org}$. While the numbers for nitric acid are generally unchanged with increasing water, the probabilities for water shift towards larger values as water is added to the system.

4.4.7 Percolation and Lattice Monte Carlo Comparison

To further investigate the third phase transition in simulation, and determine if the trend in the cluster size distribution profile in 1.25 M $[\text{HNO}_3]_{org}$ C, as compared to the exponential distribution of A and B, is indicative of reverse micelle formation or percolation, two higher water concentrations were simulated for the 1.25 M $[\text{HNO}_3]_{org}$ system. Figure 4.12 shows the cluster size distributions for several water concentrations in the left panel, including new cases of 0.38 M and 0.46 M $[\text{H}_2\text{O}]_{org}$. In the additional simulations, the cluster size distribution curve for clusters up to size 50 is no longer linear on the semilog plot but are instead consistent with a power law distribution as predicted by Flory-Stockmayer theory[116] for polymer systems near the percolation point. Also for the highest water concentration sys-

tems, a peak emerges at large cluster size, between 100 and 120 depending on the water concentration, disrupting the power law distribution. A snapshot of such a cluster, with 117 total polar solutes, is shown in Figure 4.13. To determine if this is showing micelle formation at a characteristic size or if instead this is a finite size effect limiting the size of the spanning clusters formed in simulation, the data is compared to cluster size distribution data for a Monte Carlo simulation of bond percolation for bond probabilities approaching the percolation threshold. The Monte Carlo results are plotted in the right panel of Figure 4.12. The cluster size distribution statistics for the finite size percolation from the lattice model are compared with the simulation data. They both exhibit the peak at high cluster sizes for the spanning clusters in the finite system. Therefore, we conclude that the simulation data are consistent with, for clusters up to the simulation size implemented here, third phase formation resulting from a percolation phase transition and not reverse micelle formation.

Recently, Singh *et al.* reported micelle formation and third phase formation for the TBP/dodecane/water/nitric acid system[130]. However, they implemented high water concentrations in the mono-phasic organic phase simulations that do not correspond to the concentrations of water extracted from 1-3 M nitric acid aqueous solutions. As a result, they apparently observed the formation of an emerging aqueous phase, rather than growth of micelles or a third phase, owing to the exaggerated organic phase water concentration.

4.5 Conclusions

Network analysis was used to assess hydrogen bonding in molecular dynamics simulations of nitric acid and water extracted into a 20% TBP in *n*-dodecane organic phase for various organic phase nitric acid and water concentrations. The populations of different hydrogen bond types observed in simulation was successfully modeled using a set of equilibrium binding constants for each possible hydrogen bond type fit to cluster statistics obtained from the simulations. This simplified but intuitive model for competitive hydrogen bonding captured the overall numbers of each hydrogen bond in the simulated systems and allows for direct comparison between strengths of different hydrogen bond types. Such an equilibrium binding

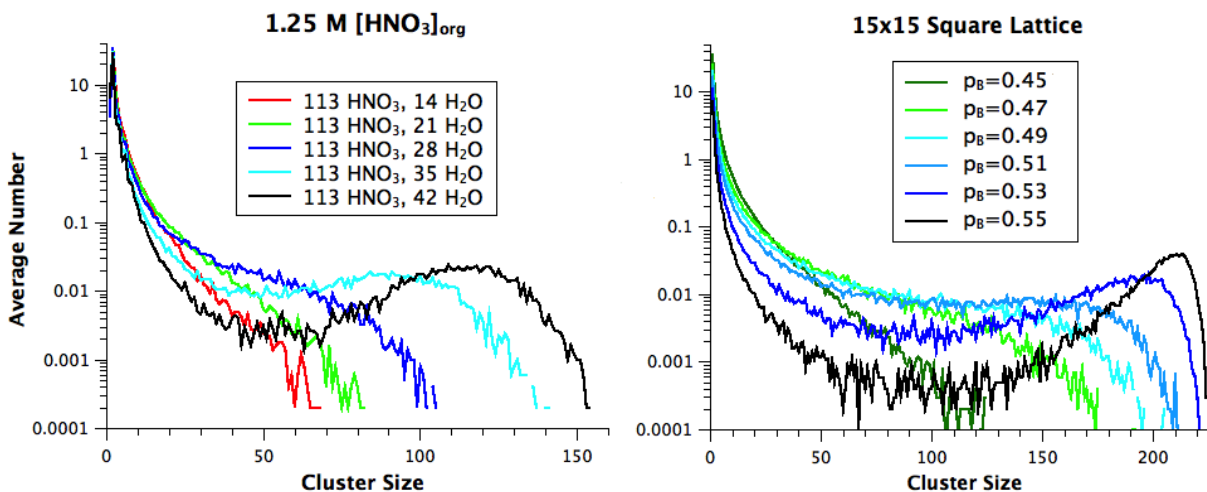


Figure 4.12: The cluster size distribution for the 1.25 M [HNO₃]_{org} systems, with additional higher water concentration simulations, is compared to the cluster size distribution plots for a 15 by 15 square lattice for a range of bond probabilities. The similarity in distribution statistics implies that the simulation data is showing a percolation phase transition with finite size effects creating spanning clusters between 100 and 120 polar solutes in size.

model provides a method to predict how speciation and extraction varies depending on binding strength which could be implemented to account for variables including molecule type, concentration and temperature.

The network of hydrogen bonds between solutes was reduced to a graph consisting of molecule vertices and edges reflecting the presence of hydrogen bonding between the molecules. This allowed convenient graph theoretic identification of hydrogen bonded clusters, as well as concentrations of frequently occurring structures and substructures, defined as clusters or subsets of clusters with specific composition and connectivity. Those structures and substructures, particularly ones distinguishing the local hydrogen bonding topology of the TBP phosphoryl oxygen atom, shows how simple solute-extractant adducts develop into the large clusters that precede phase separation. Simulation results were compared to experimental behavior of nitric acid coordination to TBP in a 1:2 TBP:HNO₃ ratio. Updated force field parameters used in the TBP model implemented here show coordination behavior consistent with experimental data.

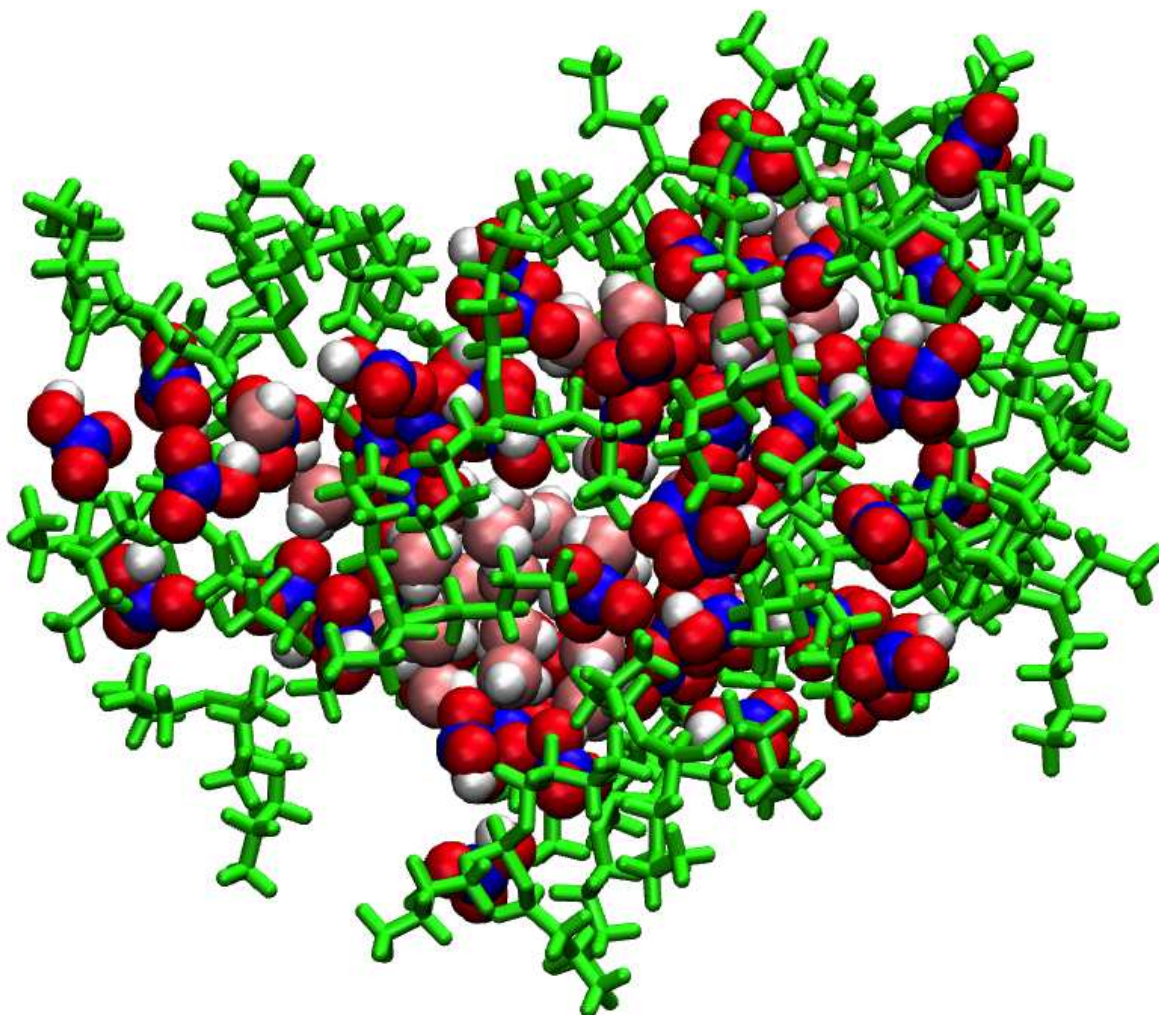


Figure 4.13: Pictured is a snapshot of a large cluster, of size 117, from the 1.25 M $[\text{HNO}_3]_{org}$ C system. TBP molecules are depicted as green for clarity.

At high nitric acid and water concentrations, the cluster size distributions were found to be consistent with a percolation phase transition mechanism for third phase formation in this system. The quantitative analysis performed for these systems, and the network interpretation of the third phase transition, has wide applicability to self-associating liquid systems governed by hydrogen bonding, including other extraction systems with alternative types of acids, extractants, diluents and metal ions. The cluster size distribution profiles described here will be applied in future studies to identify phase transitions, either through

percolation or micelle formation. The network analysis presented here can be used to interpret the effects of individual hydrogen bond formation probabilities, dependent on acid type and relative concentrations of polar solutes and described by the equilibrium binding constants, on macroscopic phase behavior.

4.6 Acknowledgements

The authors thank the Colorado School of Mines High Performance Computing center for computational resources and Nuclear Regulatory Commission Faculty Development Award NRC-HQ-11-G-38-0062 for funding.

CHAPTER 5
THE ROLE OF EXTRACTANT STRUCTURE IN THE ASSOCIATION OF
EXTRACTED URANYL NITRATE CLUSTERS

5.1 Introduction

The Plutonium Uranium Reduction EXtraction (PUREX) process is a solvent extraction process that separates fissile f -elements like uranium and plutonium in used nuclear fuel from fission and corrosion products. The used fuel, dissolved in an aqueous nitric acid medium, is contacted with an organic phase that consists of a long chain hydrocarbon diluent and an amphiphilic extractant[2]. In PUREX, the solvating organophosphorus extractant is tributyl phosphate (TBP), which selectively extracts tetra- and hexavalent metal ions. After the phases are contacted, the extractants and coordinated metal ions form complexes, referred to here as clusters, with charge neutralizing nitrate anions that are transferred to the organic phase.

Under sufficiently high metal ion loading, third phase formation can occur where the organic phase partitions into two phases. These two phases are a “light” phase, primarily comprised of organic diluent, and a “heavy” phase, rich in extractant and metal ions in addition to coextracted acid and water[4, 5]. Third phase formation is undesirable from a processing perspective since the contactor banks are designed for a two phase system. Additionally, when extracting significant quantities of plutonium the dense third phase is a criticality concern as the plutonium uncontrollably concentrates. For a given system, the maximum extracted metal concentration before third phase formation is referred to as the limiting organic concentration (LOC). Rao *et al.* demonstrated that the neutral solvating organophosphorus extractant structure has a significant impact on third phase formation. The thorium nitrate LOC for TBP is increased significantly by changing the butyl tail groups

to amyl groups. Also increasing the LOC, although less so than the alkyl chain length, is changing TBP's phosphate head group to a phosphonate group, *i.e.*, removing one of the bridging oxygens. Therefore, the thorium nitrate LOCs for TBP, triamyl phosphate (TAP) and dibutyl butyl phosphonate (DBBP) are ordered as TBP<DBBP<TAP. These three extractants are depicted in Figure 5.1.

Uranyl nitrate extracted by TBP also results in third phase under sufficiently high metal and acid loading, although the limiting concentration is higher than for thorium. While thorium nitrate and uranyl nitrate complexes are structurally different, there are likely still dependencies on extractant structure leading to different uranyl nitrate LOCs, as there are for thorium, that have not been reported in the literature. Uranium has been studied more with MD simulation in the literature. Therefore, we investigate organic phase uranyl nitrate clusters. To understand how these structural changes affect inter-cluster association and inform cluster solubility and third phase formation[78], we will compare uranyl-centered clusters of these three extractants.

Third phase formation in PUREX-type extraction systems has been studied experimentally in the literature. Metal-centered clusters and their interactions leading to third phase formation have been interpreted using small angle neutron scattering (SANS)[10, 16–20, 27, 29] and x-ray scattering (SAXS)[23]. The TBP aggregates formed by self-association, hydrogen bonding or metal complexation are modeled as hard spheres or ellipsoids with a uniform attractive surface potential. This modeling approach provides an intuitive explanation for the metal concentration dependence on phase separation. Higher concentrations of extracted metal leads to increased attraction between TBP clusters of all types. After some threshold concentration, this results in phase separation. However, this approach of treating TBP clusters as hard spheres or ellipsoids with an attractive surface potential requires significant assumptions about the cluster geometries and their interactions. All TBP clusters are unlikely to form monodisperse species even if the metal-centered clusters with TBP are of identical composition. The metal centered clusters are also unlikely to be approximated

well as hard spheres with no alkyl tail overlap. The interaction between the polar cores would also be best described with a long-range potential rather than a surface attraction.

While those significant assumptions are required for scattering modeling, molecular dynamics (MD) simulation could provide atomistic resolution to the interactions between extracted metal clusters. MD also avoids the necessity of making *a priori* assumptions about cluster shape, interaction potential and size dispersity. Previous simulation research on PUREX-type extraction systems of organic phase species have examined non-metal systems. These studies have investigated TBP self-association[56, 58, 59, 98] and TBP extraction of water and nitric acid[55, 99]. Simulations of TBP extraction of uranyl ions have centered on interfacial behavior without emphasis on organic phase speciation of the extracted clusters. However, as third phase formation depends on the solubility of the extracted organic phase species and is not an interfacial phenomenon, understanding the inter-cluster associations that govern phase behavior can be addressed in simulations of the organic phase of the extraction systems only.

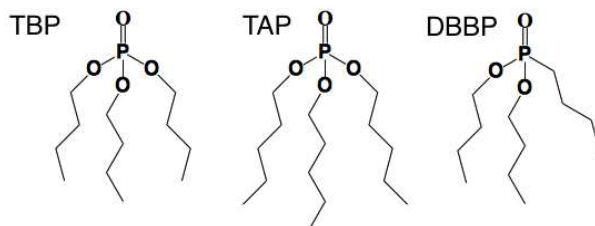


Figure 5.1: Molecular structures of the amphiphilic extractant molecules tributyl phosphate (TBP), dibutyl butyl phosphonate (DBBP) and triamyl phosphate (TAP).

This work describes the efforts to understand the nature of interactions between uranium-centered organophosphorus extractant clusters using MD simulation. First, a uranyl potential for use with organic phase clusters is parameterized and tested in simulation. That uranyl potential is implemented in low uranium concentration simulations to isolate and measure the cluster pairwise interactions in *n*-dodecane. Comparisons are made between low concentration uranium systems and high concentration systems to demonstrate that the

pairwise interactions in the dilute limit are not significantly different than the inter-cluster interactions of the concentrated uranyl systems. The changes in cluster association resulting from extractant structure are then investigated.

5.2 Methodology

5.2.1 Quantum Mechanical Calculations

Quantum mechanical calculations were conducted with the NWChem software package[131] using the B3LPY functional with the DZP basis set and Stuttgart ECP for uranium[132] and aug-cc-pVDZ basis sets for non-uranium atoms. Single point calculations used the same basis sets with second order Møller-Plesset perturbation theory.

5.2.2 Force Fields

The potentials used for TBP, *n*-dodecane, nitric acid and water are the same as we have previously implemented[99]. Bonded and nonbonded parameters for nitrate are taken from the Generalized AMBER Force Field (GAFF)[32]. Uranium non-bonded parameters for pairwise interaction with the extractant phosphoryl oxygen is given in Table 5.1. The uranyl nonbonded Lennard-Jones pairwise potentials use the nonbonded parameters implemented by Kerisit and Liu[75]. Charges for the uranyl and nitrate atoms are also given in Table 5.1. Development of these values are described in the Results section.

Table 5.1: The uranyl and nitrate charges are given. The pairwise nonbonded uranium-phosphoryl oxygen parameters developed in this study are also given.

Atoms	$\sigma[\text{\AA}]$	$\epsilon[kcal/mol]$
U-O _{extractant}	2.9002	0.1961
Atom	Charge [q_e]	QM Mulliken Charge [q_e]
U _{uranyl}	2.10	2.43
O _{uranyl}	-0.45	-0.63
N _{nitrate}	0.75	0.65
O _{nitrate}	-0.45	-0.45

5.2.3 Simulations Details and Compositions

The post-contact organic phase simulation compositions for TBP systems are taken or extrapolated from Chiarizia *et al.*[10, 17, 27] for uranyl nitrate, water and nitric acid extraction into 20% by volume TBP in a *n*-dodecane medium. The 40 uranyl nitrate simulation corresponds to the LOC for uranium. For comparison, the DBBP and TAP compositions use the same 20% extractant volume fraction and uranium concentrations with the nitric acid and water concentrations scaled with the free extractant concentration. The compositions are given in Table 5.2 for TBP, Table 5.3 for DBBP and Table 5.4 for TAP. The resulting simulation box sizes were $62 \pm 1 \text{ \AA}$ for the 6 uranyl nitrate compositions and $66 \pm 1 \text{ \AA}$ for the higher uranium concentration compositions.

Table 5.2: The uranium concentrations and MD box compositions for the simulations with TBP.

$[U](mol/L)$	0.03	0.12	0.20	0.26
# $UO_2(NO_3)_2$	6	20	30	40
# TBP	12	131	131	131
# HNO_3	0	89	69	49
# H_2O	0	18	20	22
# $C_{12}H_{26}$	604	604	604	604

Table 5.3: The uranium concentrations and MD box compositions for the simulations with DBBP.

$[U](mol/L)$	0.03	0.12	0.20	0.26
# $UO_2(NO_3)_2$	6	20	30	40
# DBBP	12	134	134	134
# HNO_3	0	18	20	22
# H_2O	0	93	73	53
# $C_{12}H_{26}$	604	604	604	604

Molecular dynamics simulations were completed using the GROMACS 4.5.5 software package[89]. The isobaric isothermal NPT ensemble with periodic boundary conditions and a leap-frog Verlet integrator were used for all simulations. Pressure was set to 1 bar with

Table 5.4: The uranium concentrations and MD box compositions for the simulations with TAP.

$[U](mol/L)$	0.03	0.12	0.20	0.26
# $UO_2(NO_3)_2$	6	20	30	40
# TAP	12	108	108	108
# HNO_3	0	73	53	33
# H_2O	0	15	16	18
# $C_{12}H_{26}$	604	604	604	604

the Berendsen barostat and temperature to 300 K with the Berendsen thermostat for equilibration and the Nose-Hoover thermostat for production. Particle-Mesh Ewald summation was used for long-range electrostatic summation with a 15 Å cut-off for short range electrostatic and van der Waals interactions. The LINCS algorithm was used for constraining hydrogen-containing bonds to enable use of a 2 fs time step. The initial configurations were generated using Packmol[133] with the $UO_2-(NO_3)_2-(Extractant)_2$ complexes in “assembled” configurations derived from QM geometry optimization and the remaining molecules inserted randomly. Energy minimization and 2 ns NPT equilibration was followed by 50 ns NPT sampling for each run. For the low uranium concentration (6 uranyl nitrate complexes) systems, reported data is averaged over 13 total runs. Higher concentration (20, 30 or 40 uranyl nitrate complexes) averaged over 5 runs.

5.3 Results

5.3.1 Organic Phase Uranyl Parameterization

Organic phase simulations will require implementation of MD potentials that accurately depict the organic phase clusters. Existing uranyl potentials have all been developed for an aqueous environment[67, 68, 75, 76] where the uranyls have fivefold coordination. Extracted $UO_2-(NO_3)_2-(TBP)_2$ clusters have been shown experimentally to have sixfold coordination with both nitrates coordinating in a bidentate manner[7, 134]. This cluster is shown in Fig-

ure 5.2. We have observed that the aqueous uranyl potentials result in fivefold coordination in the organic phase, where the two nitrate counterions bind in a monodentate fashion and the remaining three coordination spots are occupied by TBP. Existing uranyl potentials will therefore not suffice for the organic phase simulations of interest. The slower dynamics of the organic phase species means that using polarizable force fields will result in untenably long computational times to collect sufficient data for quantitative analyses. Therefore, development of a non-polarizable uranyl potential is necessary. Jensen *et al.* showed that the uranyl coordination environment is consistent, as described previously, for the low concentration up to the LOC[7].

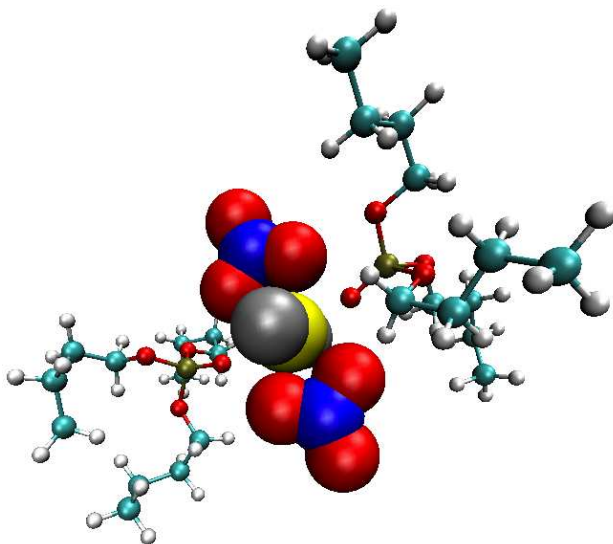


Figure 5.2: An organic phase TBP/uranyl/nitrate cluster. The nitrate anions and TBP extractants coordinate the uranyl ion in a plane perpendicular to the uranyl ion oriented into and out of the page. The nitrate anions are bidentate, resulting in sixfold total coordination.

The objective of the uranyl nitrate parameter fitting is to find classical MD potentials that sufficiently capture the uranium-centered cluster behavior as best as possible using the existing validated TBP potential. The potential is not intended for implementation outside the $\text{UO}_2\text{-(NO}_3)_2\text{-(Extractant)}_2$ cluster, where “Extractant” refers to the family of solvating organophosphorus extractants in this study. In the parameterization process, the properties required to fit to are the extractant dissociation energy and the equilibrium binding distances

in *n*-dodecane solvent. Additional objectives sought during the parameterization process include maintaining atomic charges on the uranyl nitrate complex as close as possible to those derived from the quantum mechanically calculated Mulliken population analysis, while preserving uranyl nitrate charge neutrality. Not all of these objectives could be simultaneously achieved with assumptions inherent in the computational simulation methods applied.

Trimethyl phosphate (TMP) and nitrate rigid dissociation energies from the $\text{UO}_2\text{-(NO}_3)_2\text{-(TMP)}_2$ complex were generated from the initial QM-derived cluster geometry optimization using single point calculations for $\text{U-O}_{\text{phosphoryl}}$ or $\text{U-O}_{\text{nitrate}}$ distances of 2 to 12 Å in increments of 0.2 Å. The TMP molecule was kept rigid in the equatorial plane of the TMP and nitrate coordination. The TMP was used in place of TBP to reduce calculation time for the carbon that are assumed to not impact the electronic structure of the phosphate head group, an approximation that has been made in the literature[37]. The values fitted for to the QM data for the TMP ligand are used for TBP, DBBP and TAP in simulation.

The workflow for the fitting process was implemented as follows: selected parameters in the classical MD potential were fit to the gradient of the dissociation energy profile for either TMP or nitrate using ForceFit[135]. For the subset of geometries chosen to fit in the dissociation profile, the MD parameters chosen to fit were optimized to the sum of least squares of the difference between the MD and QM atomic potential energy gradients. Each included geometry in the fitting is weighted equally. For example, by fitting over a selected range of $\text{U-O}_{\text{phosphoryl}}$ distances for TMP dissociation, $\text{U-O}_{\text{phosphoryl}}$ L-J σ and ϵ terms could be obtained. This process could be implemented for any subset of terms in the MD potential, although pairwise potentials not strongly coupled to the dissociation coordinate would likely not yield meaningful values. The QM and MD dissociation energy profiles, for a fitted set of $\text{U-O}_{\text{phosphoryl}}$ L-J parameters, are plotted in Figure 5.3. The fitted MD parameters were implemented in a 2 ns gas phase MD simulation of a single cluster (with TMP) to check the coordination distances. For fitted parameters that generate accurate gas phase coordination distances, a long simulation was ran in *n*-dodecane solvent (with TBP instead of TMP)

to compare to the experimentally determined organic phase binding distances. Simulations showed, on average, the organic phase binding distances were further than the gas phase by less than 0.1 Å. Therefore, the fitted $\text{U-O}_{\text{phosphoryl}}$ L-J parameters selected for testing in simulation give a closer equilibrium binding distance in the gas phase simulation (and QM fitting process) than are observed when implemented in simulation.

Many combinations of charges and Lennard-Jones parameters were considered in the fitting process to ascertain the impact of the different parameters on the dissociation energy and equilibrium binding distances. The uranium atom center charge most strongly affected the total dissociation energy. The $\text{U-O}_{\text{phosphoryl}}$ L-J potential, in addition to the uranium charge, impacted the equilibrium binding distance. Table 5.1 gives the QM Mulliken charges and the implemented MD charges with the fitted L-J parameters. Figure 5.3 shows the QM dissociation profile for TMP with the fitted MD dissociation profile. The MD potentials were fitted over the well region of the energy profile from 2 to 5 Å, corresponding to the uranium to phosphoryl oxygen distance. Table 5.5 gives the QM, experimental and fitted MD binding distances of the $\text{UO}_2\text{-(NO}_3)_2\text{-(Extractant)}_2$ cluster.

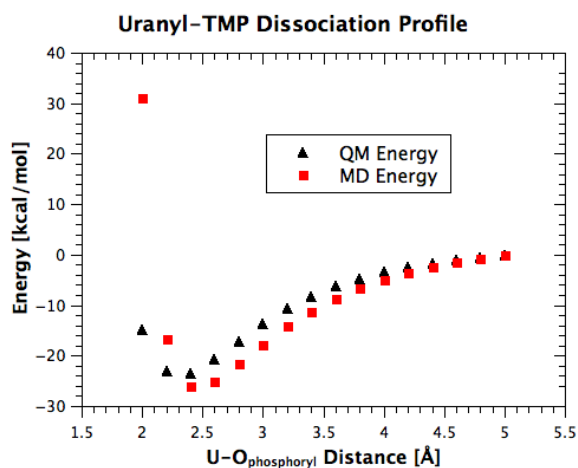


Figure 5.3: The dissociation energy profile, zeroed at 5 Å, for the TMP-uranyl nitrate complex is plotted for the QM (black) and fitted MD (red) data.

Table 5.5: The experimental, QM calculated and fitting MD simulation binding distances for the $\text{UO}_2\text{-(NO}_3)_2\text{-(TBP)}_2$ cluster (with nitrate distance restraints to enforce the $\text{U-O}_{\text{nitrate}}$ and $\text{U-N}_{\text{nitrate}}$ distances). The simulation and experimental distances are for an *n*-dodecane solvent liquid phase, while the QM calculations in the gas phase.

Atom Distance [\AA]	XAS[134]	QM	Fitted MD
$\text{U-O}_{\text{nitrate}}$	2.51	2.54	2.52
$\text{U-N}_{\text{nitrate}}$		2.99	2.98
U-O_{TBP}	2.41	2.43	2.40

We attempted to fit the nitrate dissociation in addition to extractant dissociation to have a fully dissociable potential for the entire complex. While it was possible to replicate the dissociation energy profile for nitrate, the liquid phase coordination behavior was not successfully replicated. The nitrates either reverted to monodentate coordination and engaged in “bridging” of uranyl or allowed for coordination of a third TBP. Coordinating nitrates for different parameter sets were observed to bend out of the equatorial plane in a manner not observed experimentally. We therefore used distance restraints in the MD simulation to enforce the experimentally determined bidentate coordination of the nitrate to the uranyl. The distances between the uranium atom and the coordinating oxygens of the nitrate molecule and the nitrate nitrogen atom were restrained with a $2390 \text{ kcal}/(\text{mol}\text{\AA}^2)$ harmonic potential outside of 2.49 to 2.51 \AA and 2.99 to 3.01 \AA , respectively. Figure 5.4 shows the incorrect nitrate binding behavior of the unfitted or unrestrained nitrate models compared to the correct coordination of the restrained and fitted parameters.

5.3.2 Orientation and Spatial Dependence of Uranyl Cluster Association

Experimental interpretation of inter-cluster interactions have been limited to short range, isotropic potentials. A primary objective of this investigation is to evaluate those assumptions. To determine the approximate pairwise interaction where multibody effects are as limited as possible while maintaining counting statistics, the radial distribution function is considered for the 0.03 M uranium simulations with 6 uranyl nitrate complexes with just *n*-dodecane solvent. The uranium-uranium RDFs for the 6 $\text{UO}_2\text{-(NO}_3)_2\text{-(Extractant)}_2$ clus-

ter simulations for TBP and TAP are averaged over 10 trajectories of 50 ns each. Those two RDFs are plotted in Figure 5.5. These RDFs indicate cluster association is not well described by a single coordination. Instead, multiple cluster correlation peaks exist within the hard sphere volume of the scattering model. Furthermore, significant differences exist in coordination peaks between TBP and TAP as opposed to a shift in the correlation peak corresponding to the slightly larger hard sphere volume of the TAP clusters with the amyl group carbon tails.

While differences exist in cluster association for the low concentration systems, interpreting differences in third phase formation in 20% extractant organic phases based on these inter-cluster interactions depends on how similar the cluster association is to higher concentrations. Figure 5.6 shows the RDFs averaged over 5 trajectories of 50 ns for the higher concentration TBP, TAP and DBBP systems with coextracted water and nitric acid into the 20% by volume extractant in *n*-dodecane organic phase. Here, 40 $\text{UO}_2\text{-(NO}_3)_2\text{-(Extractant)}_2$ complexes corresponds to the LOC for TBP. While the relative populations of the correlation peaks are different, the radial positions of the peaks is the same for the higher uranium concentrations as the low concentration simulations. The impact of the many-body interactions does not significantly alter the radial peak location of the pair correlation function, implying that the interactions between clusters are largely similar for the low and high concentrations. The inclusion of the PUREX solvation environment, with TBP, extracted water and nitric acid, in addition to the *n*-dodecane solvent decrease the total cluster-cluster interactions due to screening of the polar cluster association.

To better understand the cluster association and identify more specifically how it is impacted by extractant structure, the radial distribution functions for the high concentration systems are expanded to show the relative orientation of the uranyl ions at each radial distance. The orientation between two uranyles is defined by the angle formed between the -yl oxygen and the uranium atom on a uranyl and the uranium atom on the other uranyl. The orientations are counted for all four of these angles formed by each pair of uranyl ions

within 30 Å. This results in an orientation distribution approximately symmetric around 90 degrees. Figure 5.7 visually depicts one of the four $O = U - U$ angles measured for different uranyl pair orientations using ChemNetworks[84]. The angles and distances were scaled by a factor of $4\pi r^2 \sin \theta$ to account for differences in counting bin sizes to enable comparison between angle and distance combinations. The total number of counts was then normalized to unity.

The distance and orientation distribution for the TBP, TAP and DBBP systems for the 20 and 40 uranyl compositions are averaged over the 5 trajectories of 50 ns and plotted in Figure 5.8. The first row corresponds to TBP, with the 20 uranyl composition on the left and the 40 uranyl composition on the right panel. The second and third rows correspond to TAP and DBBP, respectively. The angle and distance distribution show the relative orientation of the clusters at each correlation peak. Differences between extractants can be related to the cluster orientations to determine how cluster association varies based on extractant structure.

There are three major peaks in the RDFs for the three extractants considered. Each of those peaks have different uranyl orientation distributions. The closest peak around 5-6 Å consists primarily of uranyl-uranyl orientations centered around 30 (or 150) degrees. A snapshot of this configuration is shown in Figure 5.9 A. The -yl oxygen of one uranyl is oriented towards the uranium metal center of the other uranyl ion. The the linear dioxo-cation geometry prevents completely parallel configurations as the -yl oxygens are repulsive and the nitrates and extractants in equatorial coordination plane prevents perpendicular coordination. Therefore, the uranyls orient as described in the cleft between the -yl oxygens and coordination plane. This first coordination peak is greatly reduced for the phosphonate extractant, DBBP, but largely similar between TBP and TAP and therefore independent of the alkyl tail size. This is possibly a result of the phosphonate head group of DBBP moving one of the butyl tails closer into the equatorial coordination plane, increasing the steric presence of the alkyl tail in the cleft regions.

The second RDF peak, near 8 Å, is similarly consistent between TBP and TAP while less populated for DBBP as the previously peak. This peak corresponds to the perpendicularly oriented uranyls. A cluster snapshot from the third peak region, between 10 and 12 Å, is shown in Figure 5.9 B. This coordination has little orientational preference. The reduction in peak height for TAP clusters relative to TBP and DBBP could be explained by the alkyl tail sterics of the uranyl clusters. These clusters are separated by the roughly 1 nm uranium-uranium distance and are shown in Figure 5.9 B where an alkyl tail of the left TBP in the upper right uranyl cluster is spacing the polar association between the clusters. An additional carbon in the amyl tails would reduce the population in this region.

The differences in pairwise interactions between clusters with different extractant structures may lead to the differences in cluster association that, at high uranium loading, affects the solubility of those clusters in the organic phase and therefore the LOC before phase separation. Attempts to identify long-range ordering in the high uranium concentration simulations were not sufficiently definitive to make assertions for the simulations presented here. To address the possibility of a phase transition resulting from cluster association in the form of long-range association over the domain of the phase separated region, larger simulation box sizes and longer simulation times will be implemented.

5.4 Conclusions

Nonbonded potentials for the $\text{UO}_2\text{-(NO}_3)_2\text{-(TMP)}_2$ complex were parameterized to capture organic phase behavior of uranyl nitrate extracted by solvating organophosphorus extractants. The orientational and positional dependence of the inter-cluster interactions were measured for uranyl nitrate TBP clusters and found to be similar for a range of concentrations and solvent environments. Alternative extractants to TBP showed the role of phosphate versus phosphonate head group and butyl versus amyl alkyl tails in cluster association. Increasing the alkyl tail length decreased association at the 10-12 Å correlation peak, where the uranium centers are separated by the aliphatic portion of the extractants. The differences between phosphate and phosphonate head groups impacted the closest 5-6 Å cluster asso-

ciation where the aliphatic region of the clusters are inter-penetrated. These differences in short range interactions between clusters may correspond to differences in uranyl solubility and third phase formation, but further simulation evidence will be required to demonstrate this.

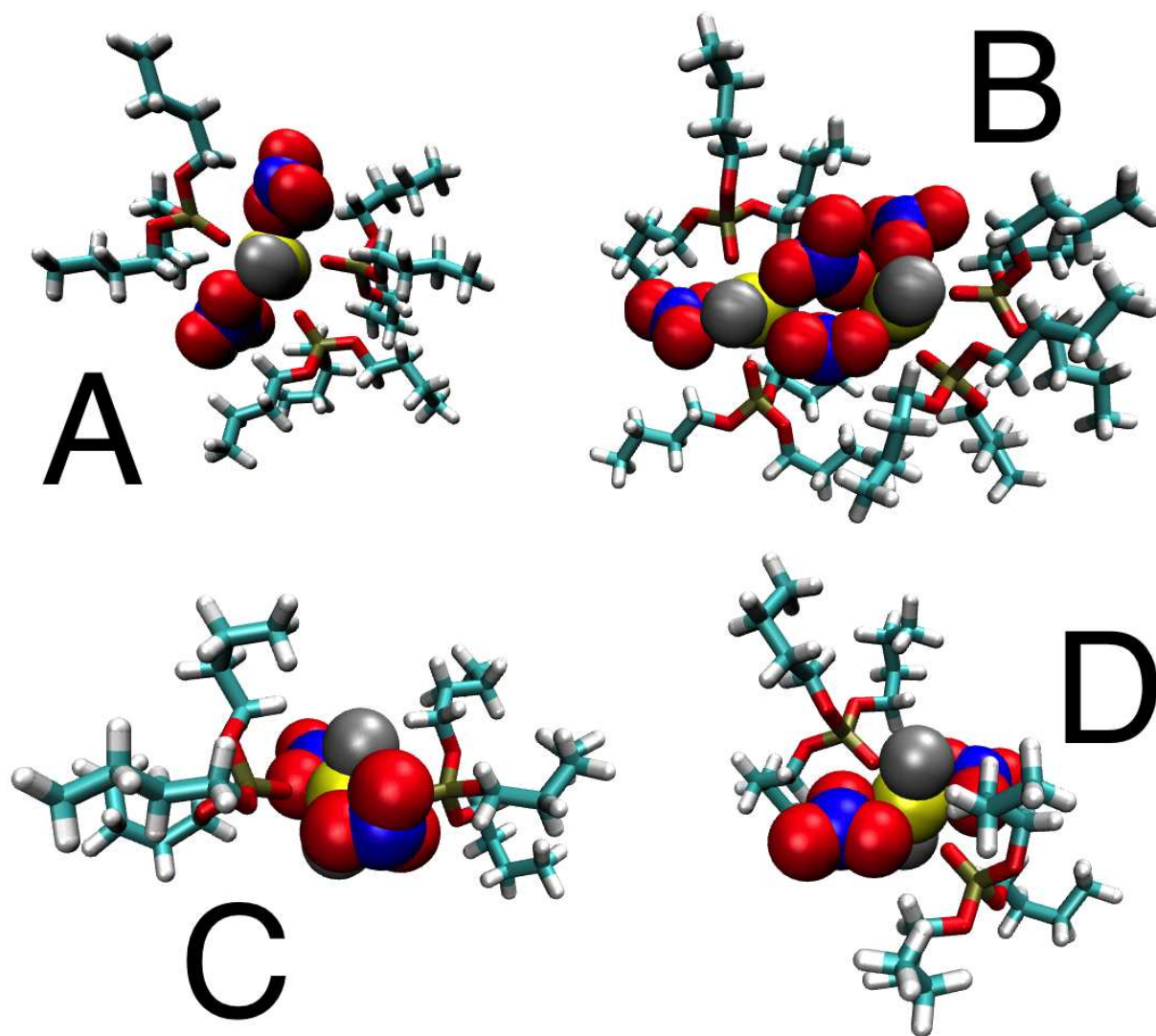


Figure 5.4: Uranyl nitrate cluster structures illustrating parameterization challenges. A) shows the 5-fold coordinate uranyl with monodentate nitrates and three binding TBPs and B) shows the 5-fold coordinate uranyl with nitrates forming a “bridge” between metal centers. C) shows the nitrate out-of-plane bending. D) shows the experimentally determined bidentate coordination.

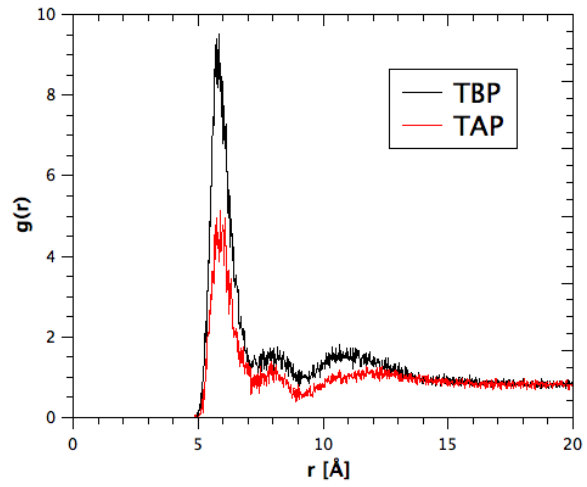


Figure 5.5: Uranium-uranium RDFs for the 6 (0.03 M) $\text{UO}_2\text{-(NO}_3)_2\text{-(Extractant)}_2$ in *n*-dodecane simulations for TBP and TAP.

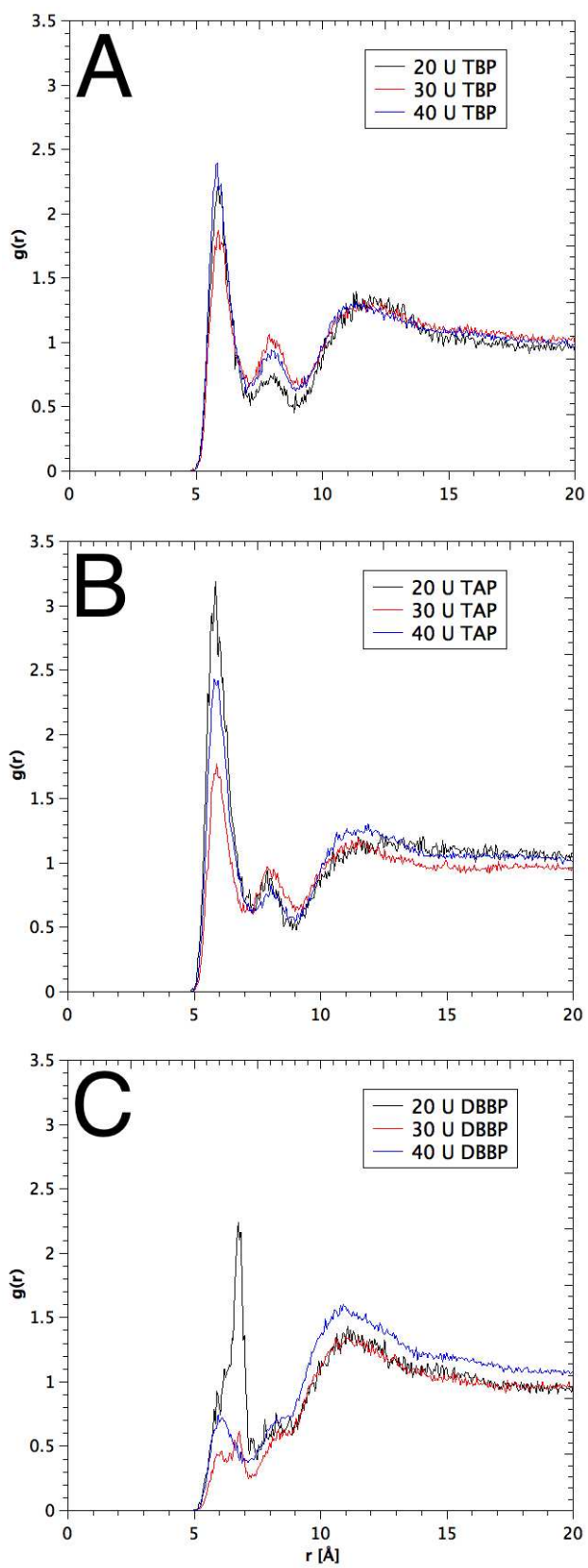


Figure 5.6: Uranium-uranium RDFs for TBP are plotted in panel A, TAP in panel B and DBBP in panel C.

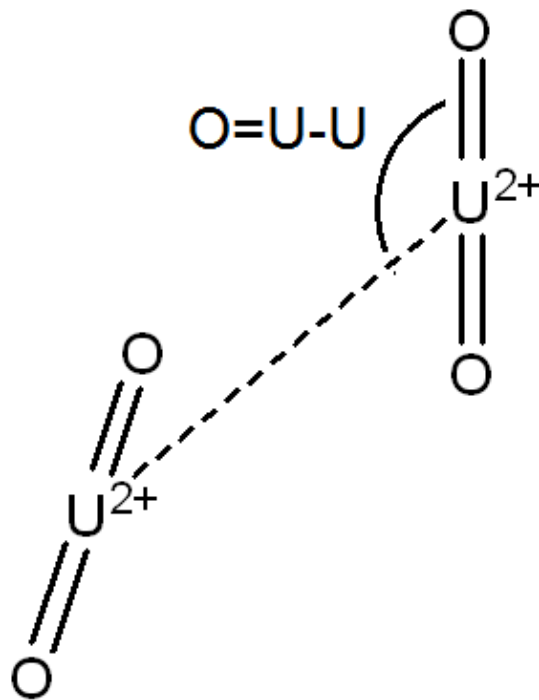


Figure 5.7: The schematic shows the angle between uranyles measured for the angle distributions. All four possible $O = U - U$ angles are counted separately for each uranyl pair within the distance cutoff, resulting in a roughly symmetric distribution around 90 degrees.

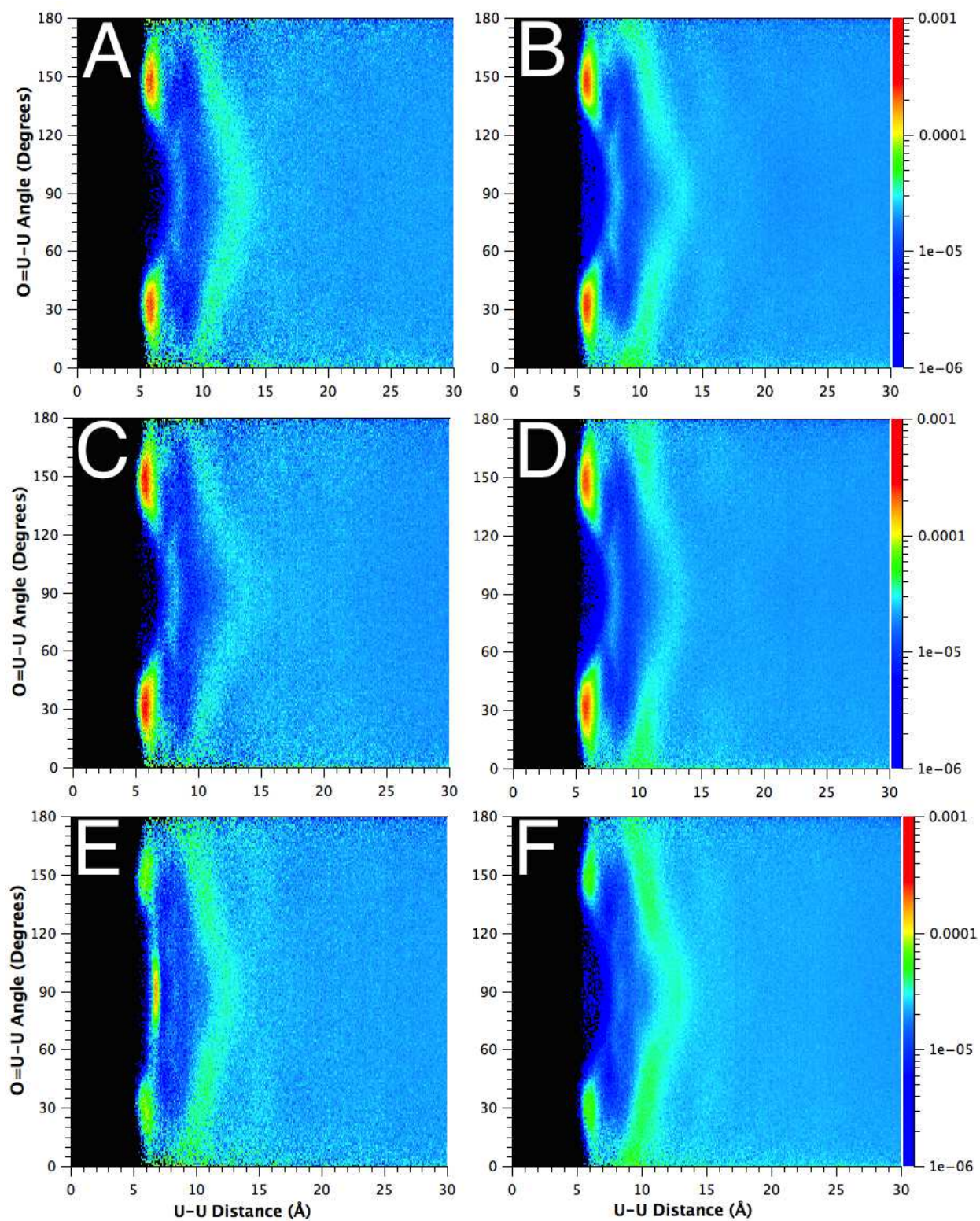


Figure 5.8: A distribution of the uranyl-uranyl orientations as a function of uranium-uranium distance. The left panels correspond to 20 uranium systems and the right panels 40 uranium systems. The top panels are for TBP systems, the middle panels for TAP and the bottom panels for DBBP.

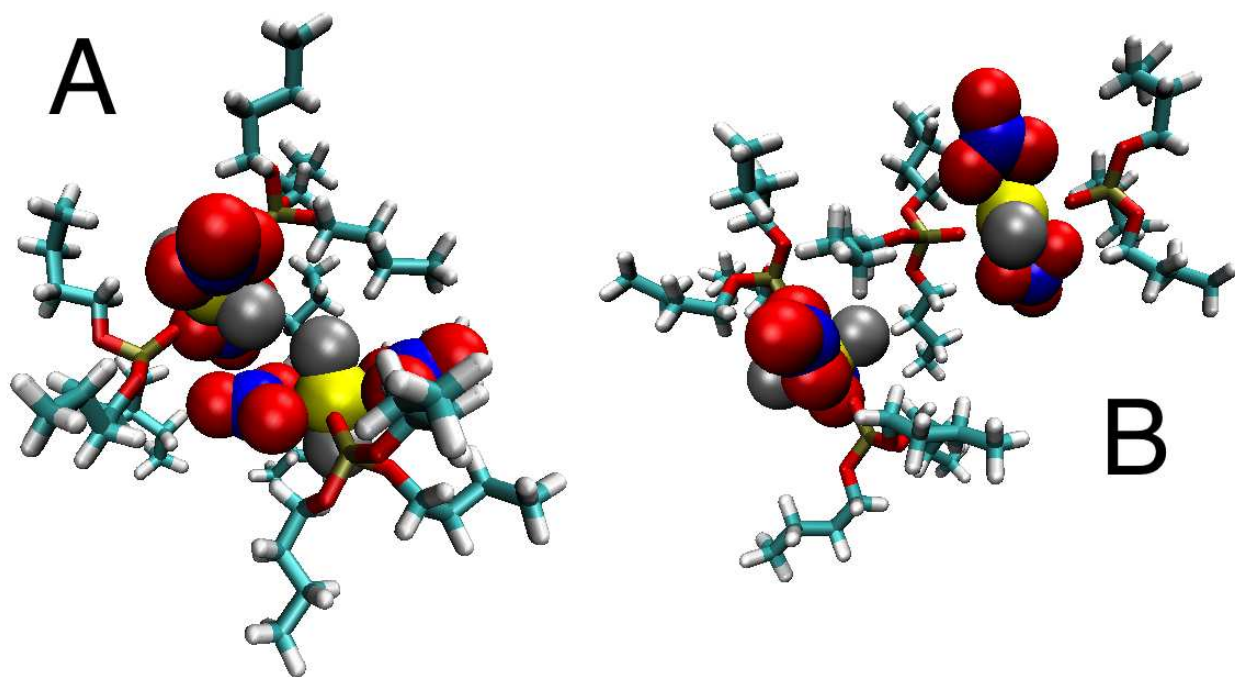


Figure 5.9: Snapshots of associating $\text{UO}_2\text{-(NO}_3)_2\text{-(TBP)}_2$ clusters, with snapshot A showing corresponding to the peak at 5-6Å, and snapshot B to the region at 10-12Å.

CHAPTER 6

CONCLUSIONS AND FUTURE DIRECTIONS

6.1 Summary and Conclusions

Molecular dynamics potentials developed in the literature for TBP were evaluated for accurate replication of self-association in aliphatic solvents. Reduction of the phosphate head group charges, chosen to improve agreement with experiment for the simulation average molecular dipole, density and self-diffusion coefficient, were found to significantly reduce self-association in *n*-dodecane and *n*-octane. An alternative model, using GAFF, was developed and implemented with modifications to the phosphorus-containing dihedrals to allow for replication of the dimerization constant without significant overprediction of the dipole and density. This reparameterization was applied to other solvating organophosphorus extractants, DBBP, TAP and DAAP. Further optimization of the alkyl carbon atom Lennard-Jones parameters to match the experimental density and enthalpy of vaporization was conducted for the four extractants. The TBP extractant model was shown to replicate the volume change on mixing and enthalpy of mixing with *n*-dodecane and *n*-hexane. These potentials are intended to be applicable to studying third phase formation in those aliphatic diluents where solubility of TBP clusters impacts phase behavior.

After developing the extractant models, organic phase speciation of extracted clusters was investigated. Formation of hydrogen bonded clusters of nitric acid and water extracted by TBP into *n*-dodecane were characterized with network analysis. The populations of the different hydrogen bond types forming the clusters were found to be consistent with an equilibrium binding constant model. For high extracted acid and water concentrations corresponding to conditions of third phase formation, the cluster size distribution was measured and found to be consistent with a percolation transition. Finally, extracted uranyl nitrate clusters were simulated for TBP, TAP and DBBP. A constrained uranyl nitrate model was

implemented with the uranyl-TBP parameters fit to quantum mechanical data. Extractant molecule structural differences were found to impact uranyl-centered cluster association. The phosphonate head group of DBBP reduced close coordination of the clusters. The increase in alkyl tail length for TAP from TBP reduced the correlation peak at the further 1 nm correlation distance.

6.2 Third Phase Formation with Water and Inorganic Acids

Third phase formation for TBP extraction of acid and water is observed at lower aqueous phase acid concentrations for other inorganic acids than nitric acid, such as hydrochloric acid, phosphoric acid, sulfuric acid and perchloric acid[21]. The relative propensity of those acids to form a third phase has not been successfully correlated to any physiochemical properties of these acids[21, 29]. The growth of clusters for TBP extraction of water and these acids, including nitric acid, has been studied with SANS using a model of spherical “reverse micelles” modeled associating through their polar cores with the Baxter potential until they are sufficiently concentrated as to exceed the solubility limit. The simulations presented here of nitric acid and water extraction have shown the clusters and percolation phase transition are not consistent with the Baxter particle scattering model where discrete clusters coalesce until they are no longer soluble. Rather, a system-spanning cluster resulting from percolation of the hydrogen bonded networks is identified as the phase transition mechanism. While it is possible that third phase formation in nitric acid/water extraction system is entirely different than for the other acids, it is also possible that the hydrogen bonding network percolation approach describes the phase transition for these other acids as well. It may then be applied to understand the as yet not understood relationship between acid type and acid LOC. For other extractants, such as TODGA or CMPO, third phase formation in the presence of just acid and water is an even more significant issue. An understanding of the phase transition mechanism and the role that acid functionality plays in the phase transition could aid extraction system design.

The cluster size distribution near the percolation threshold from MD was compared with MC lattice calculations to show that the large cluster formation was a result of the finite size effects of the simulation box on the formation of a system-spanning cluster, as expected in a percolation model, rather than formation of a large “reverse micelle” structures as described in the literature. Further simulations with an increased simulation box size showed that the large clusters of the cluster size distribution scaled with the box size, further indicating that those large clusters are a result of finite size effects and not the result of reverse micelle formation. The similarity in cluster distribution statistics between continuum MD simulation and lattice bond percolation supports the hypothesis that the percolation mechanism is shared. Geiger and Stanley[136] showed that similar properties dependent on critical exponents, such as the Fisher exponent for the cluster size distribution at the percolation threshold, between a continuum MD simulation and a 3D lattice MC calculation indicate that lattice methods can be applied to model the critical behavior of continuum systems. Therefore, a lattice MC approach could be applied to study the third phase transition if it is described by a percolation transition.

In Figure 6.1, the cluster size distributions from the MD simulations (panel A) in Chapter 4 are compared to MC distributions for bond percolation on a 2 dimensional square lattice (panel B) and a 3 dimensional cubic lattice (panel C) for a range of bond probabilities, p_B . The finite MC lattices, 15^2 for the square lattice described in Chapter 4 and 6^3 for the cubic lattice with 100,000 MC iterations are compared to the theoretical cluster size distributions calculated from the Fisher exponent for the corresponding square or cubic infinite lattice. Lattice sizes were chosen to maintain a comparable total number of vertices to the MD simulation. The similarity in cluster size distribution between the lattices and MD simulation for the cluster size distribution and the applicability of the Fisher exponent to the percolation threshold distribution indicate that prediction of the interacting continuum particle cluster distribution can be approximated using MC lattice calculations. In order to translate the hydrogen bond formation to lattice bond percolation, the bonding probabilities

for the hydrogen bond types need to be established. The bonding probabilities could be determined from the equilibrium binding model shown to reasonably describe the hydrogen bonding populations in Chapter 4.

A different approach than the lattice MC bond percolation is the mean field gelation theory described by Flory for polymer systems[116]. While the lattice bond percolation model explicitly accounts for “looping” within a cluster, where bond formation within a cluster is allowed thus reducing the total cluster sizes for a given set of bond formation probabilities, the mean field approach treats the solutes as vertices on a Cayley lattice where looping is not possible. Both approaches still assume bond formation probabilities for a given vertex are independent of the existence of bonds already formed on that vertex. While the mean field approach is less accurate for the hydrogen bond percolation application where looping is expected, it is a less computationally expensive method for calculating the percolation threshold. A matrix is used to define the expected number of connections through hydrogen bonding for a given solute type to another given solute type in the system. The expected number of connections depends on the hydrogen bond strengths, solute concentrations and the functionality of each solute. The eigenvalue of that matrix determines if the cluster size diverges while following the connectivity of solutes connected to the arbitrary starting solute, i.e., the cluster becomes “infinite” in size. The eigenvalue threshold for a percolated system would have to be determined for different systems with specific vertex functionalities.

In both modeling approaches above, simulation data are required to calculate the equilibrium binding constants that determine the hydrogen bond formation probabilities. Two major hurdles in simulating the other acids types need to be addressed before those extraction systems could be tested for a percolation phase transition. First is a limitation in understanding the protonation states of the inorganic acids. While nitric acid is generally in its associated form when extracted by TBP, the other acids generally are at least singly deprotonated. The exact protonation state is not well established and could play a significant role in hydrogen bond network formation. The second challenge is associated with imple-

mentation of molecular dynamics simulations. Even if the protonation was well established for the organic phase system approaching the LOC, MD potentials do not exist for sulfuric, phosphoric or (singly protonated) perchloric acid. Therefore, determining bonding probabilities from MD potentials is only readily possible for nitric acid extraction. Approaching third phase formation with the theoretical descriptions described about would first require first characterizing the protonation of multiprotic acids in the organic phase at the acid LOC. Second, MD potentials for the acid models require development. The equilibrium binding model described in Chapter 4 could then be implemented to calculate the hydrogen bonding probabilities for each hydrogen bond type. Those probabilities could then be implemented in lattice MC calculations to measure properties such as the cluster size distribution and investigate the impact of acid functionality and the probabilities for specific hydrogen bond types.

6.3 Third Phase Formation in Metal Ion Extraction

The lack of evidence for differences between long range ordering of TBP, DBBP and TAP clusters in the present simulations suggests that larger simulation box sizes and/or longer simulation times may be required to observe the phase transition. The next objective for this research should be to attempt to identify long-range ordering by considering larger and longer simulations and compare any resulting long-range ordering between extractants to predict which extractants result in phase separation. Calculation of x-ray or neutron scattering profiles for the simulation data could be used for comparison to experimental data and validation of the association observed in simulation.

The most significant challenge to simulating the metal clusters in the organic phase is accurately modeling the metal ions with MD potentials. Polarizable force fields could better account for the effects of metal ions on its coordination environment, although they would increase the already restrictive simulation times. A better understanding of the simulation box size and time scale limitations confronting the simulation approach would inform whether polarizable force fields are a tractable approach. Comparison between polarizable

and non-polarizable force fields would be straightforward and could be oriented towards identifying differences between $\text{UO}_2\text{-(NO}_3)_2\text{-(Extractant)}_2$ cluster association that may result from polarization of ligand coordinating the uranyl. While polarizable force fields have been employed to model TBP in the literature, there has not been extensive validation of those potentials for properties relating to self-association and mixed phase energetics as performed for the nonpolarizable modified GAFF extractant model discussed in previous chapter.

Solvent type, either different aliphatic diluent chain lengths and branching or entirely different organic solvents like those discussed in Chapter 3, have a significant impact on third phase formation and likely, therefore, uranyl cluster association. The impact of aliphatic solvent structure or other non-aliphatic solvent types on third phase formation could be readily observed if a signature of long-range ordering corresponding to phase separation is identified. While scattering data available for comparison is limited for solvents other than *n*-dodecane, the LOC identified in simulation could easily be tested without requiring scattering beamtime. In the same manner that the impact of the structural differences between extractants was linked to differences in cluster association in Chapter 5, the changes to cluster association resulting from changes to the solvent structure or chemical functionality could be investigated.

Temperature, extractant structure and concentration, acid type and acid concentration are known to impact the LOC for a given metal type. These variables could be investigated using the methodology discussed in Chapter 5. Simulation of acids other than nitric acid will require development of MD potentials as discussed above. Investigation of temperature and acid concentration would be a simple extension of the approach discussed in Chapter 5. While the coordination of uranyl is well established and largely static across metal ion concentrations, for multi-coordinate extractant extraction of trivalent lanthanides, metal coordination depends strongly on concentrations of coextracted acid and water that hydrogen bonding with the multi-metal clusters[22]. For those systems, the hydrogen bonding network

analysis discussed in Chapter 3 could be expanded to include metal coordination in the molecular connectivity defining clusters to understand how the clusters grow with increasing metal or acid concentrations.

Tetravalent metal ions like thorium and plutonium form third phases more readily than hexavalent uranium and are therefore also of interest to understand third phase formation. Examination of those metals in simulation would be a further challenge as the increased charge density would exacerbate the limitations of classical potentials. The effect of metal cluster concentration and all of the other variables discussed above on solubility of the metal clusters, and therefore the energetics governing the extraction process, could be systematically studied with simulation to form predictive models for metal distribution.

Achieving maximum utility from solvent extraction processes will require predictive modeling with atomistic resolution. While the challenges are numerous, with improved simulation capability, a network interpretation of extracted clusters could be applied to understand third phase formation for a many extraction systems. This approach could also be implemented to address other poorly understood extraction phenomena, including coextraction of different metals and extractant synergism.

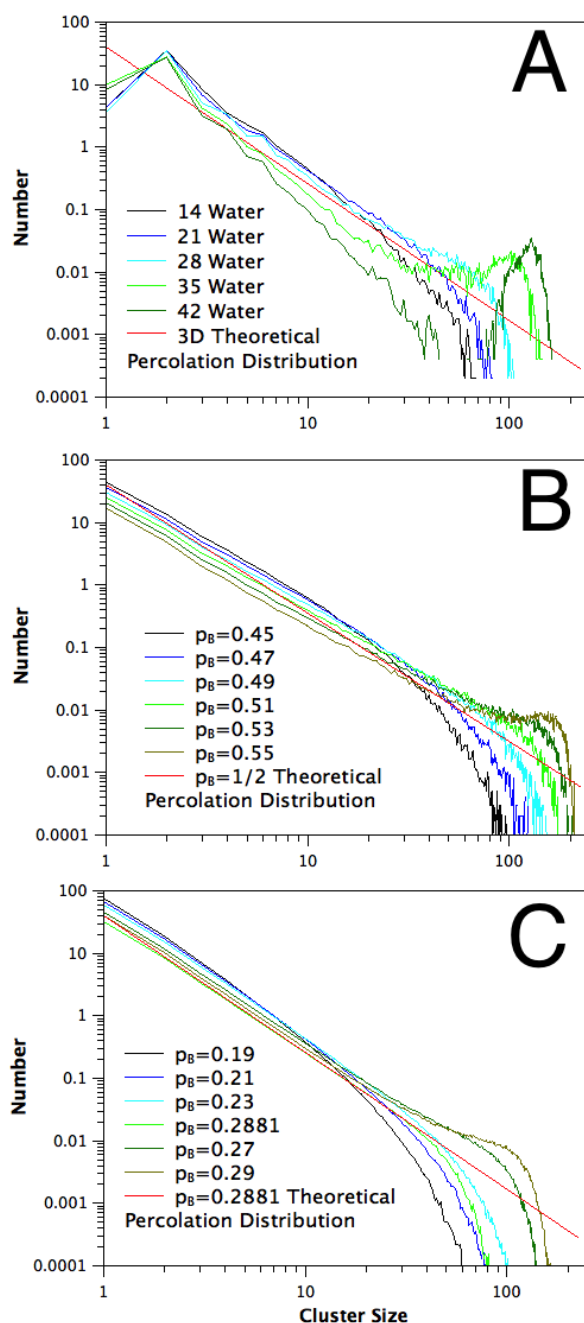


Figure 6.1: The cluster size distributions calculated from MD simulation of nitric acid and water extracted by TBP near the percolation threshold, compared with MC calculated lattice bond percolation cluster size distributions from 2 and 3 dimensional square and cubic lattices over a range of bond formation probabilities p_B around the percolation threshold probability. The theoretical percolation threshold cluster size distribution for 2D and 3D square lattices are overlaid with a red line. The MD data is compared to the 3D theoretical lattice percolation threshold distribution.

REFERENCES CITED

- [1] J Tollefson. Extraction of Uranium (VI) from Nitric Acid and Nitrate Solutions by Tributylphosphate/Kerosene. *Nature*, 507(7490):15–16, 2014.
- [2] K Nash and G Choppin. Separations Chemistry for Actinide Elements : Recent Developments and Historical Perspective. *Separation Science and Technology*, 34(1-4): 255–274, 2016.
- [3] A Kertes. The Chemistry of the Formation and Elimination of a Third Phase in Organophosphorus and Amine Extraction Systems. In *Proceeding of the International Conference sponsored by the United Kingdom Atomic Energy Authority*, pages 377–400, 1965.
- [4] P Rao and Z Kolarik. A Review of Third Phase Formation in Extraction of Actinides by Neutral Organophosphorus Extractants. *Solvent Extraction and Ion Exchange*, 14 (6):955–993, 1996.
- [5] F Testard, P Bauduin, T Zemb, and L Berthon. *Third Phase Formation in Liquid/Liquid Extraction: A Colloidal Approach*. CRC Press, 2010.
- [6] R Jha, K Gupta, P Kulkarni, P Gurba, P Janardan, R Changarani, P Dey, P Pathak, and V Manchanda. Third Phase Formation Studies in the Extraction of Th(IV) and U(VI) by N,N-dialkyl Aliphatic Amides. *Desalination*, 232(1-3):225–233, 2008.
- [7] M Jensen, R Chiarizia, J Ferraro, M Borkowski, K Nash, P Thiyagarajan, and K Littrell. New Insights in Third Phase Formation in the U(VI)-HNO₃, TBP-Alkane System. In *International Solvent Extraction Conference*, 2002.
- [8] N Kumari, D Prabhu, P Pathak, A Kanekar, and V Manchanda. Extraction Studies of Uranium into a Third-Phase of Thorium Nitrate Employing Tributyl Phosphate and N,N-dihexyl Octanamide as Extractants in Different Diluents. *Journal of Radioanalytical and Nuclear Chemistry*, 289(3):835–843, 2011.
- [9] J Plaue, A Gelis, and K Czerwinski. Actinide Third Phase Formation in 1.1 M TBP/Nitric Acid/Alkane Diluent Systems. *Separation Science and Technology*, 41(10):2065–2074, 2006.
- [10] R Chiarizia, M Jensen, M Borkowski, J Ferraro, P Thiyagarajan, and K Littrell. Third Phase Formation Revisited: The U(VI), HNO₃, TBP, n-Dodecane System. *Solvent Extraction and Ion Exchange*, 21(1):1–27, 2003.

- [11] M Borkowski, J Ferraro, R Chiarizia, and D McAlister. FT-IR Study of Third Phase Formation in the U(VI) or Th(IV)/HNO₃, TBP/Alkane Systems. *Solvent Extraction and Ion Exchange*, 20(3):313–330, 2002.
- [12] M Bera, R Ellis, B Burton-Pye, and M Antonio. Structural Aspects of Heteropolyacid Microemulsions. *Physical Chemistry and Chemical Physics*, 16(41):22566–22574, 2014.
- [13] M Bera, B Qiao, S Seifert, B Burton-Pye, M Olvera de la Cruz, and M Antonio. Aggregation of Heteropolyanions in Aqueous Solutions Exhibiting Short-Range Attractions and Long-Range Repulsions. *The Journal of Physical Chemistry C*, 120(2):1317–1327, 2016.
- [14] L Berthon and L Martinet. Solvent Penetration and Sterical Stabilization of Reverse Aggregates based on the DIAMEX Process Extracting Molecules: Consequences for the Third Phase Formation. *Solvent Extraction and Ion Exchange*, 25:545–576, 2007.
- [15] M Borkowski, R Chiarizia, M Jensen, J Ferraro, P Thiyagarajan, and K Littrell. SANS Study of Third Phase Formation in the Th(IV)-HNO₃/TBP-n-Octane System. *Separation Science and Technology*, 38(12-13):3333–3351, 2003.
- [16] R Chiarizia, P Thiyagarajan, M Jensen, M Borkowski, and K Littrell. Third Phase Formation in TBP Solvent Extraction Systems as a Result of Interaction Between Reverse Micelles. In *Hydrometallurgy*, volume 1, pages 917–928, 2003.
- [17] R Chiarizia, M Jensen, M Borkowski, J Ferraro, P Thiyagarajan, and K Littrell. SANS Study of Third Phase Formation in the U(VI)-HNO₃/TBP/n-Dodecane System. *Separation Science and Technology*, 38(12-13):3313–3331, 2003.
- [18] R Chiarizia, M Jensen, M Borkowski, P Thiyagarajan, and K Littrell. Interpretation of Third Phase Formation in the Th(IV) HNO₃, TBP n-Octane System with Baxter’s Sticky Spheres Model. *Solvent Extraction and Ion Exchange*, 22(3):325–351, 2004.
- [19] R Chiarizia, M Jensen, P Rickert, Z Kolarik, M Borkowski, and P Thiyagarajan. Extraction of Zirconium Nitrate by TBP in n-Octane: Influence of Cation Type on Third Phase Formation According to the ”Sticky Spheres” Model. *Langmuir*, 20(25):10798–10808, 2004.
- [20] R Chiarizia, D Stepinski, and P Thiyagarajan. SANS Study of Third Phase Formation in the Extraction of HCl by TBP Isomers in n-Octane. *Separation Science and Technology*, 41:2075–2095, 2006.
- [21] R Chiarizia and A Briand. Third Phase Formation in the Extraction of Inorganic Acids by TBP in n-Octane. *Solvent Extraction and Ion Exchange*, 25(3):351–371, 2007.

- [22] R Ellis, Y Meridiano, J Muller, L Berthon, P Guilbaud, N Zorz, M Antonio, T Demars, and T Zemb. Complexation-Induced Supramolecular Assembly Drives Metal-Ion Extraction. *Chemistry: A European Journal*, 20(40):12796–12807, 2014.
- [23] S Nave, C Mandin, L Martinet, L Berthon, F Testard, C Madic, and T Zemb. Supramolecular Organisation of Tri-n-butyl Phosphate in Organic Diluent on Approaching Third Phase Transition. *Physical Chemistry Chemical Physics*, 6:799–808, 2004.
- [24] J Plaue, A Gelis, K Czerwinski, P Thiyagarajan, and R Chiarizia. Small Angle Neutron Scattering Study of Plutonium Third Phase Formation in 30% TBP/HNO₃/Alkane Diluent Systems. *Solvent Extraction and Ion Exchange*, 24(3):283–298, 2006.
- [25] P Verma, P Pathak, P Mohapatra, V Aswal, B Sadhu, and M Sundararajan. An Insight into Third-Phase Formation During the Extraction of Thorium Nitrate: Evidence for Aggregate Formation from Small-Angle Neutron Scattering and Validation by Computational Studies. *Journal of Physical Chemistry B*, 117(33):9821–9828, 2013.
- [26] R Chiarizia, D Stepinski, and M Antonio. SANS Study of HCl Extraction by Selected Neutral Organophosphorus Compounds in n-Octane. *Separation Science and Technology*, 45(12-13):1668–1678, 2010.
- [27] R Chiarizia, K Nash, M Jensen, P Thiyagarajan, and K Littrell. Application of the Baxter Model for Hard Spheres with Surface Adhesion to SANS Data for the U(VI)-HNO₃, TBP-n-Dodecane System. *Langmuir*, 19:9592–9599, 2003.
- [28] J Ferraro, M Borkowski, R Chiarizia, and D McAlister. FT-IR Spectroscopy of Nitric Acid in TBP/Octane Solution. *Solvent Extraction and Ion Exchange*, 19(6):981–992, 2001.
- [29] R Chiarizia, A Briand, M Jensen, and P Thiyagarajan. SANS Study of Reverse Micelles Formed upon the Extraction of Inorganic Acids by TBP in n-Octane. *Solvent Extraction and Ion Exchange*, 26:333–359, 2008.
- [30] P Rao, R Dhamodaran, T Srinivasan, and C Mathews. The Effect of Diluent on Third Phase Formation in Thorium Nitrate-TBP System: Some Novel Empirical Correlations. *Solvent Extraction and Ion Exchange*, 11(4):645–662, 1993.
- [31] C Rao, T Srinivasan, and P Rao. Studies on the Extraction of Actinides by Dibutyl-butyl Phosphonate. *Solvent Extraction and Ion Exchange*, 28:202–224, 2010.
- [32] J Wang, M Romain, J Caldwell, P Kollman, and D Case. Development and Testing of a General AMBER Force Field. *Journal of Computational Chemistry*, 25(19):1157–1174, 2004.

- [33] D Frenkel and B Smit. *Understanding Molecular Simulation Second Edition*. Academic Press, San Diego, 2002.
- [34] P Beudaert, V Lamare, J Dozol, L Troxler, and G Wipff. Theoretical Studies on Tri-n-butyl Phosphate: MD Simulations in Vacuo, in Water, in Chloroform, and at a Water/Chloroform Interface. *Solvent Extraction and Ion Exchange*, 16:597–618, 1998.
- [35] M Baaden, M Burgard, and G Wipff. TBP at the Water-Oil Interface: The Effect of TBP Concentration and Water Acidity Investigated by Molecular Dynamics Simulations. *Journal of Physical Chemistry B*, 105:11131–11141, 2001.
- [36] M Baaden, R Schurhammer, and G Wipff. Molecular Dynamics Study of the Uranyl Extraction by Tri-n-butylphosphate (TBP): Demixing of Water/Oil/TBP Solutions with a Comparison of Supercritical CO₂ and Chloroform. *Journal of Physical Chemistry B*, 106:434–441, 2002.
- [37] R Schurhammer and G Wipff. Effect of the TBP and Water on the Complexation of Uranyl Nitrate and the Dissolution of Nitric Acid into Supercritical CO₂: A Theoretical Study. *The Journal of Physical Chemistry A*, 109(23):5208–5216, 2005.
- [38] M Baaden, F Berny, and G Wipff. The Chloroform/TBP/Aqueous Nitric Acid Interfacial System: a Molecular Dynamics Investigation. *Journal of Molecular Liquids*, 90:1–9, 2001.
- [39] G Benay and G Wipff. Liquid-Liquid Extraction of Uranyl by TBP: The TBP and Ions Models and Related Interfacial Features Revisited by MD and PMF Simulations. *Journal of Physical Chemistry B*, 118(11):3133–3149, 2014.
- [40] G Benay and G Wipff. Liquid-Liquid Extraction of Uranyl by an Amide Ligand: Interfacial Features Studied by MD and PMF Simulations. *Journal of Physical Chemistry B*, 117(24):7399–7415, 2013.
- [41] G Benay and G Wipff. Liquid-Liquid Extraction of Alkali Cations by 18-Crown-6: Complexation and Interface Crossing Studied by MD and PMF Simulations. *New Journal of Chemistry*, 40:2102–2114, 2016.
- [42] P Kujawski and M Bogacki. Molecular Dynamics Study of the Behaviour of TBP-Zinc-Chloride Complex at the Chloroform/Water Interfacial System. *Separation Science and Technology*, 47(9):1285–1295, 2012.
- [43] P Sahu, S Ali, and K Shenoy. The Passage of Charged TBP-Uranyl Complexes from Aqueous-Organic Interface to the Organic Phase: Insights from Molecular Dynamics Simulation. *Physical Chemistry and Chemical Physics*, 18:23769–23784, 2016.

- [44] P Sahu, S Ali, and K Shenoy. TBP Assisted Uranyl Extraction in Water-Dodecane Biphasic System: Insights from Molecular Dynamics Simulation. *Chemical Product and Process Modeling*, 2017.
- [45] H Zheng, F Wu, B Wang, and Y Wu. Molecular Dynamics Simulation on the Interfacial Features of Phenol Extraction by TBP/Dodecane in Water. *Computational and Theoretical Chemistry*, 970(1-3):66–72, 2011.
- [46] M Jayasinghe and T Beck. Molecular Dynamics Simulations of the Structure and Thermodynamics of Carrier-Assisted Uranyl Ion Extraction. *The Journal of Physical Chemistry B*, 113(34):11662–11671, 2009.
- [47] D Case, T Cheatham, T Darden, H Gohlke, R Luo, K Merz, A Onufriev, C Simmerling, B Wang, and R Woods. The Amber Biomolecular Simulation Programs. *Journal of Computational Chemistry*, 26:1668–1688, 2005.
- [48] B Brooks, R Bruccoleri, B Olafson, D States, S Swaminathan, and M Karplus. CHARMM: A Program for Macromolecular Energy, Minimization, and Dynamics Calculations. *Journal of Computational Chemistry*, 4:187–217, 1983.
- [49] W Jorgensen and J Tirado-Rives. The OPLS Potential Functions for Proteins. Energy Minimizations for Crystals of Cyclic Peptides and Crambin. *Journal of the American Chemical Society*, 110(6):1657–1666, 2003.
- [50] S Cui, V de Almeida, B Hay, X Ye, and B Khomami. Molecular Dynamics Simulation of Tri-n-butyl-phosphate Liquid: A Force Field Comparative Study. *The Journal of Physical Chemistry B*, 116(1):305–313, 2012.
- [51] X Ye, S Cui, V de Almeida, and B Khomami. Effect of Varying the 1-4 Intramolecular Scaling Factor in Atomistic Simulations of Long-Chain n-Alkanes with the OPLS-AA Model. *Journal of Molecular Modeling*, 19(3):1251–1258, 2013.
- [52] X Ye, S Cui, V de Almeida, and B Khomami. Molecular Simulation of Water Extraction into a Tri-n-butylphosphate/n-Dodecane Solution. *The Journal of Physical Chemistry B*, 117(47):14835–14841, 2013.
- [53] S Cui, V de Almeida, and B Khomami. Molecular Dynamics Simulations of Tri-n-butyl-phosphate/n-Dodecane Mixture: Thermophysical Properties and Molecular Structure. *The Journal of Physical Chemistry B*, 118(36):10750–10760, 2014.
- [54] L Leay, K Tucker, A Del Regno, S Schroeder, C Sharrad, and A Masters. The Behaviour of Tributyl Phosphate in an Organic Diluent. *Molecular Physics*, 112(17):2203–2214, 2014.

- [55] P Ivanov, J Mu, L Leay, C Sharrad, and A Masters. The Organic and the Third Phase in the System $\text{HNO}_3/\text{TBP}/\text{n-Dodecane}$: No Reverse Micelles. *Solvent Extraction and Ion Exchange*, 2017.
- [56] J Mu, R Motokawa, C Williams, K Akutsu, S Nishitsuji, and A Masters. Comparative Molecular Dynamics Study on Tri-n-butyl Phosphate in Organic and Aqueous Environments and Its Relevance to Nuclear Extraction Processes. *The Journal of Physical Chemistry B*, 120(23):5183–5193, 2016.
- [57] A Mondal and S Balasubramanian. Intermolecular Structure in Tri-n-butyl Phosphate/n-Octane Mixtures: A Molecular Dynamics Simulation Study. *Computational Chemistry and Molecular Simulation*, 106(9):1235–1242, 2014.
- [58] Q Vo, C Hawkins, L Dang, M Nilsson, and H Nguyen. A Computational Study of Molecular Structure and Self-Association of Tri-n-butyl Phosphates in n-Dodecane Diluent. *The Journal of Physical Chemistry B*, 119:1588–1597, 2015.
- [59] Q Vo, L Dang, M Nilsson, and H Nguyen. Quantifying Dimer and Trimer Formation by Tri-n-butyl Phosphates in n-Dodecane: Molecular Dynamics Simulations. *The Journal of Physical Chemistry B*, 120:6985–6994, 2016.
- [60] Q Vo, J Unangst, H Nguyen, and M Nilsson. Quantifying Dimer and Trimer Formation by Tri-n-butyl Phosphates in Different Alkane Diluents: FTIR Study. *The Journal of Physical Chemistry B*, 120:6976–6984, 2016.
- [61] F Hutschka, A Dedieu, L Troxler, and G Wipff. Theoretical Studies on the UO_2^{2+} and Sr^{2+} Complexation by Phosphoryl-Containing $\text{O}=\text{PR}_3$ Ligands: QM ab Initio Calculations in the Gas Phase and MD FEP Calculations in Aqueous Solution. *Journal of Physical Chemistry A*, 102:3773–3781, 1998.
- [62] C Boehme and G Wipff. The Energetic and Structural Effects of Steric Crowding in Phosphate and Dithiophosphinate Complexes of Lanthanide Cations M^{3+} : A Computational Study. *Chemistry: A European Journal*, 7(7):1398–407, 2001.
- [63] Michael Bühl, Romain Diss, and Georges Wipff. Coordination Environment of Aqueous Uranyl (VI) Ion. *Journal of the American Chemical Society Communications*, 127:13506–13507, 2005.
- [64] M Bühl, H Kabrede, R Diss, and G Wipff. Effect of Hydration on Coordination Properties of Uranyl(VI) Complexes. A First-Principles Molecular Dynamics Study. *Journal of the American Chemical Society*, 128(19):6357–6368, 2006.
- [65] M Bühl, R Diss, and G Wipff. Coordination Mode of Nitrate in Uranyl (VI) Complexes: A First-Principles Molecular Dynamics Study. *Inorganic Chemistry*, 46(13):5196–5206, 2007.

- [66] R Frick, A Pribil, T Hofer, B Randolph, A Bhattacharjee, and B Rode. Structure and Dynamics of the U^{4+} Ion in Aqueous Solution: An ab Initio Quantum Mechanical Charge Field Molecular Dynamics Study. *Inorganic Chemistry*, 48(9):3993–4002, 2009.
- [67] P Guilbaud and G Wipff. Hydration of UO_2^{2+} Cation and Its NO_3^- and 18-Crown-6 Adducts Studied by Molecular Dynamics Simulations. *Journal of Physical Chemistry*, 97:5685–5692, 1993.
- [68] P Guilbaud and G Wipff. Force Field Representation of the UO_2^{2+} Cation from Free Energy MD Simulations in Water. Tests on its 18-crown-6 and NO_3^- Adducts, and on its Calix[6]arene⁶⁻ and CMPO Complexes. *Journal of Molecular Structure*, 366:55–63, 1996.
- [69] D Hagberg, G Karlström, B Roos, and L Gagliardi. The Coordination of Uranyl in Water: a Combined Quantum Chemical and Molecular Simulation Study. *Journal of the American Chemical Society*, 127(41):14250–14256, 2005.
- [70] S Pérez-Conesa, F Torrico, J Martínez, R Pappalardo, and E Sánchez Marcos. A Hydrated Ion Model of UO_2^{2+} in Water: Structure, Dynamics, and Spectroscopy from Classical Molecular Dynamics. *The Journal of Chemical Physics*, 145(22):224502, 2016.
- [71] R Spezia, C Beuchat, R Vuilleumier, P D’Angelo, and L Gagliardi. Unravelling the Hydration Structure of ThX_4 ($X = Br, Cl$) Water Solutions by Molecular Dynamics Simulations and X-ray Absorption Spectroscopy. *Journal of Physical Chemistry B*, 116:6465–6475, 2012.
- [72] G Wipff, P Weiner, and P Kollman. A Molecular Mechanics Study of 18-Crown-6 and Its Alkali Complexes: An Analysis of Structural Flexibility, Ligand Specificity, and the Macrocyclic Effect. *Journal of the American Chemical Society*, 104(12):3249–3258, 1982.
- [73] J Zhou and H Schlegel. Ab Initio Molecular Dynamics Study of the Reaction between Th^+ and H_2O . *The Journal of Physical Chemistry A*, 114:8613–8617, 2010.
- [74] X Ye, R Smith, S Cui, V de Almeida, and B Khomami. Influence of Nitric Acid on Uranyl Nitrate Association in Aqueous Solutions: A Molecular Dynamics Simulation Study. *Solvent Extraction and Ion Exchange*, 28(1):1–18, 2010.
- [75] S Kerisit and C Liu. Structure, Kinetics, and Thermodynamics of the Aqueous Uranyl(VI) Cation. *Journal of Physical Chemistry A*, 118:6421–6432, 2014.
- [76] L Dang, Q Vo, M Nilsson, and H Nguyen. Rate Theory on Water Exchange in Aqueous Uranyl Ion. *Chemical Physics Letters*, 671:58–62, 2017.

- [77] X Ye, S Cui, V de Almeida, and B Khomami. Interfacial Complex Formation in Uranyl Extraction by Tributyl Phosphate in Dodecane Diluent: A Molecular Dynamics Study. *The Journal of Physical Chemistry B*, 113(29):9852–9862, 2009.
- [78] M Antonio, R Ellis, S Estes, and M Bera. Structural Insights into the Multinuclear Speciation of Tetravalent Cerium in the Tri-*n*-butyl Phosphate-*n*-Dodecane Solvent Extraction System. *Physical Chemistry and Chemical Physics*, 2017.
- [79] K Nash and J Braley. Challenges for Actinide Separations in Advanced Nuclear Fuel Cycles. *ACS Symposium Series*, 1046:19–38, 2010.
- [80] J McKibben. Chemistry of the Purex Process. *Radiochimica Acta*, 36:3–15, 1984.
- [81] D Campbell and W Burch. The Chemistry of Fuel Reprocessing: Present Practices, Future Trends. *Journal of Radioanalytical and Nuclear Chemistry*, 142(1):303–320, 1990.
- [82] D Sood and S Patil. Chemistry of Nuclear Fuel Reprocessing: Current Status. *Journal of Radioanalytical and Nuclear Chemistry*, 203(2):547–573, 1996.
- [83] X Ye, S Cui, V de Almeida, B Hay, and B Khomami. Uranyl Nitrate Complex Extraction into TBP/Dodecane Organic Solutions: A Molecular Dynamics Study. *Physical Chemistry and Chemical Physics*, 12(47):15406–15409, 2010.
- [84] A Ozkanlar and A Clark. ChemNetworks: A Complex Network Analysis Tool for Chemical Systems. *Journal of Computational Chemistry*, 35:495–505, 2014.
- [85] A Jakalian, B Bush, D Jack, and C Bayly. Fast, Efficient Generation of High-Quality Atomic Charges. AM1-BCC Model: I. Method. *Journal of Computational Chemistry*, 21(2):132–146, 1999.
- [86] A Jakalian, D Jack, and C Bayly. Fast, Efficient Generation of High-Quality Atomic Charges. AM1-BCC Model: II. Parameterization and Validation. *Journal of Computational Chemistry*, 23(16):1623–41, 2002.
- [87] J Stewart. *MOPAC2012*. Stewart Computational Chemistry, Colorado Springs, CO, 2012.
- [88] G te Velde, F Bickelhaupt, E Baerends, C Fonseca Guerra, S van Gisbergen, J Snijders, and T Ziegler. Chemistry with *adf*. *Journal of Computational Chemistry*, 22(9):931–967, 2001.

- [89] B. Hess, C. Kutzner, D. Spoel, and E. Lindhal. Gromacs 4: Algorithms for highly efficient, load balanced, and scalable molecular dynamics simulation. *Journal of Chemical Theory and Computation*, 4(3):435–447, 2008.
- [90] Q Tian and H Liu. Densities and Viscosities of Binary Mixtures of Tributyl Phosphate with Hexane and Dodecane from (298.15 to 328.15) K. *Journal of Chemical Engineering Data*, 52:892–897, 2007.
- [91] J Hurwic and J Michalczyk. Dielectric investigations of tributylphosphate and some of its systems. *Nukleonika*, 10:221, 1965.
- [92] G Estok and W Wendlandt. Electric Moments of Some Alkyl Phosphates and Thiophosphates. *Journal of the American Chemical Society*, 495(6):4767–4769, 1955.
- [93] D Petkovic, B Kezele, and D Rajic. Dipole Moments of Some Neutral Organic Phosphates. *Journal of Physical Chemistry*, 77(7):922–924, 1973.
- [94] G Vandegrift. Diluents for tbp extraction systems. In W Schulz, J Navratil, and A Kertes, editors, *Science and Technology of Tributyl Phosphate*, volume I, pages 69–136. CRC Press, Boca Raton, FL, 1984.
- [95] J Roddy. Distribution of Ethanol-Water Mixtures to Organic Liquids. *Industrial Engineering and Chemical Process Design and Development*, 20:104–108, 1981.
- [96] D Petkovic. Some Correlations of Trialkyl Phosphates Dimerization Constants. *Journal of Inorganic and Nuclear Chemistry*, 30:603–609, 1968.
- [97] R Ellis, M Audras, and M Antonio. Mesoscopic Aspects of Phase Transitions in a Solvent Extraction System. *Langmuir*, 28:15498–15504, 2012.
- [98] M Servis, C Tormey, D Wu, and J Braley. A Molecular Dynamics Study of Tributyl Phosphate and Diamyl Amyl Phosphonate Self-Aggregation in Dodecane and Octane. *The Journal of Physical Chemistry B*, 120(10):2796–2806, 2016.
- [99] M Servis, D Wu, and J Braley. Network Analysis and Percolation Transition in Hydrogen Bonded Clusters: Nitric Acid and Water Extracted by Tributyl Phosphate. *Physical Chemistry and Chemical Physics*, 19(18):11326–11339, 2017.
- [100] S Siu, K Pluhackova, and R Bo. Optimization of the OPLS-AA Force Field for Long Hydrocarbons. *Journal of Chemical Theory and Computation*, 8:1459–1470, 2012.
- [101] A Suresh, T Srinivasan, and P Rao. Extraction of U(VI), Pu(IV) and Th(IV) by some Trialkyl Phosphates. *Solvent Extraction and Ion Exchange*, 12:727–744, 1994.

- [102] W Acree and J Chickos. Phase transition enthalpy measurements of organic and organometallic compounds. In P Linstrom and W Mallard, editors, *NIST Chemistry WebBook, NIST Standard Reference Database Number 69*. National Institute of Standards and Technology, Gaithersburg, MD.
- [103] L Tsimering and A Kertes. Excess Enthalpies of Tri-*n*-butylphosphate + Hydrocarbons. *Journal of Chemical Thermodynamics*, 6:411–415, 1974.
- [104] R Motokawa, S Suzuki, H Ogawa, M Antonio, and T Yaita. Microscopic Structures of Tri-*n*-butyl Phosphate/*n*-Octane Mixtures by X-ray and Neutron Scattering in a Wide *q* Range. *Journal of Physical Chemistry B*, 116:1319–1327, 2012.
- [105] Jacob N. Israelachvili. *Intermolecular and Surface Forces*. Academic Press, San Diego, 3 edition, 2011.
- [106] R Singh and C Sinha. Dielectric Behavior of the Binary Mixtures of *n*-Hexane with Toluene, Chlorobenzene, and 1-Hexanol. *Journal of Chemical Engineering Data*, 27:283–287, 1982.
- [107] B Qiao, T Demars, M Olvera de la Cruz, and R Ellis. How Hydrogen Bonds Affect the Growth of Reverse Micelles Around Coordinating Metal Ions. *Journal of Physical Chemistry Letters*, 5:1440–1444, 2014.
- [108] J Braley, G Lumetta, and J Carter. Combining cmpo and heh[ehp] for separating trivalent lanthanides from the transuranic elements. *Solvent Extraction and Ion Exchange*, 31(6):567–577, 2013.
- [109] A Baldwin, Y Yang, N Bridges, and J Braley. Tributyl Phosphate Aggregation in the Presence of Metals: An Assessment Using Diffusion NMR Spectroscopy. *Journal of Physical Chemistry B*, 120(47):12184–12192, 2016.
- [110] H Wang, X Hong, F Gu, and X Ba. Statistical Theory for Hydrogen Bonding Fluid System of AaDd Type (I): The Geometrical Phase Transition. *Science in China, Series B: Chemistry*, 49(6):499–506, 2006.
- [111] M Girardi, V Henriques, and W Figueiredo. Amphiphilic Aggregation in Hydrogen Bonding Liquids: Dynamic and Equilibrium Properties. *Journal of Chemical Physics*, 328(1-3):139–146, 2006.
- [112] L Dougan, J Crain, J Finney, and A Soper. Molecular Self-Assembly in a Model Amphiphile System. *Physical Chemistry and Chemical Physics*, 12(35):10221–10229, 2010.

- [113] E Bianchi, P Tartaglia, E La Nave, and F Sciortino. Fully Solvable Equilibrium Self-Assembly Process: Fine-Tuning the Clusters Size and the Connectivity in Patchy Particle Systems. *Journal of Physical Chemistry B*, 111(40):11765–11769, 2007.
- [114] J Tavares, P Teixeira, M Telo Da Gama, and F Sciortino. Equilibrium Self-Assembly of Colloids with Distinct Interaction Sites: Thermodynamics, Percolation, and Cluster Distribution Functions. *Journal of Chemical Physics*, 132(23):234502–234513, 2010.
- [115] C Fu, Z Sun, and L An. Relationship Between Structural Gel and Mechanical Gel for ABA Triblock Copolymer in Solutions: A Molecular Dynamics Simulation. *Journal of Physical Chemistry B*, 115(39):11345–11351, 2011.
- [116] P. J. Flory. *Principles of Polymer Chemistry*. Cornell University Press, London, 1953.
- [117] H Passos, A Luis, J Coutinho, and M Freire. Thermoreversible (Ionic-Liquid-Based) Aqueous Biphasic Systems. *Scientific Reports*, 6, 2016.
- [118] B Mokili and C Poitrenaud. Modeling of Nitric Acid and Water Extraction From Aqueous Solutions Containing a Salting-Out Agent by Tri-n-butyl Phosphate. *Solvent Extraction and Ion Exchange*, 13(4):731–754, 1995.
- [119] C Dickson, L Rosso, R Betz, R Walker, and I Gould. GAFFlipid: A General Amber Force Field for the Accurate Molecular Dynamics Simulation of Phospholipid. *Soft Matter*, 8(37):9617–9627, 2012.
- [120] D Peppard and J Ferraro. An infra-red study of the systems tri-n-butyl phosphate-hno₃ and bis-(2-ethylhexyl)-phosphoric acid-hno₃. *Journal of Inorganic and Nuclear Chemistry*, 15:365–370, 1960.
- [121] A Alcock, S Grimley, T Healy, J Kennedy, and H McKay. The Extraction of Nitrates by Tri-n-butyl Phosphate (TBP) Part 1 – The System TBP + Diluent + H₂O + HNO₃. *Transactions Faraday Society*, pages 39–47, 1955.
- [122] J Zielkiewicz. Structural Properties of Water: Comparison of the SPC, SPCE, TIP4P, and TIP5P Models of Water. *Journal of Chemical Physics*, 123(10):104501, 2005.
- [123] P Burns and C Hanson. Distribution of Nitric Acid Between Tri-n-butyl Phosphate and Water. *Journal of Applied Chemistry*, 14:117–121, 1964.
- [124] W Davis, J Mrochek, and C Hardy. The System: Tri-n-butyl Phosphate (TBP)-Nitric Acid-Water. *Journal of Inorganic and Nuclear Chemistry*, 28:2001–2014, 1966.

- [125] M. J. Frisch, G. W. Trucks, H. B. Schlegel, G. E. Scuseria, M. A. Robb, J. R. Cheeseman, G. Scalmani, V. Barone, B. Mennucci, G. A. Petersson, H. Nakatsuji, M. Caricato, X. Li, H. P. Hratchian, A. F. Izmaylov, J. Bloino, G. Zheng, J. L. Sonnenberg, M. Hada, M. Ehara, K. Toyota, R. Fukuda, J. Hasegawa, M. Ishida, T. Nakajima, Y. Honda, O. Kitao, H. Nakai, T. Vreven, J. A. Montgomery, Jr., J. E. Peralta, F. Ogliaro, M. Bearpark, J. J. Heyd, E. Brothers, K. N. Kudin, V. N. Staroverov, R. Kobayashi, J. Normand, K. Raghavachari, A. Rendell, J. C. Burant, S. S. Iyengar, J. Tomasi, M. Cossi, N. Rega, J. M. Millam, M. Klene, J. E. Knox, J. B. Cross, V. Bakken, C. Adamo, J. Jaramillo, R. Gomperts, R. E. Stratmann, O. Yazyev, A. J. Austin, R. Cammi, C. Pomelli, J. W. Ochterski, R. L. Martin, K. Morokuma, V. G. Zakrzewski, G. A. Voth, P. Salvador, J. J. Dannenberg, S. Dapprich, A. D. Daniels, . Farkas, J. B. Foresman, J. V. Ortiz, J. Cioslowski, and D. J. Fox. Gaussian09 Revision E.01, 2009. Gaussian Inc. Wallingford CT 2009.
- [126] V Rassolov, M Ratner, J Pople, P Redfern, and L Curtiss. 6-31g* basis set for third-row atoms. *Journal of Computational Chemistry*, 22(9):976–984, 2001.
- [127] A Klamt. The cosmo and cosmo-rs solvation models. *Wiley Interdisciplinary Reviews: Computational Molecular Science*, 1(5):699–709, 2011.
- [128] E Stoyanov, V Mikhailov, A Chekmarev, and S Chizhevskaya. The Composition and Structure of the Associates of Nitric Acid Extracted from its Concentrated Aqueous Solutions by 100% Tributyl Phosphate. *Russian Journal of Inorganic Chemistry*, 35(6):821–826, 1990.
- [129] E Stoyanov, V Mikhailov, and A Chekmarev. The Chemistry of the Extraction of Nitric Acid by Tributyl Phosphate and Other Oxygen-Containing Extracting Agents. *Russian Journal of Inorganic Chemistry*, 37(11):1323–1329, 1992.
- [130] M Singh, S Nayak, A Kanthe, R Patil, and V Gaikar. Insight into Acidity Driven Third Phase Formation of TBP in Organic Solutions by MD Simulation. *Journal of Molecular Liquids*, 2017.
- [131] R Kendall, E Apra, D Bernholdt, E Bylaska, M Dupuis, G Fann, R Harrison, J Ju, J Nichols, J Nieplocha, and T Straatsma. High Performance Computational Chemistry: An Overview of NWChem a Distributed Parallel Application. *Computer Physics Communications*, 128:260–283, 2000.
- [132] W Kuechle, M Dolg, H Stoll, and H Preuss. Energy-Adjusted Pseudopotentials for the Actinides. Parameter Sets and Test Calculations for Thorium and Thorium Monoxide. *Journal of Chemical Physics*, 100(10):7535–7542, 1994.

- [133] L Martinez, R Andrade, E Birgin, and J Martinez. Packmol: A Package for Building Initial Configurations for Molecular Dynamics Simulations. *Journal of Computational Chemistry*, 30(13):2157–2164, 2009.
- [134] C Den Auwer, C Lecouteux, M Charbonnel, C Madic, and R Guillaumont. XAS Study of Actinide and Lanthanide Solvent Extraction Compounds–I. $\text{UO}_2(\text{NO}_3)_2(\text{TIBP})_2$ and $\text{UO}_2(\text{NO}_3)_2(\text{TBP})_2$ (with TIBP = Tri-Isobutylphosphate and TBP = Tributylphosphate). *Polyhedron*, 16(13):2233–2238, 1997.
- [135] B Waldher, J Kuta, S Chen, N Henson, and A Clark. ForceFit: A Code to Fit Classical Force Fields to Quantum Mechanical Potential Energy Surfaces. *Journal of Computational Chemistry*, 31:2307–2316, 2010.
- [136] A Geiger and H Stanley. Tests of Universality of Percolation Exponents for a Three-Dimensional Continuum System of Interacting Waterlike Particles. *Physical Review Letters*, 49:1895–1898, 1982.

APPENDIX
SUPPORTING INFORMATION FROM CHAPTER 4

The force field parameters used for the TBP and dodecane molecules are given in Tables Table A.1, Table A.2, Table A.3, Table A.4. Parameters which have been modified from the default GAFF values, as described in the main article, are denoted with an asterisk. Table Table A.5 gives the partial atomic charges used in the dodecane and TBP models.

Figure Figure A.1 show the RDFs used to determine the hydrogen bond definitions. Figures Figure A.2 and Figure A.3 plot less frequently occurring structures and substructures, respectively.

Table A.1: GAFF Lennard Jones parameters for the TBP and dodecane atom types.

Atom	σ [Å]	ϵ [kcal mol ⁻¹]
O2	2.9599	0.2100
P	3.7418	0.2000
OS	3.0000	0.1700
CT* (TBP)	3.2297	0.1127
CT* (dodecane)	3.1324	0.1444
H1	2.4714	0.0157
HC	2.6495	0.0157

Table A.2: GAFF equilibrium bond length and bond energy parameters.

Bond	l_0 [Å]	k_l [kcal mol ⁻¹ Å ⁻²]
O2-P	1.481	487.7
P-OS	1.602	342.5
P-CT	1.813	259.7
OS-CT	1.439	301.5
CT-CT	1.535	303.1
CT-H1	1.093	335.9
CT-HC	1.092	337.3

Table A.3: GAFF equilibrium angle and angle energy parameters.

Angle	θ_0 [deg]	k_θ [kcal mol ⁻¹ deg ⁻²]
O2-P-OS	116.09	44.0
O2-P-CT	112.50	39.9
OS-P-OS	102.46	45.2
OS-P-CT	103.83	40.6
P-OS-CT	118.00	78.5
P-CT-CT	114.24	77.0
P-CT-H1	109.64	53.8
OS-CT-CT	108.42	67.8
OS-CT-H1	108.82	50.8
CT-CT-CT	110.63	63.2
CT-CT-H1	110.07	46.4
CT-CT-HC	110.05	46.4
H1-CT-H1	109.55	39.2
HC-CT-HC	108.35	39.4

Table A.4: GAFF equilibrium dihedral angle and dihedral energy parameters. Asterisk indicates modified parameters.

Dihedral	n=1		n=2		n=3	
	V_n [kcal mol ⁻¹]	γ_n [deg]				
O2-P-OS-CT*	2.00	180	3.00	180		
O2-P-CT-CT*			0.80	180		
O2-P-CT-H1*			0.80	180		
OS-P-OS-CT*	2.00	180	3.00	180		
OS-P-CT-CT*			0.80	180		
OS-P-CT-H1*			0.80	180		
CT-P-OS-CT*			2.40	0		
P-OS-CT-CT					1.15	0
P-CT-CT-CT					1.40	0
P-CT-CT-HC					1.40	0
P-OS-CT-H1					1.15	0
OS-CT-CT-CT					1.40	0
OS-CT-CT-HC	0.25	0				
CT-CT-CT-CT	0.20	180	0.25	180	0.18	0
CT-CT-CT-H1					0.16	0
CT-CT-CT-HC					0.16	0
H1-CT-CT-HC					0.15	0
HC-CT-CT-HC					0.15	0

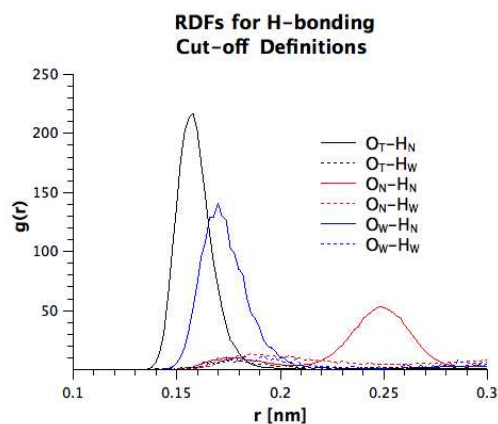


Figure A.1: The RDFs used to determine the distance cut-off given in the text for the hydrogen bond definitions of each hydrogen bond type.

Table A.5: TBP and dodecane AM1-BCC charges. For dodecane, the carbon and hydrogen atoms are denoted by position in the chain.

Atom	AM1-BCC [e]
<hr/>	
TBP	
O2	-0.7963
P	1.5955
OS	-0.5682
CT ₁	0.1644
CT ₂	-0.0834
CT ₃	-0.0814
CT ₄	-0.0921
H1 ₁	0.0467
HC ₂	0.0567
HC ₃	0.0417
HC ₄	0.0347
<hr/>	
dodecane	
CT _{1,12}	-0.0891
CT ₂₋₁₁	-0.0744
HC _{1,12}	0.0317
HC ₂₋₁₁	0.0367

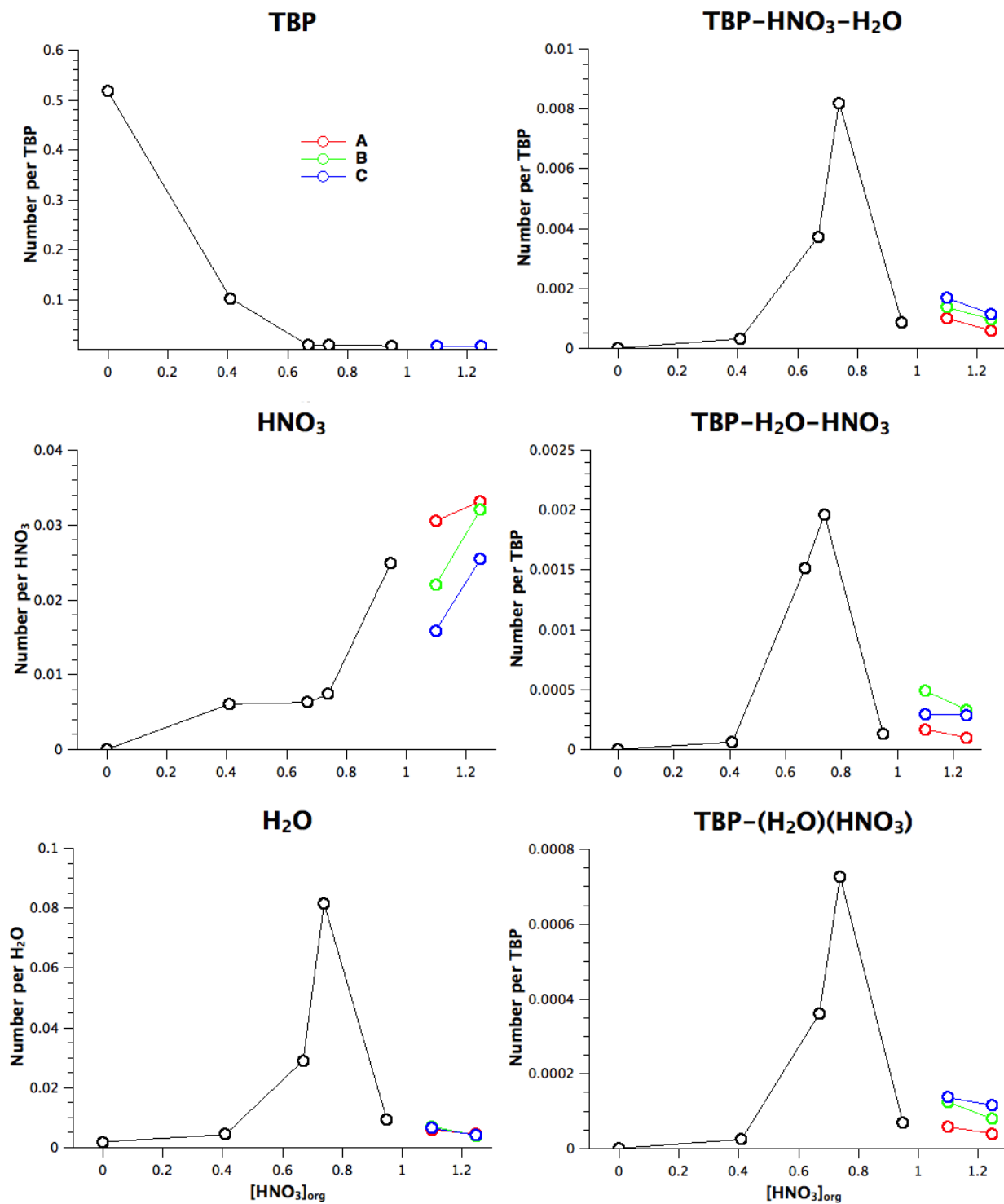


Figure A.2: The average observed number of the TBP, TBP-HNO₃-H₂O, HNO₃, TBP-H₂O-HNO₃, H₂O and TBP(HNO₃)(H₂O) structures.

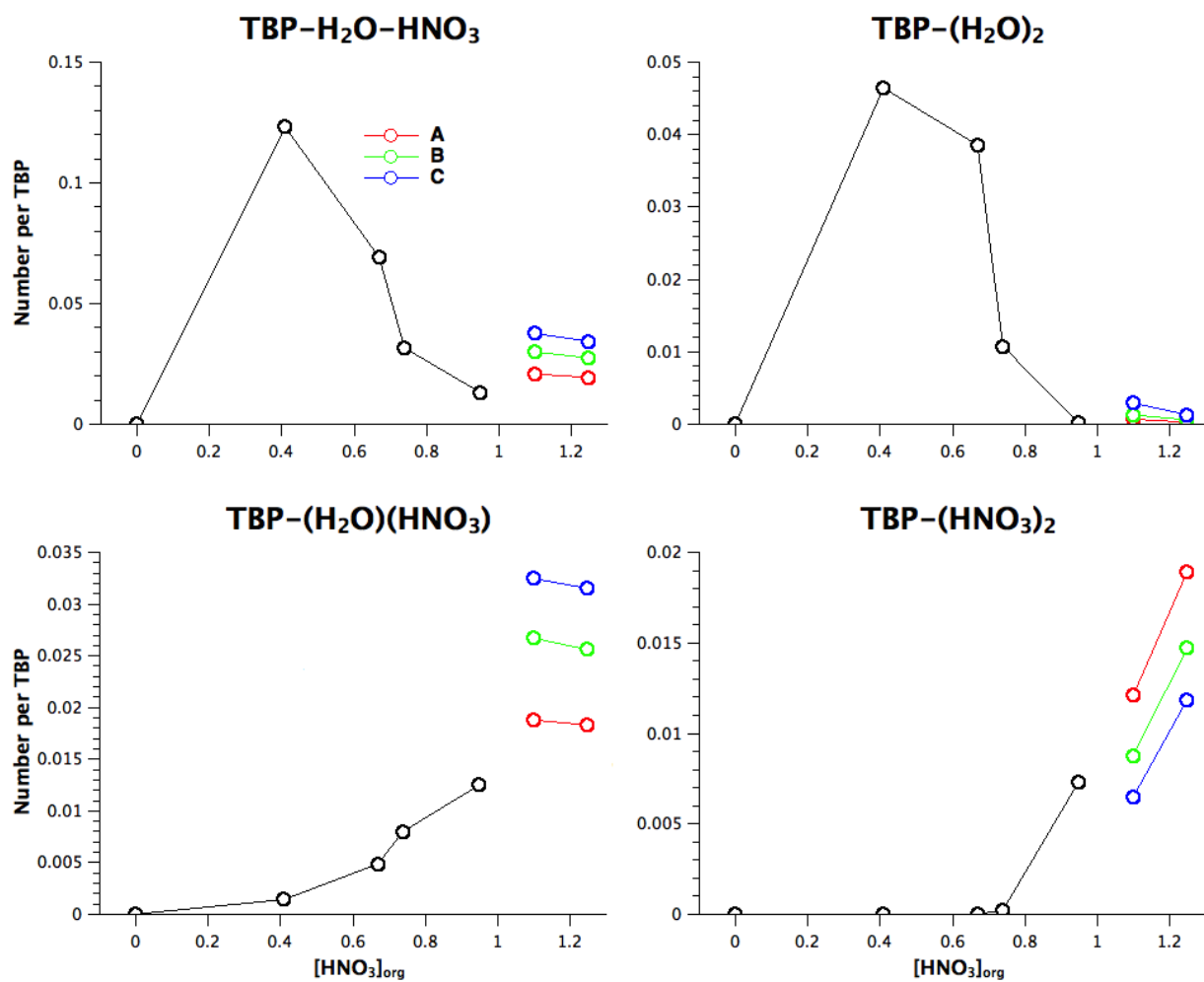


Figure A.3: The average observed number of the TBP-H₂O-HNO₃, TBP(H₂O)₂, TBP(H₂O)(HNO₃) and TBP(HNO₃)₂ substructures.